A Study on Phosphides-based Negative Electrode Materials for Sodium Secondary Batteries Using Ionic Liquid Electrolytes

Shubham Kaushik

Table of contents

Chapter 1

General Introduction

1.1 Electrochemical energy storage system

The rapid development of this technological era has resulted in high demands for energy. Currently, a major portion of energy is mainly generated by combusting non-renewable fossil fuels. The limited amount of non-renewable resources raises concerns over the sustainability and reliability of these resources [1, 2]. Fortunately, renewable resources like solar and wind energies are inexhaustible and holds an immense potential to provide future energy requirements [3]. However, due to their intermittent nature, introduction of energy storage systems (ESS) have become indispensable for practical realization of renewable resources [1, 2]. ESS plays a vital role in frequency regulation, load leveling, and peak shaving by controlling the energy supply according to the requirements [4, 5]. Moreover, it also enables the decentralization of the energy grid and making energy transmission efficient and more reliable [6].

The ESS technology has significantly improved in the past few decades and there are several kinds of ESS available based on scale and application (Figure 1-1) [2]. For example, the traditional pumped hydro power and compressed air energy storage are the most employed technologies for large scale and high energy application, whereas supercapacitor is a popular choice for high power applications. Among all the different ESSs, batteries have emerged as a versatile option covering a wide range of applications from room temperature to high temperature offering simple scalability and high round-trip efficiency [7-9].

A battery stores energy in the form of chemical energy and provides electricity by the electrochemical reactions. Depending on different chemistries, several types of rechargeable batteries have emerged in the market as shown in Figure 1-1. Among them, Li-ion batteries (LIBs) have gained widespread attention owing to its high energy and power densities [10, 11]. After the commercialization by SONY in 1991, the LIBs have found various applications from daily consumer electronic gadgets to electric vehicles [2, 12]. The primary chemistry consisting of graphite, non-aqueous electrolyte, and lithium cobalt oxide ($LiCoO_2$) have been evolved to several other earth abundant and safer components such as lithium iron phosphate $LiFePO_4$ and polymer electrolytes [13, 14], although the former components are still in use in some applications. One of the biggest drawbacks of LIBs is the limited abundance and uneven distribution of lithium reserves [15, 16], which makes the cost of Li resources unstable in near future [17] (Table 1-1). The projected increase in the demand of LIBs in future will definitely put pressure on the resources [18]. Therefore, there is an urgent need to find alternative battery technologies to share the burden of LIBs.

1.2 Sodium secondary batteries

Sodium is significantly more abundant and evenly distributed than lithium in earth crust and seawater (Table 1-1) [19]. Moreover, the low standard electrode potential of Na^+/Na (−2.71 vs. standard hydrogen electrode) and similarity in the properties to lithium, being present in the same group, makes its battery application suitable based on the technologies developed for LIBs. Some sodium-based battery technologies such as Na/S and $Na/NiCl_2$ batteries are already commercialized. These batteries operate at high temperature (250~300 °C) using beta-alumina (sodium aluminate) solid state electrolytes (for ensuring high conductivity of electrolyte and maintenance of good contact between electrode and electrolyte [20-22]. However, operating at high temperatures poses safety threats and decreases overall efficiency of the process, which limits their acceptance in society [23].

The development of sodium-ion batteries (NIBs) and LIBs were proceeding in parallel in 1970s and 1980s. A reversible capacity of sodium was confirmed in $NaCoO_2$ positive electrode [24] but better electrochemical performance obtained in LIBs gained attention at that time leaving NIBs development stagnant. However, in early 2000, the research interest in NIBs was resurfaced when a reversible insertion of sodium in hard carbon (~300 mA h g^{-1}) was demonstrated at a very low voltage [25]. The cost benefit owing to the utilization of cheaper Al current collector [26] (Na does not form alloy with Al) and abundant sodium resources are additional advantages (see Table 1-1). The lower solvation energy of Na^+ than Li^+ owing to its weaker Lewis acidity can also facilitate the electrode/electrolyte interface reactions [27]. Therefore, NIBs hold a huge potential for development of ESS technology.

1.3 Negative electrodes

The mission to find a potential negative electrode material for NIBs for high electrochemical performance and safety is still ongoing. Extensive efforts have been stressed on improvement of negative electrode materials in the past decades. Negative electrode materials are broadly categorized into carbonaceous, Ti-based materials, alloy and conversion materials. The following sections provide a brief description of material characteristics of each category in the beginning followed by detailed electrochemical behavior.

1.3.1 Carbonaceous materials

Carbon materials have always been the focus of electrode materials in electrochemistry field owing to their low-cost, good electrical conductivity, and chemical robustness. Despite delivering a decent reversible capacity (~372 mA h g^{-1} for LiC_6) as negative electrode in LIBs, [28] graphitic carbon generally shows very limited capacity (~35 mA h g^{-1} for the first charge with the formula NaC_{64}) [29] in NIBs using conventional ester-based electrolytes owing to the thermodynamic instability of sodium-inserted graphite intercalation compounds (GICs) [30, 31]. The limitation has been circumvented by using co-intercalation phenomena reported, through the formation of (Na(diglyme)C_{20}) GICs, a reversible capacity approaching 100 mA h g^{-1} with a stable cycleability over 1000 cycles was recently achieved for graphite electrode [32]. Another type of carbon is getting popular, generally named as "hard carbons (HC)" due to their non-graphitizable nature, consisting of turbostatic graphene domains with local stacking resulting in porosity of various sizes and shapes [33, 34]. The HCs are able to be prepared by the pyrolysis of renewable bio-materials. The functional groups and porosity can be tuned by the pyrolysis conditions [35]. HC have become an attractive choice of negative electrode material owing to the low operating voltage and improved Na insertion storage (~300 mA h g^{-1}) than graphite [25].

One of the earliest studies for HC in NIBs was reported in 2000, where a HC prepared by pyrolysis of glucose at 1000 °C provided a reversible capacity of 300 mA h g^{-1} using 1 mol dm^{-3} $NaClO_4$ in EC:DEC (3:7 v/v) [25]. It was proposed that Na insertion into HC can be visually represented as the "house of cards" model which states that the random arrangement of graphene layers produces regions of local stacking (two or three layers) and nanoscale porosity which gives rise to the sloping charging and discharging profile at higher voltage and plateau region at potential close to 0 V, respectively. However, the clear understanding of the phenomenon is still under debate. In another study, ^{23}Na magic-angle spinning nuclear magnetic resonance (MAS NMR) spectroscopy of HC synthesized by pyrolysis of sucrose at various temperatures demonstrated Na cluster formation in the micropores of HC [36]. Moreover, it was suggested that the electrochemical capacity is highly influenced by pyrolysis temperature as well as defect sites in the structure. The precursor of HC (peat moss [37], banana peels [38], pomelo peels [39]) and doping with heteroatom (S [40], P [41], PO_x [42]) also influences the electrochemical performance significantly by inducing defects as summarized in the review article [34]. Overall, the main structural features that affect the performance of HC in NIB are: (1) interlayer *d*-spacing and number of graphene layers, (2) porosity, and (3) amount of defects induced by either doping of heteroatom or heat treatment of precursor. The effects of electrolytes will be discussed in details in Section 1.4.2. Although the aforementioned results show that HC provides a high electrochemical performance, the extremely low sodiation potential close to 0 V vs. Na^+/Na can be hazardous due to the risk of Na metal plating at high current rates.

1.3.2 Titanium based materials

Titanium is the ninth most abundant element on earth and have been investigated in electrode materials for a long time. The earliest investigation of TiS_2 dates back to 1976, when Li intercalation compound Li_xTiS_2 was introduced [43]. However, due to the invention of high voltage $LiCoO_2$ [44], the investigation for Ti-based materials was halted. These materials were resurfaced in 1989 with the report of lithium titanate ($LiTi_2O_4$ and $Li_{4/3}Ti_{5/3}O_4$) which provided high cycleability and fast Li kinetics [45]. Currently, $Li_4Ti_5O_{12}$ is widely used as a negative electrode material in some commercialized LIBs for fast charging purposes due to its zero strain effect [46]. Another largely investigated material is titanium dioxide (TiO_2) which is available in several polymorphs including anatase, rutile, brookite, and bronze. TiO_2 can be prepared easily and is stable in ambient conditions. In LIBs, the reaction of TiO_2 generally proceeds through the redox activity of Ti^{3+}/Ti^{4+} in TiO_6 octahedra by Li-ion intercalation and deintercalation [47]. After successful application of Ti-based materials in LIBs, investigations have been done in NIBs also [48, 49].

The electrochemical performance of Ti-based materials has been improved in recent years but there are some existing limitations. The electronic conductivity of the Ti-based compounds is often low resulting in limited kinetics which is often circumvented by nano-structuring [50, 51], carbon coating [52, 53], and, morphology optimization [54, 55] of the particle. A comparative study of different phases of TiO_2/C (anatase, rutile and amorphous) prepared by template approach showed a better cycleability and rate capability in case of the anatase phase than other ones owing to the low energy barrier for Na^+ insertion and two-dimension diffusion pathways [56]. Interestingly, the charge-discharge mechanism of anatase TiO_2 in NIBs is different from that in LIBs, showing metallic Ti, Na_2O and amorphous sodium titanate after charging according to X-ray diffraction, X-ray photoelectron spectroscopic, and Raman spectroscopic analyses [57]. The bronze phase of TiO_2 prepared by hydrothermal synthesis exhibited a good rate capability (150, 100, and 70 mA h g^{-1} at 0.1, 1, and 10 C). Moreover, amorphization of the product was observed after charging and the similar charge-discharge mechanism to anatase case was reported [58].

Another class of highly investigated Ti-based material is sodium titanate. The charge-discharge behavior of $Na_2Ti_3O_7$ prepared by heat treatment was reported in which a high reversible capacity of 178 mA h g^{-1} as well as a low Ti^{4+}/Ti^{3+} redox potential of 0.3 V vs. Na/Na^+ was observed [59]. Additionally, $Na_2Ti_6O_{13}$ [60] and $Na_4Ti_5O_{12}$ [61] were also investigated but only a limited capacity below 50 mA h g^{-1} was observed in both the cases. On the other hand, the Li counterpart of $Na_4Ti_5O_{12}$, $Li_4Ti_5O_{12}$, provided a Na storage capacity of 155 mA h g^{-1} at 0.91 V vs Na/Na^+ based on a three-phase mechanism ($2Li_4Ti_5O_{12} + 6Na^+ + 6e^- \rightleftharpoons Li_7Ti_5O_{12} + Na_6LiTi_5O_{12}$) [62]. Recently, polyanion compounds consisting of titanium phosphates ($Na_3Ti(PO_4)_3$) [63] and sulfates ($Ti_2(SO_4)_3$) [64] have demonstrated promising performance for NIBs owing to the open-framework structures enabling facile pathways for Na^+ ion diffusion. Porous $NaTi_2(PO_4)_3/C$ nanocubes exhibited a high rate capability and cycleability by providing 98 mA h g^{-1} after 2000 cycles at current density of 4000 mA g^{-1} [65].

1.3.3 Alloying and conversion materials

High capacity electrode materials are desirable for achieving high energy density in NIBs. Alloying materials form Na-rich compounds providing high reversible capacities. Most of them consist of elements in groups 14 and 15 in the periodic table. Table 1-2 summarized the final sodiated product, electrical conductivity, theoretical capacity, and volume change of the common alloying materials for NIBs. The large capacities often accompany a large volume change which creates a large mechanical strain in the electrode by agglomeration or pulverization of particles leading to poor cycleability in these materials [66, 67]. Moreover, degradation of the electrode causes continuous solid electrolyte interface (SEI) formation which decreases the Coulombic efficiency [68]. Nano-structuring, morphology optimization, carbon compositing, and selection of suitable electrolyte are required to improve the performance [48, 69, 70].

Engineering metal with non-metallic alloys such as M-P/Sn/Sb is also an attractive strategy to alleviate the aforementioned problem. The charge-discharge mechanism in these cases leads to the conversion based mechanism [71]. The metal M can serve different roles based on its activity or non-activity towards sodiation. When active, M contributes to the capacity, facilitate Na^+ ion diffusion, and acts a mutual matrix buffering the volume change. In the case of inactivity, M functions to buffer the volume change and improve the electrical conductivity of the electrode. In the recent years, several review articles have been reported to highlight the electrochemical performance of alloying and conversion based materials and their underlying challenges in NIBs [72, 73].

In 2011, the sodiation of Sn was theoretically investigated and formation of four different phases ($NaSn_5$, NaSn, Na_9Sn_4, $Na_{15}Sn_4$) was reported [74]. However, only the Na-rich phase ($Na_{15}Sn_4$) was experimentally found by X-ray diffraction (XRD) [75]. Later, an *in-situ* transmission electron microscopy (TEM) revealed a two-step sodiation process of crystalline Sn: a two phase conversion of Sn to amorphous $NaSn_2$ followed by a single-phase transformation to amorphous Na_9Sn_4 and Na_3Sn and finally to crystalline $Na_{15}Sn_4$ [76]. In 2013, Yamamoto et. al. systematically studied the formation of different Na-Sn alloy using Na[FSA]-K[FSA] (FSA: bis(fluorosulfonyl)amide anion) ionic liquid as electrolyte [77]. They observed that the plateaus at 0.16 and 0.08 V correspond to a two-phase transition of α-NaSn/Na_9Sn_4 and Na_9Sn_4/$Na_{15}Sn_4$, respectively, by *ex-situ* XRD. Moreover, the equilibrium potentials of β-Sn/$NaSn_2$ and $NaSn_2$/α-NaSn were proposed to be 0.53 and 0.46 V, respectively.

Several reports on other alloying materials (Sb [78], Ge [79], Pb [80], Bi [81]) also emerged in subsequent years. A hollow Sb nanospheres, prepared by galvanic replacement of Ni nanosheets, demonstrated a high reversible capacity of 622 mA h g^{-1} at a rate of 50 mA g^{-1} after 50 cycles [82]. Germanium thin films synthesized by sputtering exhibited a low average potential of 0.4 V vs. Na^+/Na and a reversible capacity of 350 mA h g^{-1} at a rate of 18.45 mA g^{-1} [79]. A highly loaded Pb with 98 wt% in the electrode showed a high reversible capacity of 464 mA h g^{-1} at 26 mA g^{-1} in 1 mol dm^{-3} $NaPF_6$/diglyme electrolyte givinga stepwise charge-dischargewith four plateaus similar to that observed for Sn electrode, which was confirmed by *in-situ* XRD [80]. In 2012, SnSb/C nanocomposite prepared by high energy ball-milling provided a high capacity of 544 mA h g^{-1} at 100 mA g^{-1} with good capacity retention [83].

1.3.4 Phosphorus and phosphide based materials

Phosphorus is one of the most abundant elements in the earth crust and it shows one of the highest theoretical gravimetric capacities among all the alloying based materials (2596 mA h g^{-1}) [84]. It mainly exists in three allotropes: white, red and black P. The schematic of the structures is shown in Figure 1-2. White P is not suitable for battery application because it is highly toxic and reactive in air [85]. Red P is highly investigated as a negative electrode material for NIBs owing to its relative stability in air and abundance [86]. Black P with a layered structure is the most stable allotrope of P usually prepared at severe conditions, possessing a high electrical conductivity (3.0 S cm^{-1}) [87]. The charge-discharge mechanism is the same for all the allotropes of P: $P + 3Na^+ + 3e^- \rightarrow Na_3P$. In this section, the electrochemical performance of P and P-based materials will be summarized in details. In addition, common issues and strategies for improvement of performance will also be discussed.

1.3.4.1 Black P and related materials

As mentioned above, black P possesses a layered structure consisting of phosphorene layers bound together by van der Waal forces (Figure 1-2 (b)). The insertion of Na^+ ion (2.04 Å) is possible owing to a larger interlayer distance of 3.08 Å [88]. In 2015, the first experimental study on the electrochemical performance of black P was reported for NIBs [87]. A high capacity of 1587 mA h g^{-1} was observed at the current density of 125 mA g^{-1} in the first cycle and the cycleability was significantly improved by using FEC (5 wt%) as an additive with 1 M $NaPF_6$ in EC/DEC (1:1 v/v). Carbon composite of black P with Ketjen black and multiwalled carbon nanotubes showed high Coulombic efficiency in the first cycle (91.1%) and 1700 mA h g^{-1} reversible capacity after 100 cycles [89]. Buffering of the large volume changes and maintenance of electrical contact owing to the efficient distribution of P in the nanostructureed carbon matrix was suggested as the primary reason behind good electrochemical performance. In another report, a black P/graphene composite prepared by pressurization method at room temperature exhibited a high rate capability (720 mA h g^{-1} at 40000 mA g^{-1}) and a 92.5% capacity retention after 100 cycles [90].

Similar to graphene, phosphorene also holds promise as a high performance negative electrode for NIBs owing to the single layer 2-D structure. Several researches have reportdifferent techniques for synthesizing few-layers phosphorene (FL-P) such as mechanical exfoliation, liquid-phase peeling and many more [91, 92]. Among them, electrochemical cathodic exfoliation via intercalation of tetraalkylammonium cations has been reported as an effective method to prepare tunable FL-P [93]. In this report, a five-layer phosphorene (FL-P-5) displayed a discharge capacity of 321 mA h g^{-1} at 2500 mA g^{-1} and retained 603 mA h g^{-1} after 100 cycles. Despite delivering decent electrochemical performance in NIBs, the energy intensive preparation methods and high irreversible capacities limit applicability of black P and related materials for practical application.

1.3.4.2 Red P and related materials

The structure of red P consists of P_4 tetrahedra connected by the P-P bond of each other forming a polymeric chain (Figure 1-2 (c)). Every P atom is bonded to other three P atoms in a tetrahedral structure. Owing to this structure, the red P is stable in air and environmentally benign. However, its electrical conductivity is very low and the alloying reaction with Na results in high volume change as shown in Table 1-2, which results in pulverization of the active material and continuous decomposition of the electrode during cycling. Several strategies have been employed to conquer this problem: constructing carbon composites, downsizing the particle size, and making alloys with metals.

Carbon composites of red P have been actively investigated. Various carbon sources have been employed for carbon composites including acetylene black (AB) [94], multi-walled carbon nanotubes [95], single-walled carbon nanotubes [86], mesoporous carbon [96], and graphene [97]. The first study on Na storage in red P was reported on a P/AB composite prepared by a simple high energy ball-milling method. A high reversible capacity of 1764 mA h g^{-1} was observed with a Coulombic efficiency of 87% in the first cycle but a gradual capacity deterioration was observed [94]. In another report, the cycleability was considerably improved by incorporating single-walled carbon nanotubes with red P, which demonstrated only 0.01% capacity fading over 2000 cycles [86]. Graphene is a revolutionary material which strongly influences the kinetics and activation owing to the superior electrical conductivity and high surface area. Red P nanodots deposited on reduced graphene oxide (P-rGO) prepared by physical vapor deposition illustrated a high capacity of 1594 mA h g^{-1} in the first cycle [98]. Moreover, it provided a discharge capacity of 510 mA h g^{-1} at 31878 mA g^{-1} and 86.6% capacity retention after 100 cycles because of the facilitated electron pathway and volume change accommodation by the layered rGO.

Reducing the particle size in nanometer range is also an effective way to improve the overall electrochemical performance. For instance, P nanoparticles (100-150 nm) attached to the graphene sheets displayed a high discharge capacity of 2355 mA h g^{-1} in the initial cycle and a high capacity retention of 92.3% after 150 cycles [99]. In another report, a self-standing film of red P nanoparticles (~98 nm) embedded in porous N-doped carbon nanofibers prepared by electrospinning method demonstrated a high rate capability (343 mA h g^{-1} at 10000 mA g^{-1}) and good cycleability (81% capacity retention after 1000 cycles) [100]. Both of the aforementioned studies stressed on the advantage of P nanoparticles for inhibiting electrode mechanical failure and facile diffusion of Na^+ ion due to shorter diffusion length.

1.3.4.3 Metal phosphides

Metal phosphides have been emerging as effective negative electrodes because of several reasons: (1) buffering of the large volume change by the formation of in-situ metal nanoparticles, (2) faster kinetics by the improved electrical conductivity, and (3) high tap densities resulting in high volumetric capacities. According to the reported literature of metal phosphides in NIBs, they can be broadly classified based on reaction mechanism in three categories: conversion, hybrid (conversion + alloying) and others. In addition, these categories can be subcategorized depending on whether the metal is electrochemically active or inactive as a part of electrode material. The conversion process is usually formulated in the following way:

$$M_xP_y + 3yNa \rightleftharpoons xM + yNa_3P \text{ (M inactive)} \quad (1)$$

$$M_xP_y + (3y + z)Na \rightleftharpoons Na_zM_x + yNa_3P \text{ (M active)} \quad (2)$$

In a conversion process, the reaction can be reversible because the original composition of the active material is preserved after desodiation but in some cases amorphization has been observed. The 3d transition metals (Fe, Co, Cu, Ni) are usually inactive towards sodiation except Zn. Nanowires of Cu_3P grown directly on Cu foil provided a reversible capacity of 349 mA h g^{-1} at 50 mA g^{-1} and 96.4% capacity retention after 100 cycles [101]. A reversible reaction of $Cu_3P + 3Na \rightleftharpoons 3Cu + Na_3P$ was observed by *ex-situ* XRD. Based on a similar mechanism, NiP_3 prepared by a ball-milling process delivered a high capacity of 900 mA h g^{-1} at 159 mA g^{-1} [102]. The electrochemical performance of several other metal phosphides (SiP$_2$/C [103], CuP$_2$/C [104], and MoP/rGO [105]) have been reported as negative electrodes for NIBs based on Reaction (1) above. Higher capacities can be achieved by employing Na active metals. For instance, amorphous Se_4P_4 prepared by a simple ball-milling method displayed a high capacity of 1048 mA h g^{-1} (24 Na per molecule of Se_4P_4) at 50 mA g^{-1} with a capacity retention of 840 mA h g^{-1} after 60 cycles [106]. The XRD and MAS-NMR analyses revealed the reversible formation of Se_4P_4, Na_2Se and Na_3P. In another report, ZnP$_2$/C prepared by a solid-state heat treatment and a ball-milling method showed reversible conversion of ZnP_2 to $NaZn_{13}$ and Na_3P confirmed by XRD and X-ray absorption spectroscopy (XAS) [107].

In the hybrid mechanism, the sodiation in the first cycle proceeds through conversion, but the original composition is not recovered after sodiation alloying takes place from the second cycle onwards. It can be represented from the two reaction schemes, depending on the activity of the metal as described below:

Metal inactive:

$$M_xP_y + 3yNa \rightarrow xM + yNa_3P \text{ (first cycle)} \quad (3)$$

$$M + 3yNa + yP \rightleftharpoons M + yNa_3P \text{ (subsequent cycles)} \quad (4)$$

Metal active:

$$M_xP_y + (3y + z)Na \rightarrow Na_zM_x + yNa_3P \text{ (first cycle)} \quad (5)$$

$$zNa + xM \rightleftharpoons Na_zM_x \text{ (subsequent cycles)} \quad (6)$$

$$3Na + P \rightleftharpoons Na_3P \text{ (subsequent cycles)} \quad (7)$$

In the case of the inactive metal, the in-situ formation of metal nanoparticles results in a conductive matrix which improves electrical conductivity as well as prevents P from agglomeration. When metal is active to sodiation, a high capacity can be realized in addition to the aforementioned advantages of volume buffer and inhibition to agglomeration. Cobalt phosphide (CoP) [108] and iron phosphide (FeP) [109] have been observed to provide the hybrid mechanism. In the case of CoP, the XPS peak corresponding to the Co metal in Co $2p_{3/2}$ spectrum remained unchanged after charging and discharging. Tin alloys with phosphorus to give many phosphides in stoichiometry [110] (Sn_4P_3, SnP, Sn_3P_4, SnP_3) and has been explored immensely as a negative electrode for NIBs [111-113]. The most common composition Sn_4P_3 exhibited a remarkable electrochemical activity by showing a reversible gravimetric capacity of 718 mA h g^{-1} with negligible capacity fading during 100 cycles [112]. Moreover, it showed a low reaction voltage (0.3 V vs Na^+/Na) and a high volumetric capacity owing to the high density. The charge-discharge mechanism is similar to formula (5), (6), and (7), forming $Na_{15}Sn_4$ and Na_3P in the first charging step followed by separate alloying/dealloying in the subsequent cycles confirmed by XAS, XRD and TEM. The germanium phosphide/carbon composite (GeP_5/C) prepared by high energy ball-milling also exhibits hybrid mechanism by forming NaGe and Na_3P and provided a large capacity of 1250 mA h g^{-1} with a Coulombic efficiency of 93% in the first cycle owing to the layered structure and high electrical conductivity [114].

Some metal phosphides show different mechanisms from the aforementioned conversion or hybrid ones. For instance, the insertion behavior has been recently reported in vanadium phosphide (V_4P_7) showing a much lower capacity of ~240 mA h g^{-1} at 50 mA g^{-1} than observed in the above-mentioned metal phosphides. Moreover, FeP_2 [115] and TiP_2 [116] showed inactivity towards sodiation. A possibility of sodiation potential of FeP_2 lower than 0 V was suggested as the reason of inactivity because of the reported low potential of lithiation of FeP_2 (0.3 vs Li^+/Li) [117] and inherent difference of ~0.3 V between standard electrode potential of lithium and sodium redox. However, the understanding of the charge-discharge behavior of insertion-based metal phosphides and inactivity is not clear so far and requires systematic investigation. From the discussion above, metal phosphides illustrating interesting electrochemical properties can be a promising class of negative electrode material for NIBs.

1.4 Ionic liquid electrolytes

Electrolytes play an essential role to determine the safety, cost and electrochemical performance of batteries. Electrolytes in current LIBs usually consist of Li salts, most commonly $Li[PF_6]$ and $Li[ClO_4]$, and organic solvents, such as ethylene carbonate (EC), diethylene carbonate (DEC), propylene carbonate (PC), and dimethyl carbonate (DMC). In NIBs, Na counterparts of the Li salts ($Na[PF_6]$ and $Na[ClO_4]$) are often used with the above-mentioned solvents. Although Na-based organic electrolytes possess high ionic conductivities at room temperature, the reported electrochemical performance is not satisfactory. Flammability and volatility associated with utilizing organic electrolytes are important factors to construct safe batteries.

Ionic liquids (ILs), entirely consisting of ions, have been attracting attention as electrolytes for ESS owing to their low flammability, negligible volatility, high thermal stability, and wide electrochemical window. Such beneficial properties make the utilization of IL electrolytes feasible in a wide temperature range from space applications at low temperatures to industries at high temperature. In some reports, IL electrolytes showed a significant improvement in electrochemical performance of NIBs compared to organic electrolytes in terms better cycleability and superior rate capabilities (see Table 1-3). It is generally reported that ILs induce the formation of uniform and stable SEI layer and facilitate Na^+ ion diffusion in the electrolyte at elevated temperatures. The Na[FSA]-[C_3C_1pyrr][FSA] ($C_3C_1pyrr^+$: *N*-methyl-*N*-propylpyrrolidinium cation) IL has been widely investigated for NIBs at both room temperature and intermediate temperature. This IL exhibits a wide electrochemical window and an ionic conductivity of 18.4 mS cm^{-1} at 358 K (20 mol% Na[FSA]) [118, 119] (see Table 1-4). The structures of C_3C_1pyrr cation and FSA anion are shown in Figures 1-3 and 1-4, respectively.

1.4.1 Solid electrolyte interphase

Extensive efforts have been focused on the improvement of negative electrode materials in recent decades, but the investigation of electrode/electrolyte interfacial properties is equally important for ensuring the overall performance and safety of batteries. The SEIs formed by reductive decomposition of conventional ester-based electrolytes are considered not sufficiently stable, leading to severe capacity degradation. The success of conventional HC negative electrodes depends on complicated electrolyte formulations and the introduction of SEI forming additives. Thus, for the development of negative electrodes, exploring compatible electrolytes is indispensable.

The performance and safety of the batteries are highly dependent on the SEI layer properties [120] which are sensitive to the parameters such as salt concentration of electrolyte

[121], temperature [122, 123], and binder [124]. Investigation of physical and chemical properties of SEI layer is very important for understanding the degradation mechanism in batteries. However, such a study is often hindered because of the complex structure and nanoscale dimensions of SEI layer as well as limited characterization tools. Moreover, owing to the higher reactivity and higher standard redox potential of Na than Li, the technology transfer of interfacial properties from LIBs is not always possible. In addition, the solubility of SEI in conventional electrolyte in Na secondary batteries aggravates the self-discharging properties. R. Mogensen et al. confirmed the self-discharging properties using conventional 1 mol dm^{-3} Na[PF$_6$]-EC/DEC in Na secondary batteries, whereas minimal self-discharge was found in LIBs [125]. Therefore, it is imperative to investigate the interfacial properties in Na secondary batteries in other types of electrolytes.

Na metal is generally used as the counter electrode in half-cell configurations. However, the electrochemical behavior at the Na electrode itself is generally not well investigated in each case, causing the origin of cell degradation indistinguishable from the working electrode of interest [42]. The SEI layer on Na metal using ester based EC/DEC and ether based diglyme and tetraglyme with 1 mol dm^{-3} Na[PF$_6$] was investigated by X-ray photoelectron spectroscopy (XPS) and formation of a thin and stable SEI was observed in the diglyme case [126] whereas a thick and highly resistive film was formed in EC/DEC. In-depth XPS studies identified a formation of uniform and impermeable to solvent layer consisting of inorganic components in glyme based electrolytes including Na_2O and NaF contrasting with a mix organic (RCH_2OCO_2Na) and inorganic composition in EC/DEC. It was found that a mixed organic-inorganic SEI is prone to solvent permeation resulting into dendrite growth. Recently, the electrochemical properties of Na metal were also studied in IL electrolytes. Typically, a large interfacial resistance resulting, presumably resulting from the surface film of Na metal, is observed in the IL electrolytes [127-129]. Such impedance could sometimes even hinder the evaluation of true performance of the target electrodes in half-cell configuration. A systematic study on the Na/Na symmetric cells using ILs showed that the overall cell resistance dramatically decreases with increasing temperature but increases with Na salt content [129].

The electrolyte effects on the composition of SEI layer formed on hard carbon (HC) was extensively investigated by G. G. Eshetu et al. [130] The anion of the electrolyte salt was reported to govern the characteristics of the SEI formed on HC. Especially, the organic content decreases in the order Na[PF_6] > Na[ClO_4] > Na[TFSA] > Na[FTFSA] > Na[FSA] (TFSA = bis(trifluoromethylsulfonyl)amide, FTFSA = fluorotrifluoromethylsulfonylamide). The electrolyte effect on the thermal stability of SEI and anodic stability of Al current collector were studied by the same group. For a fixed solvent (EC/DMC), the onset temperature of first exothermic peak (related to SEI cracking) follows the sequence: Na[ClO_4] < Na[PF_6] < Na[TFSA] ≈ Na[FTFSA] < Na[FSA].[131] The Al dissolution or the anion decomposition increases in the order: Na[PF_6] < Na[ClO_4] < Na[TFSA] < Na[FTFSA] < Na[FSA] in EC/DEC. However, Na[FSA] showed the stability towards the decomposition in the different solvents in the order: EC/DEC < EC/DEC + 5% Na[PF_6] < [C_4C_1pyrr][FSA] (C_4C_1pyrr$^+$: *N*-butyl-*N*-methylpyrrolidinium cation).

IL-derived SEI could be distinctly different from that formed in organic electrolytes. Performance and interfacial properties of HC in 1 mol dm^{-3} Na[FSA]-[C_3C_1pyrr][FSA] IL and conventional organic electrolyte 1 mol dm^{-3} Na[ClO_4]-EC/DEC (1:1 v/v) were compared at 25 °C. EIS of HC/HC symmetric cell showed a lower charge transfer resistance in IL than organic electrolyte. A dense SEI enriched with Na_2CO_3 and $NaCO_2R$ species was confirmed in the organic electrolyte by scanning electron microscopy (SEM) and X-ray photoelectron spectroscopy (XPS) measurements. These species are considered to be the resistive components in SEI layer [127]. Similar species were also observed with 1 mol dm^{-3} Na[ClO_4]-EC/DEC (1:1 v/v) in 3-D carbon framework (CF) (discussed below), whereas polyolefin ($(CH_2)_n$) and S=C=O derived from FSA anion was found in IL [132]. With respect to alloying based electrode, a robust SEI layer is widely acknowledged as a crucial factor to realize good cycleability since these materials undergo an enormous volume change during sodiation/desodiation. The evolution of SEI composition on red phosphorus cycled in organic electrolytes and IL was investigated by the combination of hard X-ray photoelectron spectroscopy (HAXPES) and time-of-flight secondary ion mass spectroscopy (TOF-SIMS) [133]. The TOF-SIMS analysis showed that the SEI layer generated in IL electrolyte was composed of a uniform mixture of organic and inorganic components (with the inner surface primarily covered with inorganic species), whereas mainly inorganic species were observed in organic electrolyte under the same condition. Moreover, it can be clearly seen that the SEI composition dynamically changed with cycles in organic electrolyte, while the composition remains stable in IL one. The homogeneous and complete coverage of SEI layer on red phosphorus was considered as the reason behind the improved reversible capacity and capacity retention in the IL electrolyte.

1.4.2 Performance of negative electrodes in IL

The electrochemical performance of negative electrodes investigated using ILs are summarized in Table 1-3. The details of the corresponding reports are given in the following. The electrochemical performance of 3-D carbon framework (CF) prepared by high speed homogenizer of graphene nanosheets and carbon nanospheres was analyzed using 1 mol dm^{-3} Na[ClO$_4$] in EC/DEC (1:1 v/v) and 1 mol dm^{-3} Na[FSA]-[C$_3$C$_1$pyrr][FSA] IL at 25 and 60 °C [132]. A capacity retention of 85% was observed after 250 cycles with IL electrolyte at 25 °C while only 70% capacity retention was observed with organic electrolyte at room temperature. At 60 °C, the performance was significantly improved in IL than in organic electrolyte. Moreover, the self-discharge in organic electrolyte (15%) exceeded than in IL (8%) after five days of rest. Robust SEI layer formation owing to the decomposition of FSA$^-$ was claimed as the main reason behind the better cycleability. Electrochemical performance of commercial HC powders was investigated with 20 mol% Na[FSA]-[C_3C_1pyrr][FSA] IL in a wide temperature range of −10 to 90 °C [134]. This HC showed high capacity of 277 mA h g^{-1} at 20 mA g^{-1} and remarkable rate capability at 90 °C owing to the high ionic conductivity and low charge transfer resistance of IL. It also showed a capacity of 193 mA h g^{-1} at 20 mA g^{-1} at 25 °C which is important for room temperature applications.

Charge-discharge behavior of commercial anatase TiO_2 was reported with 10 mol% Na[TFSA]-[C_3C_1pyrr][FSA] [135]. Even at 25 °C, TiO_2 showed decent rate capability by providing 47 mA h g^{-1} at 2 C (1C = 335 mA g^{-1}). To increase the reversible capacity, Fe_2O_3 was incorporated with TiO_2 by heat treatment of commercial TiO_2 and $Fe(NO_3)_3$. A high reversible capacity of 386 mA h g^{-1} at 10 mA g^{-1} and 80% capacity retention after 300 cycles at 200 mA g^{-1} was achieved at 90 °C using 20 mol% Na[FSA]-[C_3C_1pyrr][FSA] [136]. A niobium doped rutile TiO_2 ($Ti_{0.94}Nb_{0.06}O_2$) prepared by a sol-gel method was investigated as negative electrode for NIBs using 1 mol dm^{-3} Na[FSA]-[C_3C_1pyrr][FSA] and 1 mol dm^{-3} Na[FSA] in PC [137]. A high capacity retention of 97% was observed with Na[FSA]-[C_3C_1pyrr][FSA] at 60 °C.

Several intermetallic compounds of Sn-M (M = Fe, Ni, Cu) with 56 mol% Na[FSA]-K[FSA] IL were investigated at 90 °C for NIBs [138-140]. The charge-discharge curves of Sn-Cu film annealed for 4h show four plateaus even after 1000 cycles at 90 °C, which represents the excellent cycleability of this system. This result was attributed to the buffering effect of inactive component Cu_3Sn and randomly dispersed less electrochemical active component, Cu_6Sn_5. Sn_4P_3 exhibited remarkable cycleability (112% for 200 cycles) and high reversible capacity with 1 mol dm^{-3} Na[FSA]-[C_3C_1pyrr][FSA] at 30 °C [141]. The richer phosphorus phase of SnP_3 was also investigated using 1 mol dm^{-3} Na[FSA]-[C_3C_1pyrr][FSA] at 30 °C but severe capacity degradation was observed owing to the insufficient buffering power of low Sn content in SnP_3 [141]. Tin oxide SnO_2/graphene composite prepared by supercritical-CO_2-assisted synthesis method was analyzed in IL electrolytes [142]. At elevated temperature of 60 °C, high reversible capacities of 600 and 330 mA h g^{-1} were obtained at 20 and 1000 mA g^{-1}, respectively, with 1 mol dm^{-3} Na[FSA]-[C_3C_1pyrr][FSA].

1.5 Aims of this study

Based on the background described above, development of negative electrode materials with high capacity and energy density is an urgent topic for practical NIBs, and the use of IL electrolytes contributes it to bring out their performance and attain safe energy storage devices. The aim of this study is to investigate phosphide-based negative electrode materials prepared by high energy ball-milling using the Na[FSA]-[C_3C_1pyrr][FSA] IL at room and intermediate temperatures. A brief summary of aim regarding each chapter is given below:

Chapter 2 provides information about the details of experimental setup, procedures and conditions followed in the Chapter 3 to Chapter 7.

In Chapter 3, the charge-discharge behavior of copper phosphide-carbon composite (CuP_2/C 80:20 in weight ratio) is investigated at 25 and 90 °C. The reaction mechanism is revealed by *ex-situ* and *in-situ* XRD.

In Chapter 4, the carbon content in the copper phosphide-carbon composite (CuP_x-Cy) is optimized based on the electrochemical performance evaluated by electrochemical impedance spectroscopy (EIS), galvanostatic intermittent titration technique (GITT), and scanning electron microscopy (SEM).

In Chapter 5, the electrochemical performance of vanadium phosphide-phosphorus composite (V_4P_7/5P) is explored at 25 and 90 °C using the IL and compared with that in an organic electrolyte at room temperature. The charge-discharge mechanism is elucidated by *ex-situ* XRD.

In Chapter 6, the preparation conditions of vanadium diphosphide (VP_2) are optimized and its electrochemical behavior is investigated. The charge-discharge mechanism is observed by employing XRD, XAS, and NMR.

In Chapter 7, the electrochemical behavior of an amorphous silicon diphosphide-carbon composite (SiP_2/C) with 20 and 30 wt% carbon is reported.

Chapter 8 summarizes the entire thesis and describes future prospects related to this work.

Table 1-1 Comparison of the standard electrode potential, abundance, and cost of Li and Na [15-17, 19].

	Li	**Na**
$E^{o}(M^{+}/M)$vs. SHE / V	−3.04	−2.71
Abundance / µg (g-crust)$^{-1}$ µg (dm^{3}-seawater)$^{-1}$	13/180	23,000 /10,780,000
Cost / \$ ton-carbonates)$^{-1}$	13,900	150

Table 1-2 Comparison of the final sodiated product, electrical conductivity, theoretical capacity, and volume change of several alloy-based elements reported as negative electrode for NIBs.

Element	**Final sodiated product**	**Electrical conductivity at 20 °C S cm^{-1}**	**Theoretical capacity mA h g^{-1}**	**Volume change Δ*V* %**	**Ref.**
Ge	NaGe	1.0×10^{-2}	369	126	[79]
Sn	$Na_{15}Sn_4$	9.0×10^{4}	847	424	[143]
Pb	$Na_{3.75}Pb$	4.5×10^{4}	485	387	[80]
Red P	Na_3P	1.0×10^{-14}	2596	299	[84]
As	Na_2As	3.3×10^{4}	1072	200	[144]
Sb	Na_3Sb	2.5×10^{4}	660	293	[145]
Bi	Na_3Bi	7.7×10^{3}	385	253	[81]

Table 1-3 Specifications of negative electrode materials in IL electrolytes.

Cell configration	**Electrolytes**	**Mass loading / mg cm^{-2}**	**Temp. / °C**	**1st cycle discharge capacity @ current (coul. eff.) / mA h g^{-1} @ mA g^{-1}**	**Rate Capability / mA h g^{-1} (current density)**	**Cycleability**	**Ref.**
Na/3-D CF	Na[FSA]-[C$_3$C$_1$pyrr][FSA]	–	25	235 @ 30 (40%)	115 (1000 mA g^{-1})	85% (250 cycles)	[132]
			60	–	–	80% (250 cycles)	
Na/Semi-graphitic HC	0.5 M Na[TFSA]-[C$_3$C$_1$pyrr][TFSA] + 2% VEC	–	30	178 @ 74.2 (91%)	44 (1860 mA g^{-1})	100% (55 cycles)	[146]
Na/HC	20 mol% Na[FSA]-[C$_3$C$_1$pyrr][FSA]	–	0	48 @ 20 (–)	–	–	[134]
			25	193 @ 20 (–)	44 (200 mA g^{-1})	>100% (500 cycles)	
			90	277 @ 20 (78.5%)	230 (1000 mA g^{-1})	84% (500 cycles)	
Na/Anatase TiO$_2$	10% mol Na[TFSA]-[C$_3$C$_1$pyrr][FSA]	1.4–1.6	25	159 @ 33.5 (43%)	47 (3350 mA g^{-1})	98% (80 cycles)	[135]
Na/Nb doped rutile TiO$_2$	Na[FSA]-[C$_3$C$_1$pyrr][FSA]	–	30	110 @ 50 (–)	–	–	[137]
	Na[FSA]-[C$_3$C$_1$pyrr][FSA]		60	180 @ 50 (–)	–	97% (350 cycles)	
	Na[FSA]-PC		30	120 @ 50 (–)	–	–	
	Na[FSA]-PC		60	200 @ 50 (–)	–	91% (350 cycles)	
Na/TiO$_2$-Fe$_2$O$_3$	20 mol% Na[FSA]-[C$_3$C$_1$pyrr][FSA]	–	90	386 @ 10 (52%)	91 (2000 mA g^{-1})	80% (300 cycles)	[136]
Na/FeTiO$_3$-C	20 mol% Na[FSA]-[C$_3$C$_1$pyrr][FSA]	0.8–1.3	25	120 @ 10 (–)	–	–	[147]
	20 mol% Na[FSA]-[C$_3$C$_1$pyrr][FSA]		90	390 @ 10 (46.8%)	256 (2000 mA g^{-1})	113% (2000 cycles)	
	Na[PF$_6$]-EC/DMC		25	150 @ 10 (–)	–	–	
Na/TiO$_2$-C	20 mol% Na[FSA]-[C$_3$C$_1$pyrr][FSA]	1–2	25	143 @ 10 (–)	–	–	[148]
	20 mol% Na[FSA]-[C$_3$C$_1$pyrr][FSA]		90	340 @ 10 (45%)	93 (2000 mA g^{-1})	79% (1000 cycles)	
	Na[PF$_6$]-EC/DMC		25	114 @ 10 (–)	–	–	
Na/Sn film	56 mol% Na[FSA]-K[FSA]	–	90	729 @ 0.619* (92.3 %)	–	66% (30 cycles)	[77]
Na/Sn-Fe film	56 mol% Na[FSA]-K[FSA]	0.76	90	443 @ 84.7 (71%)	–	43% (100 cycles)	[138]
Na/Sn-Cu film	56 mol% Na[FSA]-K[FSA]	0.88–1.07	90	100 @ 84.7 (62.5%)	70 (847 mA g^{-1})	100% (1000 cycles)	[140]
Na/Sn-Ni film	56 mol% Na[FSA]-K[FSA]	0.67–0.85	90	605 @ 84.7 (86.4%)	–	56% (100 cycles)	[139]
Na/P-AB	0.25 M Na[FSA]-[C$_3$C$_1$pyrr][FSA]	0.47–0.56	–	1595 @ 125 (72.3%)	–	93% (80 cycles)	[133]
	Na[PF$_6$]-PC		–	1768 @ 125 (76.3%)	–	26% (80 cycles)	
	Na[PF$_6$]-EC/DEC		–	1755 @ 125 (77.3%)	–	30% (80 cycles)	
	Na[PF$_6$]-EC/PC/3DEC		–	1654 @ 125 (75.8%)	–	–	
Na/Black P	Na[TFSA]-[C$_{(10201)}$C$_1$][FSA]	–	30	800 @ 50 (–)	–	38% (100 cycles)	[149]
	Na[TFSI]-[C$_2$C$_1$im][FSA]		30	1072 @ 50 (–)	–	–	
	Na[TFSA]-PC		30	1500 @ 50 (–)	–	7% (40 cycles)	
Na/InP	Na[FSA]-[C$_3$C$_1$pyrr][FSA]	0.8–1	30	476 @ 50 (78.7%)	–	105% (100 cycles)	[150]
Na/CuP$_2$	Na[FSA]-[C$_3$C$_1$pyrr][FSA]	0.8–1	30	758 @ 50 (72.7%)	–	SCD	[150]
Na/GeP	Na[FSA]-[C$_3$C$_1$pyrr][FSA]	0.8–1	30	798 @ 50 (87.5%)	–	SCD	[150]

Na/GeP$_5$	Na[FSA]-[C$_3$C$_1$pyrr][FSA]	0.8–1	30	963 @ 50 (85.6%)	–	SCD	[150]
Na/SiP	Na[FSA]-[C$_3$C$_1$pyrr][FSA]	0.8–1	30	522 @ 50 (71.5%)	–	SCD	[150]
Na/LaP	Na[FSA]-[C$_3$C$_1$pyrr][FSA]	0.8–1	30	12 @ 50 (7.4%)	–	–	[150]
Na/Sn$_4$P$_3$	Na[FSA]-[C$_3$C$_1$pyrr][FSA]	1.2	0	220 @ 100 (55.9%)		–	[151]
		1.6	30	670 @ 50 (83.5%)	520 (1000 mA g^{-1})	112% (200 cycles)	[141]
		1.2	60	976 @ 100 (84.6%)	250 (3000 mA g^{-1})	–	[151]
		1.2	90	1057 @ 100 (82.5%)	230 (3000 mA g^{-1})	–	[151]
Na/SnP$_3$	Na[FSA]-[C$_3$C$_1$pyrr][FSA]	1.6	30	1100 @ 50 (88.4%)	–	SCD	[141]
Na/Sb$_2$S$_3$-graphene	Na[ClO$_4$]-PC	1–1.2	25	710 @ 50 (52%)	340 (1500 mA g^{-1})	48% (100 cycles)	[152]
	Na[ClO$_4$]-PC/FEC		25	710 @ 50 (60%)	285 (1500 mA g^{-1})	83% (100 cycles)	
	Na[ClO$_4$]-EC/DEC		25	560 @ 50 (48%)	55 (1500 mA g^{-1})	40% (100 cycles)	
	Na[ClO$_4$]-EC/DEC/ FEC		25	580 @ 50 (55%)	150 (1500 mA g^{-1})	69% (100 cycles)	
	Na[FSA]-[C$_3$C$_1$pyrr][FSA]		25	660 @ 50 (65%)	240 (1500 mA g^{-1})	96% (100 cycles)	
	Na[ClO$_4$]-PC/FEC		60	610 @ 50 (50%)	120 (1500 mA g^{-1})	43% (100 cycles)	
	Na[FSA]-[C$_3$C$_1$pyrr][FSA]		60	760 @ 50 (75%)	420 (1500 mA g^{-1})	95% (100 cycles)	
Na/SnO$_2$-graphene	Na[ClO$_4$]-PC/FEC	1–1.2	25	505 @ 20 (–)	197 (1000 mA g^{-1})	73% (100 cycles)	[142]
	Na[ClO$_4$]-EC/PC		25	500 @ 20 (–)	310 (1000 mA g^{-1})	71% (100 cycles)	
	Na[ClO$_4$]-EC/PC/FEC		25	505 @ 20 (–)	237 (1000 mA g^{-1})	88% (100 cycles)	
	Na[FSA]-[C$_3$C$_1$pyrr][FSA]		25	410 @ 20 (–)	148 (1000 mA g^{-1})	99% (100 cycles)	
	Na[ClO$_4$]-EC/PC/FEC		60	505 @ 20 (–)	–	59% (100 cycles)	
	Na[FSA]-[C$_3$C$_1$pyrr][FSA]		60	600 @ 20 (–)	330 (1000 mA g^{-1})	96% (100 cycles)	
Na/Na$_2$DBQ-OMC	Na[ClO$_4$]-EC/PC	0.3–0.6	22	–	–	38% (50 cycles)	[153]
	Na[FSA]-EC/PC		22	–	–	–	
	Na[FSA]-[C$_3$C$_1$pyrr][FSA]		22	145 @ 25 (43%)	–	–	
	Na[FSA]-[C$_3$C$_1$pyrr][FSA]		60	277 @ 25 (–)	175 (300 mA g^{-1})	88% (300 cycles)	

* mA cm^{-2}; SCD = severe capacity degradation; FEC = 5% by volume; ratio of organic solvents = 1:1 v/v; molarity of electrolyte = 1 mol dm^{-3} unless specified

** 3-D CF = 3 dimensional carbon fiber

*** TFSA = bis(trifluoromethylsulfonyl)amide, FSA = bis(fluorosulfonyl)amide), C$_2$C$_1$im = 1-ethyl-3-methylimidazolium, C$_3$C$_1$pyrr = *N*-methyl-*N*-propylpyrrolidinium,, C$_{(10201)}$C$_1$ = 1-((2-methoxyethoxy)methyl)-1-methylpyrrolidinium

Table 1-4. Comparison of ionic conductivities of $NaClO_4$-PC organic and Na[FSA]-[C_3C_1pyrr][FSA] ionic liquid electrolytes [118, 119].

Electrolyte	**Ionic conductivity / mS cm^{-1}**
1 mol dm^{-3} $NaClO_4$-PC [118]	6.0 (298 K)
20 mol% Na[FSA]-[C_3C_1pyrr][FSA] [119]	3.6 (298 K) 18.4 (358 K)

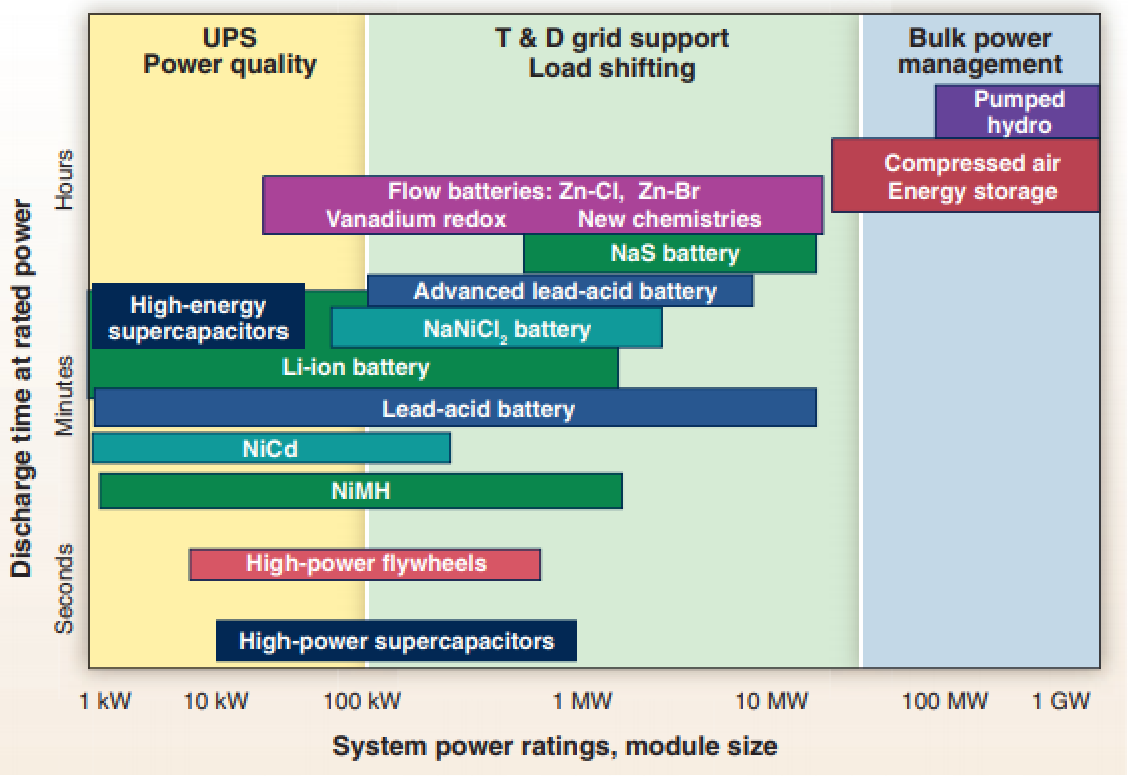

Figure 1-1 Comparison of discharge time and power rating for various EES technologies [1].

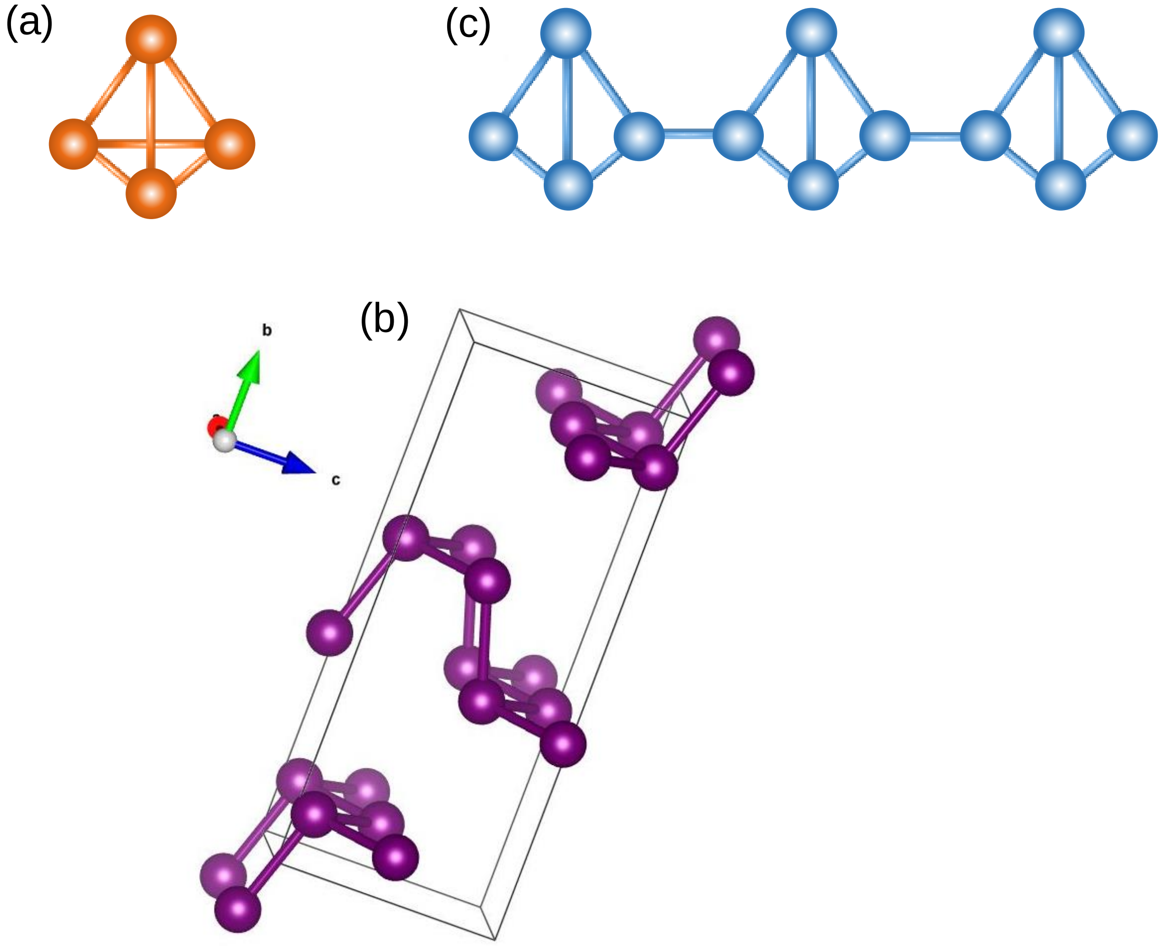

Figure 1-2 Schematic of the structures of (a) white phosphorus, (b) black phosphorus, and (c) red phosphorus.

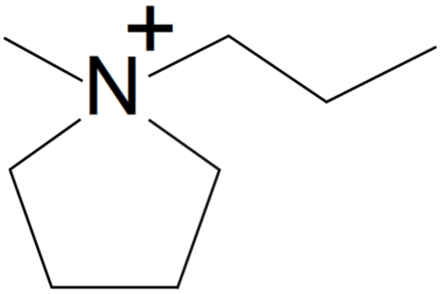

Figure 1-3 Structure of *N*-methyl-*N*-propylpyrrolidinium cation ($C_3C_1pyrr^+$).

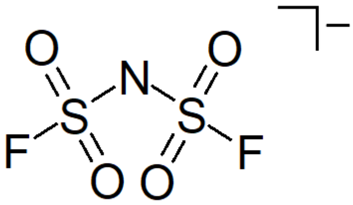

Figure 1-4 Structure of bis(fluorosulfonyl)amide anion (FSA^-).

References

[1] Z. Yang, J. Zhang, M.C.W. Kintner-Meyer, X. Lu, D. Choi, J.P. Lemmon, J. Liu, Chem. Rev., 111 (2011) 3577-3613.

[2] B. Dunn, H. Kamath, J.-M. Tarascon, Science, 334 (2011) 928.

[3] O. Ellabban, H. Abu-Rub, F. Blaabjerg, Renew. Sust. Energy Rev., 39 (2014) 748-764.

[4] H. Chen, T.N. Cong, W. Yang, C. Tan, Y. Li, Y. Ding, Prog. Nat. Sci., 19 (2009) 291-312.

[5] H. Qian, J. Zhang, J. Lai, W. Yu, IEEE Trans. Power Electron., 26 (2011) 886-896.

[6] J. Tollefson, Nature, 456 (2008) 436.

[7] L. Li, C. Chen, A. Yu, Sci. China Chem., 60 (2017) 1402-1412.

[8] G.J. Zhao, W.L. Wu, W.B. Qiu, S.L. Liu, G. Wang, Adv. Mater. Res., 528 (2012) 202-205.

[9] G. Nikiforidis, M.C.M. van de Sanden, M.N. Tsampas, RSC Adv., 9 (2019) 5649-5673.

[10] J.M. Tarascon, M. Armand, Nature, 414 (2001) 359-367.

[11] M.S. Whittingham, Chem. Rev., 104 (2004) 4271-4302.

[12] J.B. Goodenough, K.-S. Park, J. Am. Chem. Soc., 135 (2013) 1167-1176.

[13] V. Etacheri, R. Marom, R. Elazari, G. Salitra, D. Aurbach, Energy Environ. Sci., 4 (2011) 3243-3262.

[14] N. Nitta, F. Wu, J.T. Lee, G. Yushin, Mater. Today, 18 (2015) 252-264.

[15] S.R. Taylor, S.M. McLennan, The continental crust: Its composition and evolution (1985) United States.

[16] Y. Nozaki, EOS. Trans, 78 (1997) 221.

[17] U.S.G. Survey, Mineral Commodity Summaries 2019, Lithium, (2019) 98.

[18] J.-M. Tarascon, Nat. Chem., 2 (2010) 510-510.

[19] U.S.G. Survey, Mineral Commodity Summaries 2019, Soda Ash, (2019) 154.

[20] J.L. Sudworth, J. Power Sources, 11 (1984) 143-154.

[21] J. Coetzer, J. Power Sources, 18 (1986) 377-380.

[22] K.B. Hueso, M. Armand, T. Rojo, Energy Environ. Sci., 6 (2013) 734-749.

[23] S. Song, Z. Wen, Q. Zhang, Y. Liu, J. Power Sources, 195 (2010) 384-388.

[24] L.W. Shacklette, J. Electrochem. Soc., 135 (1988) 2669.

[25] D.A. Stevens, J.R. Dahn, J. Electrochem. Soc., 147 (2000) 1271.

[26] M.D. Slater, D. Kim, E. Lee, C.S. Johnson, Adv. Funct. Mater., 23 (2013) 947-958.

[27] S.P. Ong, V.L. Chevrier, G. Hautier, A. Jain, C. Moore, S. Kim, X. Ma, G. Ceder, Energy Environ. Sci., 4 (2011) 3680-3688.

[28] Y. Nishi, J. Power Sources, 100 (2001) 101-106.

[29] P. Ge, M. Fouletier, Solid State Ionics, 28-30 (1988) 1172-1175.

[30] H. Moriwake, A. Kuwabara, C.A.J. Fisher, Y. Ikuhara, RSC Advances, 7 (2017) 36550-36554.

[31] K. Nobuhara, H. Nakayama, M. Nose, S. Nakanishi, H. Iba, J. Power Sources, 243 (2013) 585-587.

[32] B. Jache, P. Adelhelm, Angew. Chem. Int. Ed., 53 (2014) 10169-10173.

[33] E. Irisarri, A. Ponrouch, M.R. Palacin, J. Electrochem. Soc., 162 (2015) A2476-A2482.

[34] B. Xiao, T. Rojo, X. Li, ChemSusChem, 12 (2019) 133-144.

[35] C. Bommier, W. Luo, W.-Y. Gao, A. Greaney, S. Ma, X. Ji, Carbon, 76 (2014) 165-174.

[36] R. Morita, K. Gotoh, M. Fukunishi, K. Kubota, S. Komaba, N. Nishimura, T. Yumura, K. Deguchi, S. Ohki, T. Shimizu, H. Ishida, J. Mater. Chem. A, 4 (2016) 13183-13193.

[37] J. Ding, H. Wang, Z. Li, A. Kohandehghan, K. Cui, Z. Xu, B. Zahiri, X. Tan, E.M. Lotfabad, B.C. Olsen, D. Mitlin, ACS Nano, 7 (2013) 11004-11015.

[38] E.M. Lotfabad, J. Ding, K. Cui, A. Kohandehghan, W.P. Kalisvaart, M. Hazelton, D. Mitlin, ACS Nano, 8 (2014) 7115-7129.

[39] K.-l. Hong, L. Qie, R. Zeng, Z.-q. Yi, W. Zhang, D. Wang, W. Yin, C. Wu, Q.-j. Fan, W.-x. Zhang, Y.-h. Huang, J. Mater. Chem. A, 2 (2014) 12733-12738.

[40] L. Qie, W. Chen, X. Xiong, C. Hu, F. Zou, P. Hu, Y. Huang, Adv. Sci., 2 (2015) 1500195.

[41] H. Hou, L. Shao, Y. Zhang, G. Zou, J. Chen, X. Ji, Adv. Sci., 4 (2017) 1600243.

[42] Z. Li, L. Ma, T.W. Surta, C. Bommier, Z. Jian, Z. Xing, W.F. Stickle, M. Dolgos, K. Amine, J. Lu, T. Wu, X. Ji, ACS Energy Lett., 1 (2016) 395-401.

[43] M.S. Whittingham, J. Electrochem. Soc., 123 (1976) 315.

[44] K. Mizushima, P.C. Jones, P.J. Wiseman, J.B. Goodenough, Mater. Res. Bull., 15 (1980) 783-789.

[45] K.M. Colbow, J.R. Dahn, R.R. Haering, J. Power Sources, 26 (1989) 397-402.

[46] M. Odziomek, F. Chaput, A. Rutkowska, K. Świerczek, D. Olszewska, M. Sitarz, F. Lerouge, S. Parola, Nat. Commun., 8 (2017) 15636.

[47] D. Deng, M.G. Kim, J.Y. Lee, J. Cho, Energy Environ. Sci., 2 (2009) 818-837.

[48] Y. Mei, Y. Huang, X. Hu, J. Mater. Chem. A, 4 (2016) 12001-12013.

[49] S. Guo, J. Yi, Y. Sun, H. Zhou, Energy Environ. Sci., 9 (2016) 2978-3006.

[50] H. Xiong, M.D. Slater, M. Balasubramanian, C.S. Johnson, T. Rajh, J. Phys. Chem. Lett., 2 (2011) 2560-2565.

[51] S.-T. Myung, N. Takahashi, S. Komaba, C.S. Yoon, Y.-K. Sun, K. Amine, H. Yashiro, Adv. Funct. Mater., 21 (2011) 3231-3241.

[52] Y. Ge, H. Jiang, J. Zhu, Y. Lu, C. Chen, Y. Hu, Y. Qiu, X. Zhang, Electrochim. Acta, 157 (2015) 142-148.

[53] Y. Ge, H. Jiang, K. Fu, C. Zhang, J. Zhu, C. Chen, Y. Lu, Y. Qiu, X. Zhang, J. Power Sources, 272 (2014) 860-865.

[54] Z. Yan, L. Liu, J. Tan, Q. Zhou, Z. Huang, D. Xia, H. Shu, X. Yang, X. Wang, J. Power Sources, 269 (2014) 37-45.

[55] W. Wang, C. Yu, Z. Lin, J. Hou, H. Zhu, S. Jiao, Nanoscale, 5 (2013) 594-599.

[56] D. Su, S. Dou, G. Wang, Chem. Mater., 27 (2015) 6022-6029.

[57] L. Wu, D. Bresser, D. Buchholz, G.A. Giffin, C.R. Castro, A. Ochel, S. Passerini, Adv. Energy Mater., 5 (2015) 1401142.

[58] L. Wu, D. Bresser, D. Buchholz, S. Passerini, J. Electrochem. Soc., 162 (2014) A3052-A3058.

[59] P. Senguttuvan, G. Rousse, V. Seznec, J.-M. Tarascon, M.R. Palacín, Chem. Mater., 23 (2011) 4109-4111.

[60] A. Rudola, K. Saravanan, S. Devaraj, H. Gong, P. Balaya, Chem. Commun., 49 (2013) 7451-7453.

[61] S.H. Woo, Y. Park, W.Y. Choi, N.-S. Choi, S. Nam, B. Park, K.T. Lee, J. Electrochem. Soc., 159 (2012) A2016-A2023.

[62] Y. Sun, L. Zhao, H. Pan, X. Lu, L. Gu, Y.-S. Hu, H. Li, M. Armand, Y. Ikuhara, L. Chen, X. Huang, Nat. Commun., 4 (2013) 1870.

[63] P. Senguttuvan, G. Rousse, M.E. Arroyo y de Dompablo, H. Vezin, J.M. Tarascon, M.R. Palacín, J. Am. Chem. Soc., 135 (2013) 3897-3903.

[64] P. Senguttuvan, G. Rousse, H. Vezin, J.M. Tarascon, M.R. Palacín, Chem. Mater., 25 (2013) 2391-2393.

[65] Z. Wang, J. Liang, K. Fan, X. Liu, C. Wang, J. Ma, Front. Chem., 6 (2018) 1-8.

[66] M. Lao, Y. Zhang, W. Luo, Q. Yan, W. Sun, S.X. Dou, Adv. Mater., 29 (2017) 1700622.

[67] H. Tan, D. Chen, X. Rui, Y. Yu, Adv. Funct. Mater., 29 (2019) 1808745.

[68] L. Ji, M. Gu, Y. Shao, X. Li, M.H. Engelhard, B.W. Arey, W. Wang, Z. Nie, J. Xiao, C. Wang, J.-G. Zhang, J. Liu, Adv. Mater., 26 (2014) 2901-2908.

[69] L. Li, Y. Zheng, S. Zhang, J. Yang, Z. Shao, Z. Guo, Energy Environ. Sci., 11 (2018) 2310-2340.

[70] J. Song, Z. Yu, M.L. Gordin, S. Hu, R. Yi, D. Tang, T. Walter, M. Regula, D. Choi, X. Li, A. Manivannan, D. Wang, Nano Lett., 14 (2014) 6329-6335.

[71] Z. Huang, H. Hou, C. Wang, S. Li, Y. Zhang, X. Ji, Chem. Mater., 29 (2017) 7313-7322.

[72] L. Wang, J. Światowska, S. Dai, M. Cao, Z. Zhong, Y. Shen, M. Wang, Mater. Today Energy, 11 (2019) 46-60.

[73] F. Klein, B. Jache, A. Bhide, P. Adelhelm, Phys. Chem. Chem. Phys., 15 (2013) 15876-15887.

[74] V.L. Chevrier, G. Ceder, J. Electrochem. Soc., 158 (2011) A1011.

[75] S. Komaba, Y. Matsuura, T. Ishikawa, N. Yabuuchi, W. Murata, S. Kuze, Electrochem. Commun., 21 (2012) 65-68.

[76] J.W. Wang, X.H. Liu, S.X. Mao, J.Y. Huang, Nano Lett., 12 (2012) 5897-5902.

[77] T. Yamamoto, T. Nohira, R. Hagiwara, A. Fukunaga, S. Sakai, K. Nitta, S. Inazawa, J. Power Sources, 237 (2013) 98-103.

[78] D.Y.W. Yu, P.V. Prikhodchenko, C.W. Mason, S.K. Batabyal, J. Gun, S. Sladkevich, A.G. Medvedev, O. Lev, Nat. Commun., 4 (2013) 2922.

[79] L. Baggetto, J.K. Keum, J.F. Browning, G.M. Veith, Electrochem. Commun., 34 (2013) 41-44.

[80] A. Darwiche, R. Dugas, B. Fraisse, L. Monconduit, J. Power Sources, 304 (2016) 1-8.

[81] C. Wang, L. Wang, F. Li, F. Cheng, J. Chen, Adv. Mater., 29 (2017) 1702212.

[82] H. Hou, M. Jing, Y. Yang, Y. Zhu, L. Fang, W. Song, C. Pan, X. Yang, X. Ji, ACS Appl. Mater. Interfaces, 6 (2014) 16189-16196.

[83] L. Xiao, Y. Cao, J. Xiao, W. Wang, L. Kovarik, Z. Nie, J. Liu, Chem. Commun., 48 (2012) 3321-3323.

[84] Y. Kim, Y. Park, A. Choi, N.-S. Choi, J. Kim, J. Lee, J.H. Ryu, S.M. Oh, K.T. Lee, Adv. Mater., 25 (2013) 3045-3049.

[85] H.S. Mason, Chem. Eng. News, 23 (1945) 40.

[86] Y. Zhu, Y. Wen, X. Fan, T. Gao, F. Han, C. Luo, S.-C. Liou, C. Wang, ACS Nano, 9 (2015) 3254-3264.

[87] M. Dahbi, N. Yabuuchi, M. Fukunishi, K. Kubota, K. Chihara, K. Tokiwa, X.-f. Yu, H. Ushiyama, K. Yamashita, J.-Y. Son, Y.-T. Cui, H. Oji, S. Komaba, Chem. Mater., 28 (2016) 1625-1635.

[88] J. Sun, H.-W. Lee, M. Pasta, H. Yuan, G. Zheng, Y. Sun, Y. Li, Y. Cui, Nat. Nanotechnol., 10 (2015) 980-985.

[89] G.-L. Xu, Z. Chen, G.-M. Zhong, Y. Liu, Y. Yang, T. Ma, Y. Ren, X. Zuo, X.-H. Wu, X. Zhang, K. Amine, Nano Lett., 16 (2016) 3955-3965.

[90] Y. Liu, Q. Liu, A. Zhang, J. Cai, X. Cao, Z. Li, P.D. Asimow, C. Zhou, ACS Nano, 12 (2018) 8323-8329.

[91] H. Liu, A.T. Neal, Z. Zhu, Z. Luo, X. Xu, D. Tománek, P.D. Ye, ACS Nano, 8 (2014) 4033-4041.

[92] C.R. Ryder, J.D. Wood, S.A. Wells, Y. Yang, D. Jariwala, T.J. Marks, G.C. Schatz, M.C. Hersam, Nat. Chem., 8 (2016) 597-602.

[93] Z. Huang, H. Hou, Y. Zhang, C. Wang, X. Qiu, X. Ji, Adv. Mater., 29 (2017) 1702372.

[94] J. Qian, X. Wu, Y. Cao, X. Ai, H. Yang, Angew. Chem. Int. Ed., 52 (2013) 4633-4636.

[95] W.-J. Li, S.-L. Chou, J.-Z. Wang, H.-K. Liu, S.-X. Dou, Nano Lett., 13 (2013) 5480-5484.

[96] W. Li, Z. Yang, M. Li, Y. Jiang, X. Wei, X. Zhong, L. Gu, Y. Yu, Nano Lett., 16 (2016) 1546-1553.

[97] Y. Liu, A. Zhang, C. Shen, Q. Liu, J. Cai, X. Cao, C. Zhou, Nano Res., 11 (2018) 3780-3790.

[98] Y. Liu, A. Zhang, C. Shen, Q. Liu, X. Cao, Y. Ma, L. Chen, C. Lau, T.-C. Chen, F. Wei, C. Zhou, ACS Nano, 11 (2017) 5530-5537.

[99] L. Pei, Q. Zhao, C. Chen, J. Liang, J. Chen, ChemElectroChem, 2 (2015) 1652-1655.

[100] Y. Liu, N. Zhang, X. Liu, C. Chen, L.-Z. Fan, L. Jiao, Energy Storage Mater., 9 (2017) 170-178.

[101] M. Fan, Y. Chen, Y. Xie, T. Yang, X. Shen, N. Xu, H. Yu, C. Yan, Adv. Funct. Mater., 26 (2016) 5019-5027.

[102] J. Fullenwarth, A. Darwiche, A. Soares, B. Donnadieu, L. Monconduit, J. Mater. Chem. A, 2 (2014) 2050-2059.

[103] J. Saddique, X. Zhang, T. Wu, X. Wang, X. Cheng, H. Su, S. Liu, L. Zhang, G. Li, Y. Zhang, H. Yu, ACS Appl. Energy Mater., 2 (2019) 2223-2229.

[104] S.-O. Kim, A. Manthiram, Chem. Commun., 52 (2016) 4337-4340.

[105] Y. Yin, L. Fan, Y. Zhang, N. Liu, N. Zhang, K. Sun, Nanoscale, 11 (2019) 7129-7134.

[106] Y. Lu, P. Zhou, K. Lei, Q. Zhao, Z. Tao, J. Chen, Adv. Energy Mater., 7 (2017) 1601973.

[107] K.-H. Nam, Y. Hwa, C.-M. Park, ACS Appl. Mater. Interfaces, 12 (2020) 15053-15062.

[108] W.-J. Li, Q.-R. Yang, S.-L. Chou, J.-Z. Wang, H.-K. Liu, J. Power Sources, 294 (2015) 627-632.

[109] W.-J. Li, S.-L. Chou, J.-Z. Wang, H.-K. Liu, S.-X. Dou, Chem. Commun., 51 (2015) 3682-3685.

[110] A.Y. Zavrazhnov, G.V. Semenova, E.Y. Proskurina, T.P. Sushkova, J. Therm. Anal. Calorim., 134 (2018) 475-481.

[111] X. Fan, J. Mao, Y. Zhu, C. Luo, L. Suo, T. Gao, F. Han, S.-C. Liou, C. Wang, Adv. Energy Mater., 5 (2015) 1500174.

[112] Y. Kim, Y. Kim, A. Choi, S. Woo, D. Mok, N.-S. Choi, Y.S. Jung, J.H. Ryu, S.M. Oh, K.T. Lee, Adv. Mater., 26 (2014) 4139-4144.

[113] J. Liu, S. Wang, K. Kravchyk, M. Ibáñez, F. Krumeich, R. Widmer, D. Nasiou, M. Meyns, J. Llorca, J. Arbiol, M.V. Kovalenko, A. Cabot, J. Mater. Chem. A, 6 (2018) 10958-10966.

[114] W. Li, L. Ke, Y. Wei, S. Guo, L. Gan, H. Li, T. Zhai, H. Zhou, J. Mater. Chem. A, 5 (2017) 4413-4420.

[115] W. Zhang, M. Dahbi, S. Amagasa, Y. Yamada, S. Komaba, Electrochem. Commun., 69 (2016) 11-14.

[116] S.-O. Kim, A. Manthiram, Chem. Mater., 28 (2016) 5935-5942.

[117] S. Boyanov, D. Zitoun, M. Ménétrier, J.C. Jumas, M. Womes, L. Monconduit, J. Phys. Chem. C, 113 (2009) 21441-21452.

[118] K. Kuratani, N. Uemura, H. Senoh, H.T. Takeshita, T. Kiyobayashi, J. Power Sources, 223 (2013) 175-182.

[119] K. Matsumoto, Y. Okamoto, T. Nohira, R. Hagiwara, J. Phys. Chem. C, 119 (2015) 7648-7655.

[120] M.B. Pinson, M.Z. Bazant, J. Electrochem. Soc., 160 (2013) A243-A250.

[121] M. Wang, L. Huai, G. Hu, S. Yang, F. Ren, S. Wang, Z. Zhang, Z. Chen, Z. Peng, C. Shen, D. Wang, J. Phys. Chem. C, 122 (2018) 9825-9834.

[122] M.-T.F. Rodrigues, F.N. Sayed, H. Gullapalli, P.M. Ajayan, J. Power Sources, 381 (2018) 107-115.

[123] M. Haruta, T. Okubo, Y. Masuo, S. Yoshida, A. Tomita, T. Takenaka, T. Doi, M. Inaba, Electrochim. Acta, 224 (2017) 186-193.

[124] T. Jaumann, J. Balach, M. Klose, S. Oswald, U. Langklotz, A. Michaelis, J. Eckert, L. Giebeler, Phys. Chem. Chem. Phys., 17 (2015) 24956-24967.

[125] R. Mogensen, D. Brandell, R. Younesi, ACS Energy Lett., 1 (2016) 1173-1178.

[126] Z.W. Seh, J. Sun, Y. Sun, Y. Cui, ACS Cent. Sci., 1 (2015) 449-455.

[127] C.-H. Wang, C.-H. Yang, J.-K. Chang, Chem. Commun., 52 (2016) 10890-10893.

[128] K. Matsumoto, T. Hosokawa, T. Nohira, R. Hagiwara, A. Fukunaga, K. Numata, E. Itani, S. Sakai, K. Nitta, S. Inazawa, J. Power Sources, 265 (2014) 36-39.

[129] J. Hwang, K. Matsumoto, R. Hagiwara, J. Phys. Chem. C, 122 (2018) 26857-26864.

[130] G.G. Eshetu, T. Diemant, M. Hekmatfar, S. Grugeon, R.J. Behm, S. Laruelle, M. Armand, S. Passerini, Nano Energy, 55 (2019) 327-340.

[131] G.G. Eshetu, S. Grugeon, H. Kim, S. Jeong, L. Wu, G. Gachot, S. Laruelle, M. Armand, S. Passerini, ChemSusChem, 9 (2016) 462-471.

[132] X.-F. Luo, A.S. Helal, C.-T. Hsieh, J. Li, J.-K. Chang, Nano Energy, 49 (2018) 515-522.

[133] M. Dahbi, M. Fukunishi, T. Horiba, N. Yabuuchi, S. Yasuno, S. Komaba, J. Power Sources, 363 (2017) 404-412.

[134] C. Ding, T. Nohira, R. Hagiwara, A. Fukunaga, S. Sakai, K. Nitta, Electrochim. Acta, 176 (2015) 344-349.

[135] L. Wu, A. Moretti, D. Buchholz, S. Passerini, D. Bresser, Electrochim. Acta, 203 (2016) 109-116.

[136] C.S. Ding, T. Nohira, R. Hagiwara, Sustain. Energy Fuels, 1 (2017) 371-376.

[137] H. Usui, Y. Domi, M. Shimizu, A. Imoto, K. Yamaguchi, H. Sakaguchi, J. Power Sources, 329 (2016) 428-431.

[138] T. Yamamoto, T. Nohira, R. Hagiwara, A. Fukunaga, S. Sakai, K. Nitta, Electrochim. Acta, 211 (2016) 234-244.

[139] T. Yamamoto, T. Nohira, R. Hagiwara, A. Fukunaga, S. Sakai, K. Nitta, Electrochim. Acta, 193 (2016) 275-283.

[140] T. Yamamoto, T. Nohira, R. Hagiwara, A. Fukunaga, S. Sakai, K. Nitta, S. Inazawa, Electrochim. Acta, 135 (2014) 60-67.

[141] H. Usui, Y. Domi, K. Fujiwara, M. Shimizu, T. Yamamoto, T. Nohira, R. Hagiwara, H. Sakaguchi, ACS Energy Lett., 2 (2017) 1139-1143.

[142] H.-C. Chen, J. Patra, S.-W. Lee, C.-J. Tseng, T.-Y. Wu, M.-H. Lin, J.-K. Chang, J. Mater. Chem. A, 5 (2017) 13776-13784.

[143] Y. Xu, Y. Zhu, Y. Liu, C. Wang, Adv. Energy Mater., 3 (2013) 128-133.

[144] Y.R. Lim, F. Shojaei, K. Park, C.S. Jung, J. Park, W.I. Cho, H.S. Kang, Nanoscale, 10 (2018) 7047-7057.

[145] H. Hou, M. Jing, Y. Yang, Y. Zhang, W. Song, X. Yang, J. Chen, Q. Chen, X. Ji, J. Power Sources, 284 (2015) 227-235.

[146] M. Arnaiz, P. Huang, J. Ajuria, T. Rojo, E. Goikolea, A. Balducci, Batteries & Supercaps, 1 (2018) 204-208.

[147] C. Ding, T. Nohira, R. Hagiwara, J. Power Sources, 388 (2018) 19-24.

[148] C. Ding, T. Nohira, R. Hagiwara, J. Mater. Chem. A, 3 (2015) 20767-20771.

[149] M. Shimizu, H. Usui, K. Yamane, T. Sakata, T. Nokami, T. Itoh, H. Sakaguchi, Int. J. Electrochem. Sci., 10 (2015) 10145-10156.

[150] H. Usui, Y. Domi, R. Yamagami, K. Fujiwara, H. Nishida, H. Sakaguchi, ACS Appl. Energy Mater., 1 (2018) 306-311.

[151] H. Usui, Y. Domi, H. Nishida, K. Yamaguchi, R. Yamagami, H. Sakaguchi, ChemistrySelect, 3 (2018) 8462-8467.

[152] C.-Y. Li, J. Patra, C.-H. Yang, C.-M. Tseng, S.B. Majumder, Q.-F. Dong, J.-K. Chang, ACS Sustain. Chem. Eng., 5 (2017) 8269-8276.

[153] B.E. Gurkan, Z. Qiang, Y.-M. Chen, Y. Zhu, B.D. Vogt, J. Electrochem. Soc., 164 (2017) H5093-H5099.

Chapter 2

Experimental

2.1 Apparatus and material handling

Handling of all the air-sensitive reagents and active materials, fabrication and disassembling of coin-cells, and packing of ball-milling vessels were carried out in a glove box (Miwa Manufacturing Co., Ltd., DBO-2LKH-HNBR) equipped with a gas purification system (Miwa Manufacturing Co., Ltd., MS3-P60S-N). The glove box was filled with argon gas (purity = 99.995%) and the atmosphere inside the glove box is maintained below the dew point of −90 °C monitored by a dew point meter (GE Panametrics Ltd., MTS5-311-10) and the oxygen concentration below 1 ppm monitored by an oxygen analyzer (GE Sensing & Inspection Technologies Co., Ltd., DF-150ε).

All the moisture sensitive materials such as ILs and electrode materials were dried in a vacuum line [1] prior to use. Figures 2-1 and 2-2 show the schematic diagram of the vacuum line and the drying vessel. The vacuum line was made of stainless steel (SUS316, 1/2 inch o.d.) and PFA tubes (tetrafluoroetylene-perfluoroalkylvinylether copolymer, 1/2 inch o.d.) connected with stainless steel joints and valves partly made of Kel-F (polychlorotrifluoroethylene) tip (Swagelok Co.). A thinner PFA tube (1/4 o.d.) was used to connect the drying vessel to the main section. The temperature of the drying vessel was controlled by heating silicone oil in the oil bath and magnetic stirrer. The vacuum was created by rotary vacuum pump (Shibaura Eletec Corp., RP-602; or ULVAC KIKO, Inc., GLD-136C). In order to prevent the volatiles from entering the pump, a cold trap made of Pyrex glass cooled down by liquid nitrogen was used. The pressure of the vacuum line was monitored by a Pirani gauge and confirmed to be 1 Pa prior to use.

The salts, Na[FSA] (Mitsubishi Materials Electronic Chemicals, Japan, purity >99%) and [C_3C_1pyrr][FSA] (Kanto Chemical, Japan, purity >99.9%), were dried in the vacuum line for 24 h at 80 °C followed by mixing them in a 20:80 molar ratio to prepare the IL electrolyte. The powders of red P (Wako Pure Chemical Industries, Japan, purity 98%) and other elements (Cu, V, Si) were stored in the glove box and weighed using an electronic scale balance (Sartorius Mechatronics Japan K.K., CP423S, CPA224S or CPA225D) to prepare electrode composites.

2.2 Synthesis of active materials

The elemental powders were ball-milled (Planetary Micro Mill Pulverisette 7, Fritsch, 20 mL grinding bowl and 3 mm zirconium oxide balls) under different conditions to obtain the desired product. Figure 2-3 shows the schematic diagram of ball-milling components. For the preparation of the carbon composite, the phosphides were ball-milled with acetylene black (AB) (Wako Pure Chemical Industries). Details will be described in each chapter.

2.3 Characterization techniques

2.3.1 X-ray diffraction (XRD)

Structures of the pristine and charge-discharged samples were characterized by XRD (Rigaku SmartLab diffractometer, CuKα; λ = 0.1541 nm, 40 kV−30 mA). The ex-situ XRD patterns were recorded after charging and discharging the cells to the desired voltage. Each sample was prepared by disassembling the cell followed by rinsing with tetrahydrofuran (Wako Pure Chemical Industries, water content ≤10 ppm), and vacuum-drying for 1 d at room temperature.

2.3.2 Field emission scanning electron microscopy (SEM) and energy dispersive X-ray spectroscopy (EDX)

The particle size, morphology, and elemental composition were analyzed by SEM (Hitachi SU-8020, Japan) and EDX (Horiba EMAXEvolution X-max, Japan). The method of sample preparation for SEM after cycling was the same as those for *ex-situ* XRD.

2.3.3 X-ray photoelectron spectroscopy (XPS)

States of bonding in target materials were analyzed by a JEOL XPS instrument (JPS-9010, Mg$K\alpha$, 10 kV−10 mA). The binding energy was corrected using the binding energy of indium metal foil (The Nilaco Corporation) as a reference (443.8 eV). The obtained spectra were fitted using the SpecSurf software (SpecSurf, ver. 1.8.3.7, JEOL, Ltd.). Argon etching was performed at an ion energy of 400 eV for different times according to the samples. The electrodes were washed with THF and dried in vacuum overnight prior to measuring *ex-situ* XPS after charging and discharging.

2.4 Electrochemical measurements

2.4.1 Electrode preparation and cell configurations

The negative electrode was prepared by mixing the active material, AB as a conductive additive, and a polyamide-imide (PAI) binder in *N*-methyl-2-pyrrolidone (NMP) (Wako Pure Chemical Industries, purity 99%) by a planetary centrifugal mixer (AR-100, Thinky). The resulting slurry was subsequently cast on Al foil and dried under vacuum at 90 °C for 10 h in an oven and in an airtight cell connected to a vacuum line at 110 °C overnight. The electrode was punched into discs of 10 mm with an area of 0.785 cm^2. A glass fiber filter (Whatman, GF-A, 260 mm in thickness and 16 mm in diameter) was used as a separator and a sodium metal disc (Sigma-Aldrich, purity 99.9%) was used as the counter electrode. The separator was impregnated with the IL at 80 °C under vacuum overnight prior to use. Coin cells (2032-type) were assembled in the glove box to measure the electrochemical performance of each material. Figure 2-4 shows the schematic drawing of the coin cell [1].

2.4.2 Galvanostatic charge-discharge test

The electrochemical behaviors of the prepared electrodes (i.e., charge-discharge, rate capability, and cyclability tests) were measured using an HJ1001SD8 charge–discharge test device (Hokuto Denko). The prepared coin cells were maintained at an open circuit voltage for >3 h prior to the tests. The operating temperature was controlled using ESPEC SU221 environmental test chamber.

2.4.3 Electrochemical impedance spectroscopy (EIS)

Electrochemical impedance spectra were recorded using a VSP potentiostat (Bio-Logic) at 25 and 90 °C over a frequency range of 100 kHz to 10 mHz with an amplitude of 20 mV. The cells were cycled at a rate of 100 mA g^{-1} for the first three cycles and 500 mA g^{-1} for subsequent cycles. The EIS spectra were measured at 0.5 V during the charging step of the nth cycle ($n = 2, 4, 11, 51$, and 101).

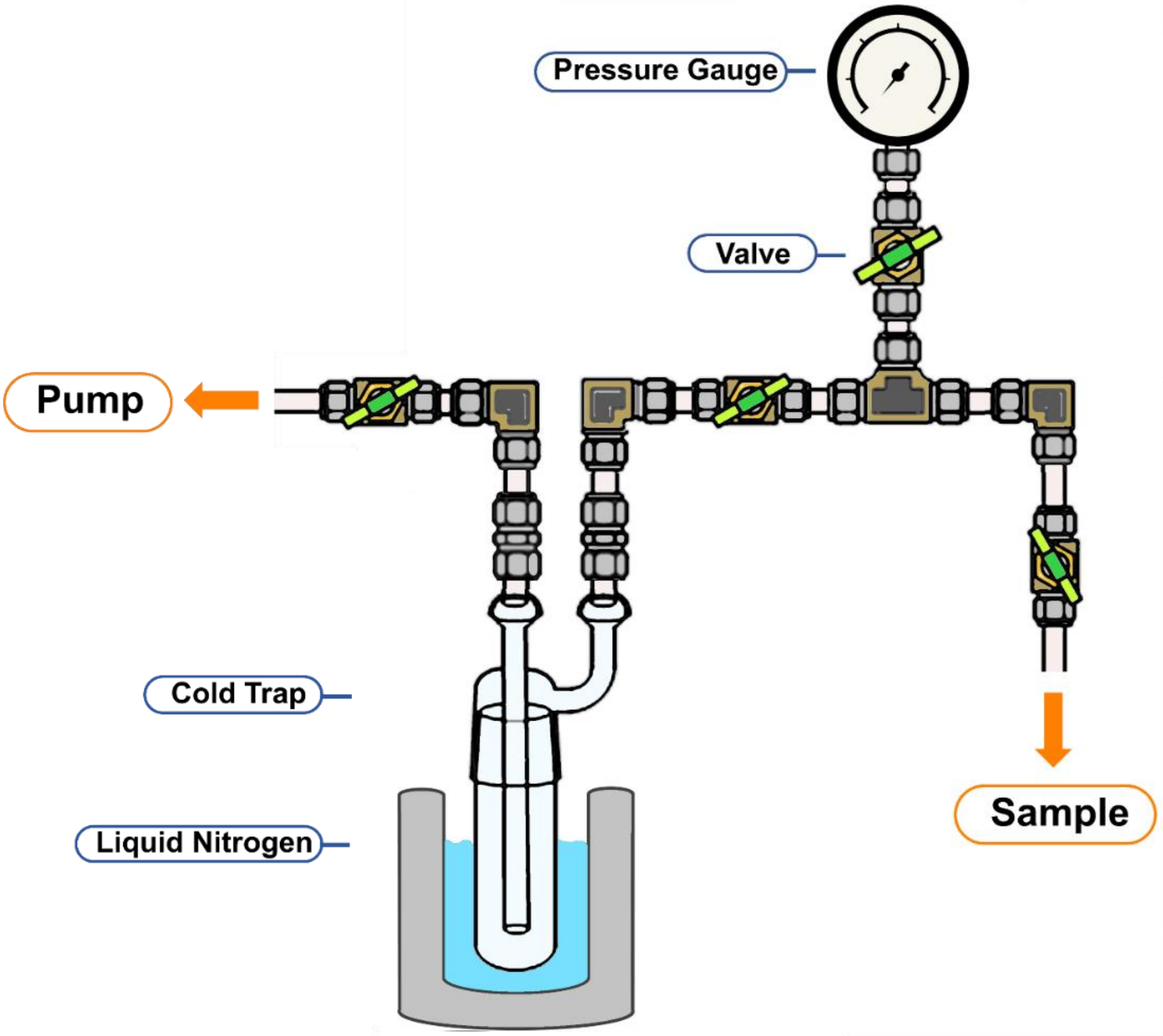

Figure 2-1 A schematic diagram of a vacuum line [1].

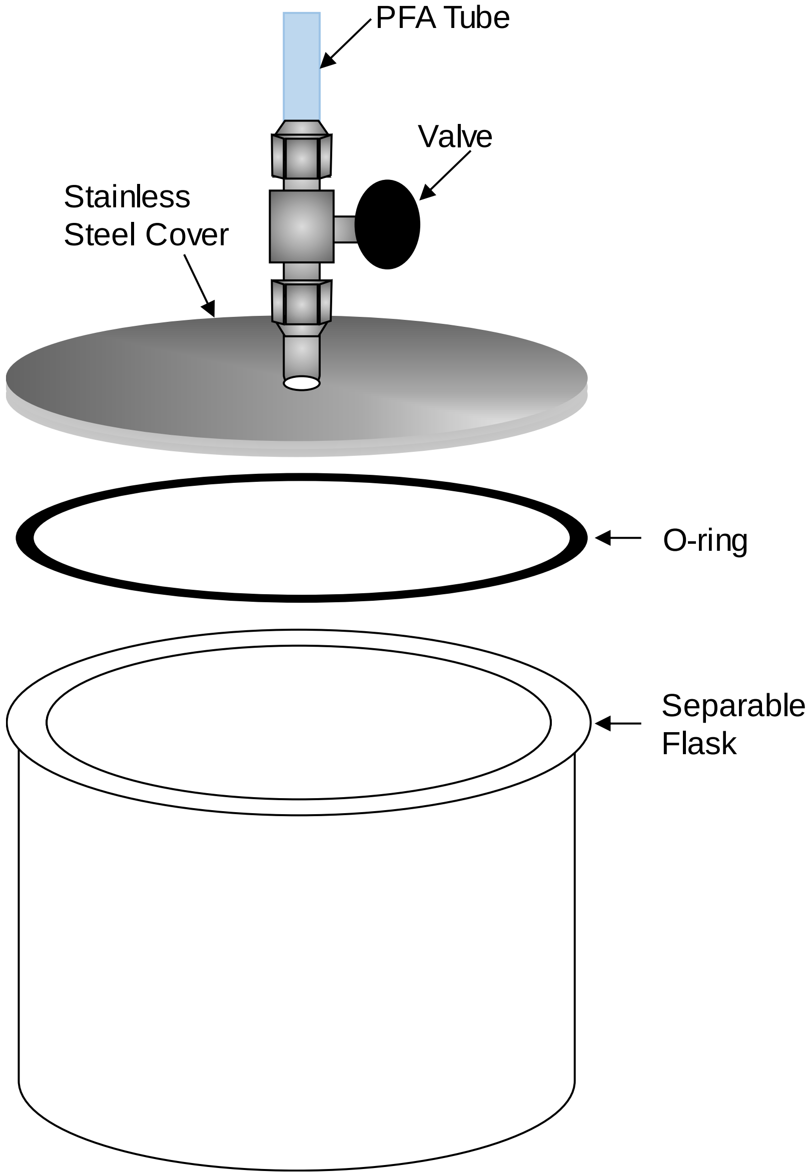

Figure 2-2 A schematic drawing of drying vessel from vacuum.

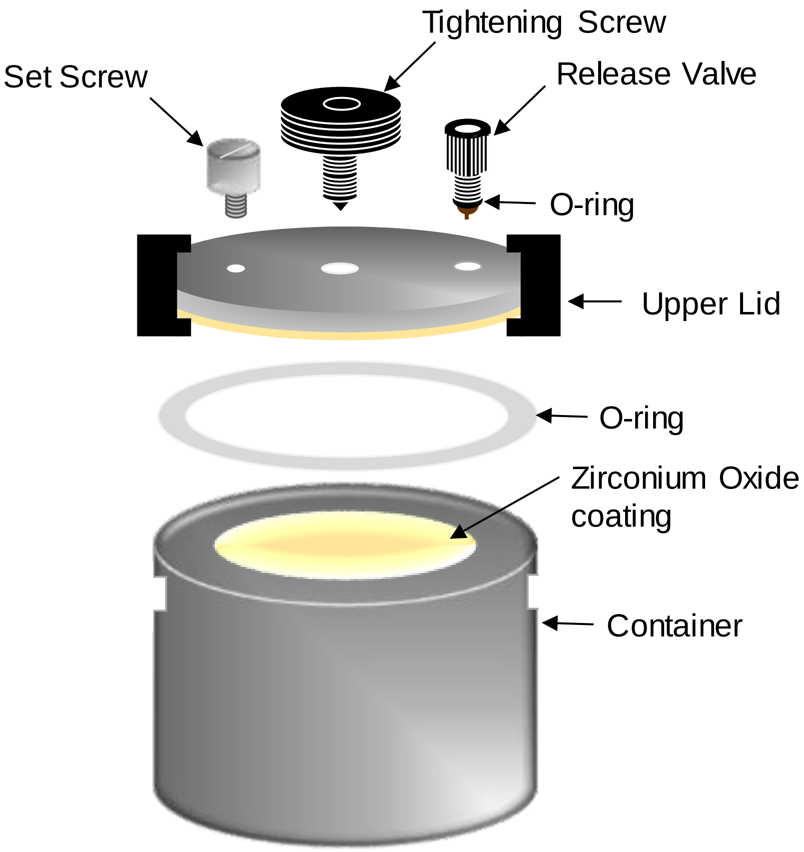

Figure 2-3 A schematic drawing of ball-milling components.

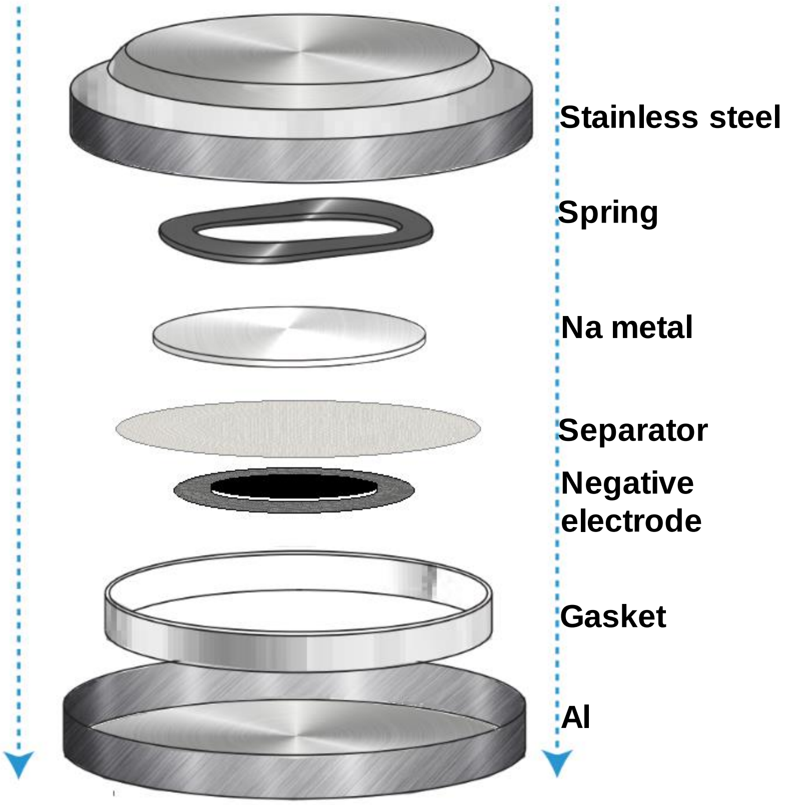

Figure 2-4 A schematic drawing of coin cell 2032.

References

[1] J. Hwang, PhD Thesis, Graduate School of Energy Science, Kyoto University (2019).

Chapter 3

Charge-discharge Behavior of CuP_2/C (80:20) Composite Negative Electrode

3.1 Introduction

Copper phosphide (CuP_2) has been extensively investigated as a negative electrode material for NIBs owing to the abundant constituent elements and high theoretical gravimetric (1290 mA h g^{-1}) as well as volumetric capacity (5534 mA hcm^{-3}). Sodiation following a conversion mechanism forms Na_3P and Cu and the subsequent desodiation provides CuP_2 [1]. After sodiation, Cu metal generally forms an electronically conductive matrix resulting in facile Na^+ diffusion, prevention of P agglomeration, and buffer for the large volume change. However, the reported studies have shown that carbon compositing of CuP_2 is essential for achieving decent cyclability and rate capabilities. Various kinds of carbon materials have been employed for carbon compositing. For instance, CuP_2 nanoparticles encapsulated in cross-linked hollow carbon sheets derived from the carbonization of polymerized dopamine hydrochloride delivered a reversible capacity of 491 mA h g^{-1} at 80 mA g^{-1} and capacity retention of 91% after 200 cycles [2]. In another report, graphene-encapsulated CuP_2 provided a high capacity of 804 mA h g^{-1} at 100 mA g^{-1} and good rate capability (508 mA h g^{-1} at 5000 mA g^{-1}) [3]. High energy ball-milling (HEBM) is a facile method to prepare carbon composites. The CuP_2/C composite with Super P carbon black (in the weight ratio of 70:30 w/w) was prepared by two-step HEBM [1]. The pristine CuP_2 was prepared in the first step of ball-milling at 400 rpm for 30 h and the carbon composite was in the second step at 400 rpm for 8 h. This composite exhibited a reversible capacity of 550 mA h g^{-1} at 50 mA g^{-1} in the first cycle and decent cyclability (430 mA h g^{-1} after 30 cycles). In 2016, S-O. Kim et. al. prepared CuP_2/AB by one-step HEBM at high speed of 1060 rpm for 3 h [4]. The carbon content was varied between 10-30 wt% and 20 wt% was proposed to be the optimized content from the electrochemical performance. The CuP_2/AB (80:20) delivered a capacity of 450 mA h g^{-1} at 50 mA g^{-1} in the first cycle and 95.5% capacity retention after 100 cycles. Although all the aforementioned reports demonstrated good cyclability and rate capability but the reported capacity is significantly lower than theoretical one. The HEBM conditions and carbon content in the composite were also observed to effect the reversible capacity value and first cycle Coulombic efficiency.

Electrolytes are also known to influence the electrochemical performances of batteries. Recently, various studies using ILs have reported enhanced electrochemical performances over wide temperature ranges, and especially at intermediate temperatures [5-7]. In particular, negative electrodes with high volume changes showed clear improvements in performance when ILs were employed due to the formation of a robust and stable SEI layer (see section 1.4.1 in Chapter 1) [8, 9]. In addition, there are a number of conversion and hybrid (conversion + alloying) based materials (i.e., Sn_4P_3 [10], Sb_2S_3/graphene [11]) for which the use of ILs has improved the electrochemical performances.

In this chapter, the investigation of CuP_2/C (80:20) using the Na[FSA]–[C_3C_1pyrr][FSA] (20:80) IL electrolyte is described. The obtained CuP_2/C composite materials are subsequently characterized by XRD, SEM and laser diffraction particle analysis. Furthermore, their charge-discharge behaviors are investigated by electrochemical tests, *ex-situ* and *in-situ* XRD and *ex-situ* TEM.

3.2 Experimental

Copper phosphide, CuP_2, was prepared by high-energy ball milling of copper metal (Kojundo Chemical Lab, purity 99.9%) and phosphorus powder (Wako Pure Chemical Industries, purity 98%) in a stoichiometric ratio under Ar atmosphere with a ball to powder ratio of 20:1 at 400 RPM for 30 h. The resulting powder was ball-milled again with AB (Wako Pure Chemical Industries) with a weight ratio of 80:20 at 900 RPM for 3 h to obtain the CuP_2/C composite. The XRD patterns of the samples were obtained with a Rigaku SmartLab diffractometer (CuKα (0.1541 nm), 40 kV−30 mA). Particle size, morphology, crystallinity, and elemental composition were analyzed by SEM, (Hitachi SU-8020), scanning transmission electron microscopy (STEM, JEOL JEM-2100F), and laser diffraction particle size analysis (Microtrac MT3300 II).

The negative electrode was prepared by mixing the active material (CuP_2/C), AB, and a PAI binder in a 75:15:10 weight ratio in NMP. The Na[FSA]-[C_3C_1pyrr][FSA] IL was prepared by mixing the two pre-dried salts in a 20:80 molar ratio and further vacuum-dried at 90 °C for more than 10 h. An organic electrolyte 1M $NaPF_6$ EC-PC (ethylene carbonate-propylene carbonate) (1:1 v/v) was used for comparison of electrochemical performance with IL electrolyte. A glass fiber filter (Whatman, GF-A, 260 mm in thickness and 16 mm in diameter) was used as a separator and a sodium metal disc (Aldrich, purity 99.9%) was used as a counter electrode. Electrochemical performance was measured by assembling a 2032 coin cell under Ar atmosphere. For *ex-situ* XRD measurements, the electrodes were taken out of the coin cells at different states of charge, rinsed with tetrahydrofuran (THF), and vacuum-dried for one day at room temperature. Similar procedures were employed for the preparation of TEM samples.

The *in-situ* XRD measurement was carried out using a special apparatus consisting of an air-tight cell with a Kapton® window and a temperature controller (Rigaku). For the preparation of negative electrode, the slurry was coated on an Al mesh rather than Al foil and dried using the same procedure as above. In addition, the electrode was impregnated with IL and the excess electrolyte was wiped with Kim wipe prior to assembly of special coin cell with an open SUS cap. The electrochemical measurement was done using an ECAD1000 charge-discharge system (EC Frontier Inc.). The charge-discharge current density was maintained at

50 mA g^{-1} in the voltage range of 0.005–2.0 V for 2 cycles at 90 °C under vacuum conditions. The setting was changed from constant current to constant voltage for 1 h at the end of each charge and discharge to confirm the structures obtained at these conditions. The scan rate of XRD was maintained at 1° min^{-1}.

3.3 Results and discussion

Figure 3-1 shows the XRD patterns of AB, CuP_2, and CuP_2/C. All of the peaks for CuP_2 and CuP_2/C are assigned to the monoclinic CuP_2 (space group $P2_1/c$), which confirms the formation of CuP_2 as reported previously [12]. The peak broadening observed for CuP_2 indicates low crystallinity, which is attributed to large lattice deformations caused by mechanical forces during ball-milling (400 rpm). Crystallinity is recovered after the second ball-milling step, which may be due to the generated heat, as a result of intense ball-milling (900 rpm) that promotes crystal growth.

Comparison of the SEM images (Figure 3-2 (a) and (b)) between CuP_2 and CuP_2/C indicates that the average particle size of the CuP_2/C composite is larger than that of CuP_2. To confirm the observation from SEM, particle size distribution was measured for both the samples using the laser diffraction analysis in water (Figure 3-2 (c-e) and (f-h) for CuP_2 and CuP_2/C, respectively). Extent of agglomeration was evaluated by sonication for 60 and 120 seconds. As evident from Figure 3-2 (c-e), the distribution of CuP_2 became broader and the median diameter (D_{50}) decreased with sonication (D_{50}: 6.49 µm without sonication, 2.53 µm for 60-second sonication, and 1.85 µm for 120-second sonication), which implies that the pristine CuP_2 consists of agglomerates and deagglomerates upon sonication. On the other hand, in the case of CuP_2/C composite, the broad peak near 8 µm remains unperturbed and another small peak below 1 µm becomes stronger with sonication (D_{50}: 4.52 µm without sonication, 4.11 µm for 60-second sonication, and 3.96 µm for 120-second sonication). This observation signifies that agglomerates of CuP_2/C are strongly bound owing to high pressure and impact during intense ball milling and are therefore difficult to separate. Hence the findings from the particle size distribution measurements support the results from SEM.

Figure 3-3 shows the electrochemical performance of the CuP_2/C composite. Figure 3-3 (a) and (b) represent the galvanostatic charge-discharge curves for 5 cycles at 25 and 90 °C, respectively, at 100 mA g^{-1}. Initial charge and discharge capacities of 429 and 316 mA h g^{-1} were observed with an initial coulombic efficiency of 73.7% at 25 K. From the third cycle on, the coulombic efficiency exceeded more than 99%. The capacity increased as the cycle proceeded, which may be due to the penetration of electrolyte resulting in extended access to the active material. The initial discharge capacity improved to 595 mA h g^{-1} with a slightly lower coulombic efficiency of 70.2% (initial charge capacity: 847 mA h g^{-1}) at 90 °C. Charge-discharge tests for the same CuP_2/C composite in an organic electrolyte (1 mol dm^{-3} $NaPF_6$ in ethylenecarbonate/propylenecarbonate (1:1 in vol.) revealed that performance of the CuP_2/C composite electrode is enhanced in ILs even at 25 °C and intermediate-temperature operation further clarify this trend (Figure 3-4). Increased electrolyte decomposition usually occurs at elevated temperatures during initial electrochemical reduction, and a large charge capacity is required to form a stable solid-electrolyte interphase (SEI) layer (below 1.5 V during the initial charging). The coulombic efficiency of the CuP_2/C electrode is higher than that of a TiO_2/C electrode [13], probably due to the former's well-grown particles with less surface area. The 5th cycle still produces a reversible capacity of 564 mA h g^{-1} with 99.6% coulombic efficiency. Results of the rate capability test of the CuP_2/C electrode at 25 °C and 90 °C are shown in Figure 3-3 (c). A significant drop in capacity was observed at 25 °C at high rates (373, 256, and 50 mA h g^{-1} at 100, 1000, and 8000 mA g^{-1}, respectively). On the other hand, high capacities were maintained at 90 °C at all current densities (567, 505, and 368 mA h g^{-1} at 100, 1000, and 8000 mA g^{-1}, respectively), and the capacity recovered to 94% after reverting back to a 100 mA g^{-1}

rate. This performance is derived from the enhancement of ionic conductivity and electrode reactions at elevated temperatures. Figure 3-3 (d) shows the cyclability test of the CuP_2/C composite at a high current density of 500 mA g^{-1} for 200 cycles (100 mA g^{-1} for the initial three cycles). Even at such a high current density the composite electrode gave a reversible capacity of 379 mA h g^{-1} after 200 cycles with 99.5% coulombic efficiency and retained 71.0% of its initial capacity. Moreover, decent capacity retention of 52.5% was also observed after 300 cycles at higher rate of 1000 mA g^{-1} (Figure 3-5). Although strong P-C or P-O-C bonds was proposed as the main reason for the high stability observed in phosphorus-carbon-based materials [1, 4], further investigation is needed to prove this mechanism.

Figure 3-6 shows the *ex-situ* XRD patterns of the CuP_2/C composite at different states of charge. Fading of the characteristic peaks assigned to CuP_2 and appearance of new peaks are observed in the charging process. The peak at 36.04° in the pattern at 0.005 V corresponds to the strongest peak of Na_3P, whereas the other small peaks around 36° are unidentified. During discharge, Na_3P disappears, and the electrode material becomes totally amorphous at 0.875 and 2.000 V. This observation is in contrast to previous reports which confirmed the presence of CuP_2 after discharging [1, 4]. Since *ex-situ* XRD data at 25 °C from the same IL electrolyte also contains CuP_2 after charging, this difference results from the operation temperature. Another possibility is the effect of the depth of charging since the larger capacity is obtained at 90 °C. Figure 3-7 shows the selected area electron diffraction (SAED), annular dark field STEM, and energy-dispersive X-ray spectroscopy (EDS) mapping images of the CuP_2/C composite after the initial cycle up to 2 V. No diffraction rings are observed in the SAED image suggesting that the material is amorphous even on the nano-scale. The EDS analysis shows the presence of Na, O, and S atoms in nearly the same region suggesting the formation of a Na^+ containing SEI layer on the particle.

The F atoms do not seem to be a main component in the SEI layer. The C atoms exhibit a slightly more diffuse mapping because of the presence of AB. The P/Cu ratio of 1.7 is close to 2, and the mappings of Cu and P atoms completely overlap with each other, suggesting that the composition of CuP_2 is preserved after the full discharge. This suggests that particle integrity is maintained after the initial cycle even though the long-range structural order is lost. For more investigation of charge-discharge mechanism, in-situ XRD measurements were performed at 90 °C with charging and discharging rates of 50 mA g^{-1} (0.05 C) (see Figure 3-8 for *in-situ* XRD patterns). The peak intensity corresponding to CuP_2 becomes smaller after first charging which states the conversion process of CuP_2. No other peak was observed after full charging which indicates that the product is amorphous. However, after first discharge, peaks corresponding to Cu_3P appears unlike the previous case of *ex-situ* XRD. In the second cycle, the same process as first cycle was repeated which depicts the reversibility of the reaction. Presence of Cu_3P after full discharge was also observed for CuP_2/C in a Li secondary battery system [12]. The difference between the *ex-situ* and *in-situ* XRD may arise from the difference in rate or depth of charge, but Cu_3P is one of the possible product at the discharged state of this material.

3.4 Conclusions

In summary, electrochemical performance of the CuP_2/C composite was investigated using the Na[FSA]-[C_3C_1pyrr][FSA] IL electrolyte in view of intermediate-temperature operation of Na secondary batteries for medium to large-scale applications. It exhibited reversible capacities of 373 mA h g^{-1} and 564 mA h g^{-1} at 25 and 90 °C, respectively, at a rate of 100 mA g^{-1}. Additionally, this composite showed a wide range of rate capability at 90 °C by retaining 65% of its capacity at a high rate of 8000 mA g^{-1} compared to its capacity at 100 mA g^{-1}. Even at the elevated rate of 500 mA g^{-1}, it showed excellent cycle stability maintaining

71.0% of its capacity after 200 cycles. *Ex-situ* XRD and STEM revealed the presence of Na_3P after full charging and reformation of amorphous CuP_2 after full discharging. Further optimization on the CuP_2/C ratio and discussion on the reaction mechanism has been discussed in Chapter 4.

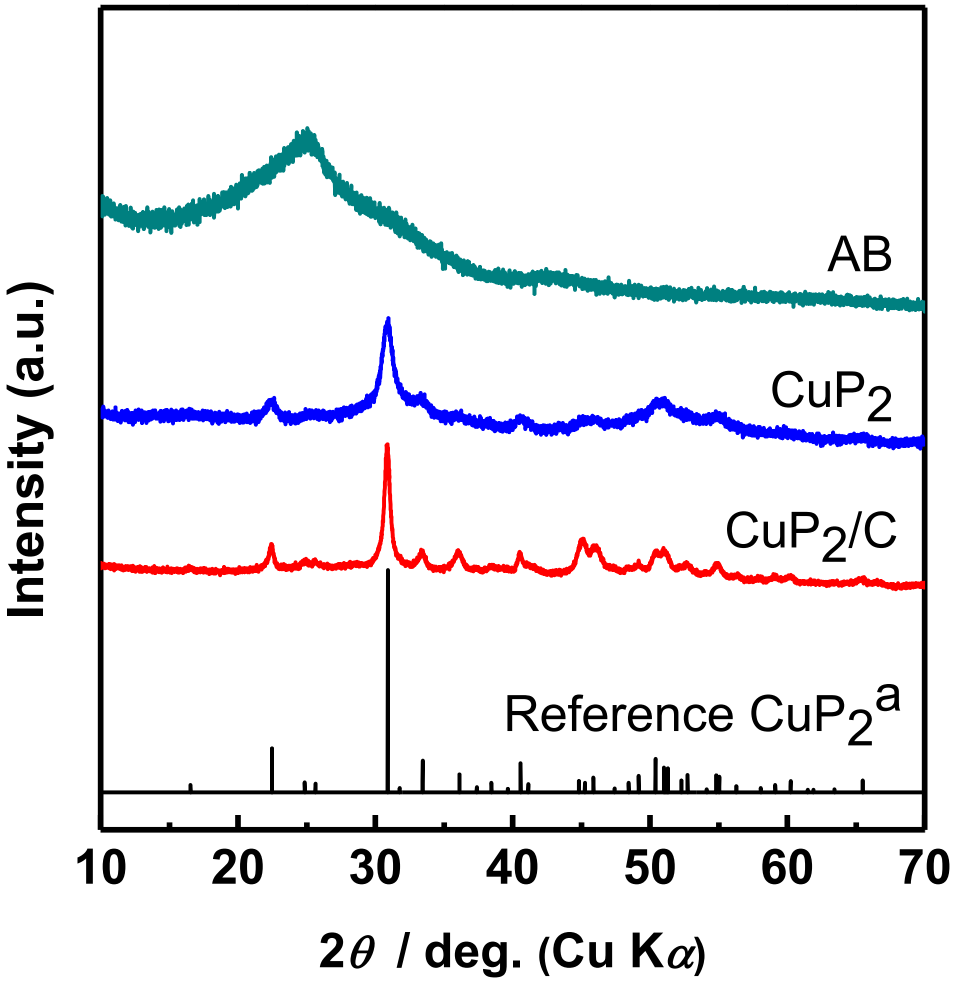

Figure 3-1 (a) XRD pattern of AB, CuP_2, and CuP_2/C, respectively. SEM images of (b) CuP_2 powder and (c) CuP_2/C powder. [a]Ref[4]

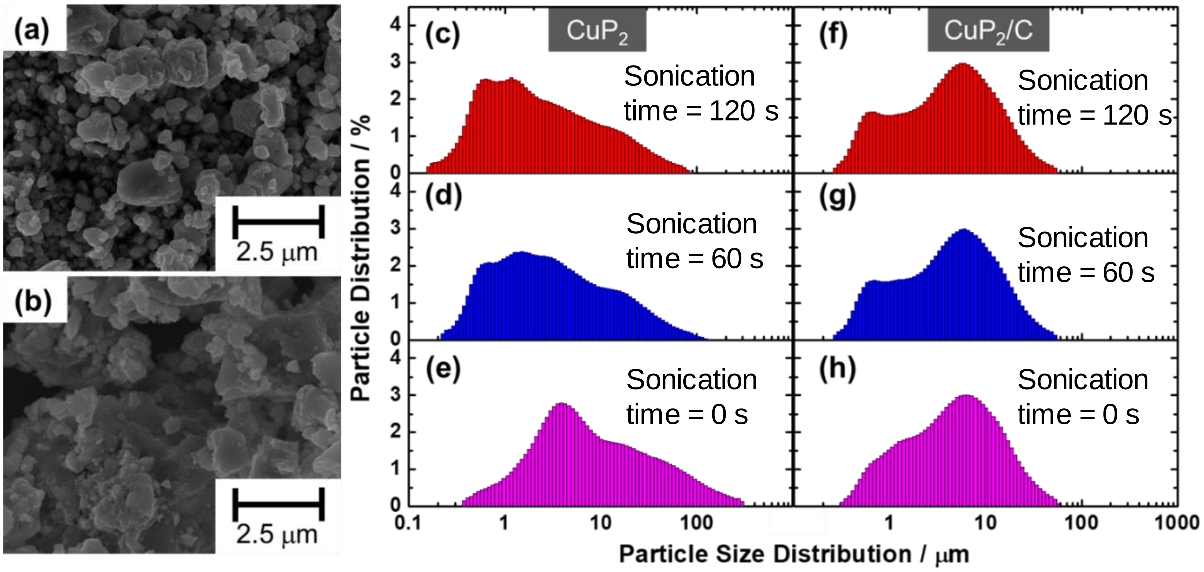

Figure 3-2 SEM images of (a) CuP_2 powder and (b) CuP_2/C powder. Particle size distribution of CuP_2 (c-e) and CuP_2/C (f-h) for sonication time of 120, 60, and 0 s, respectively.

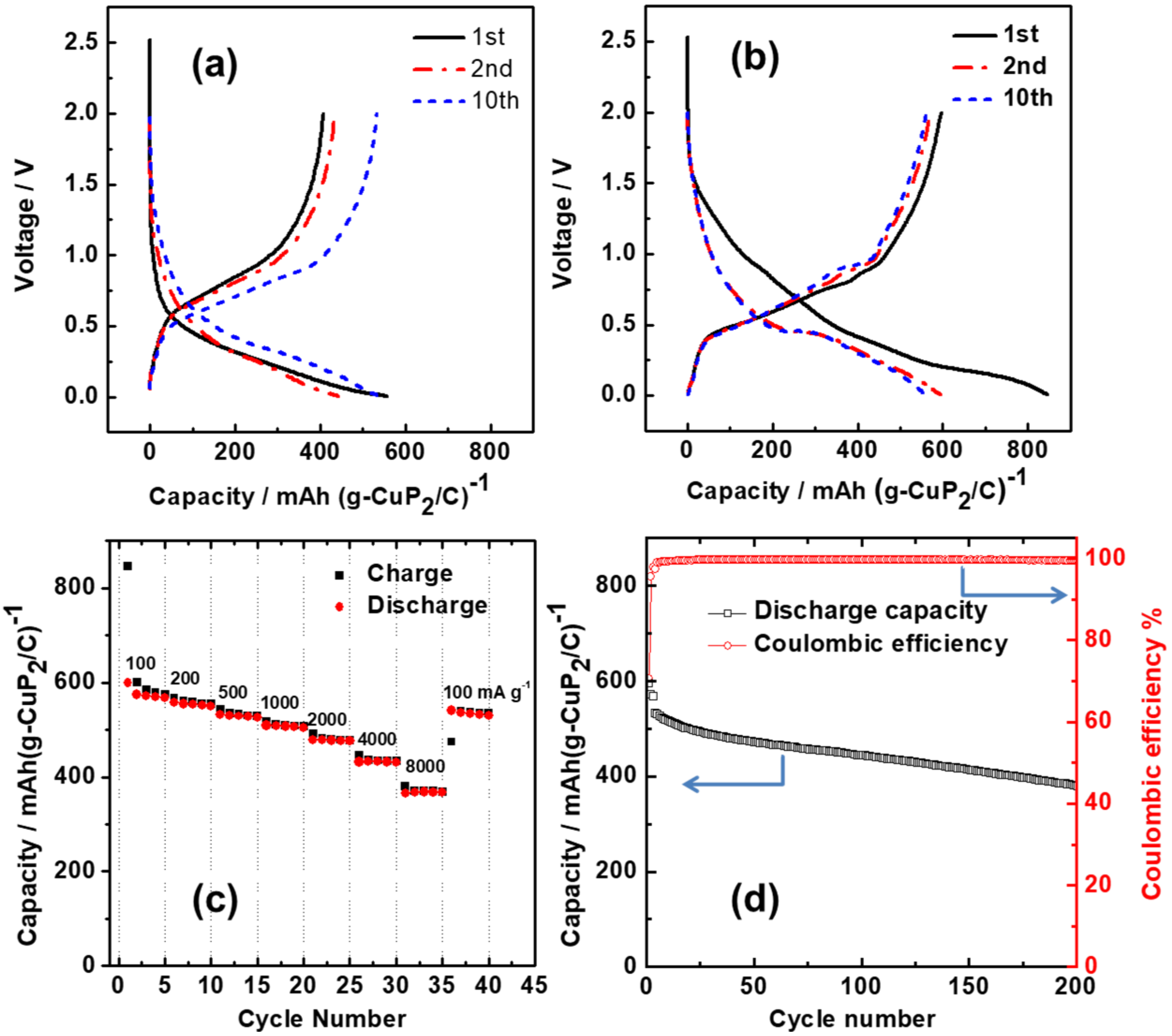

Figure 3-3 Galvanostatic charge-discharge curves of the CuP_2/C composite at (a) 25 °C, (b) 90 °C (rate: 100 mA g^{-1}, voltage range: 0.005–2.000 V), (c) rate capability test at 25 °C and 90 °C (rate: 100 mA g^{-1} – 8000 mA g^{-1}), and (d) cyclability test at 90 °C (rate: 500 mA g^{-1} (first three cycles at 100 mA g^{-1})).

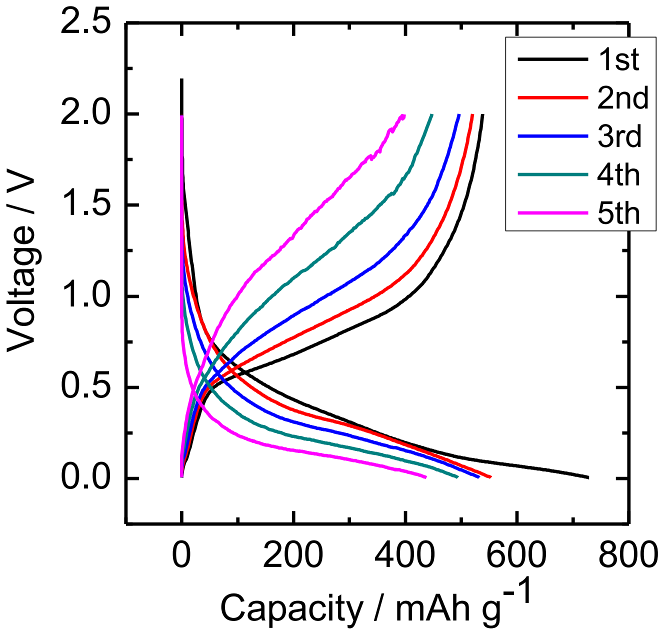

Figure 3-4 Galvanostatic charge-discharge curve of the CuP_2/C composite with 1 mol dm^{-3} $NaPF_6$ in ethylene carbonate (EC)-propylene carbonate (PC) (1:1 v/v) at 25 °C (rate: 100 mA g^{-1}, voltage range: 0.005–2.000 V).

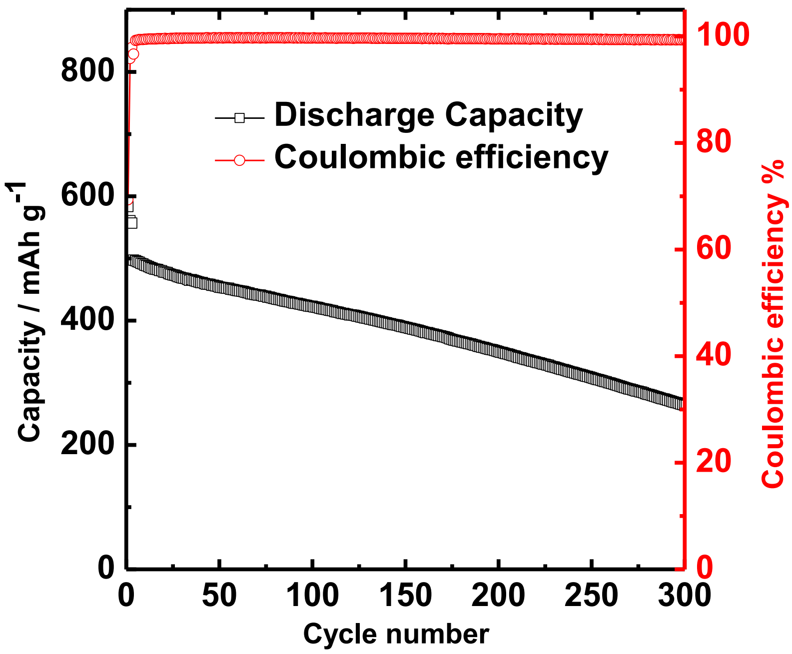

Figure 3-5 Cyclability test at 90 °C (rate: 1000 mA g^{-1} (first three cycles at 100 mA g^{-1}), voltage range: 0.005–2.000 V).

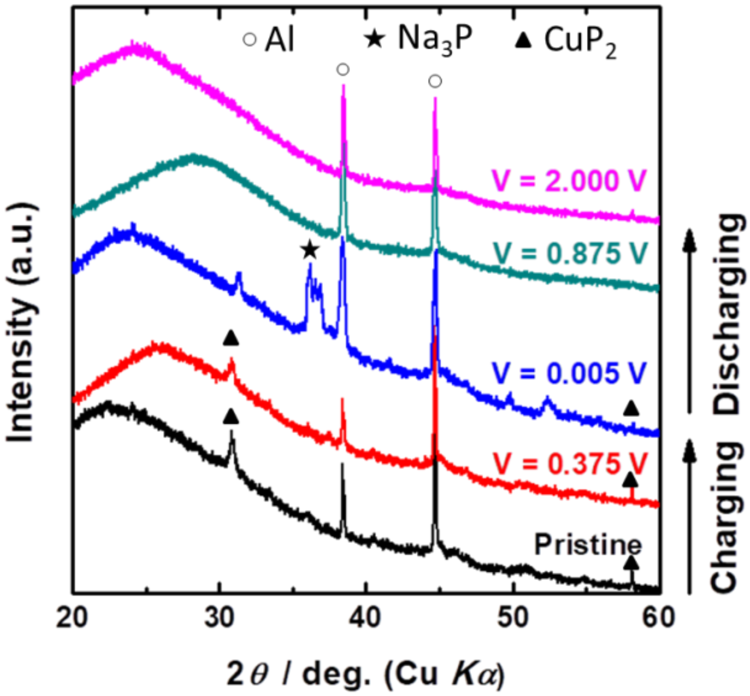

Figure 3-6 *Ex-situ* XRD of the first cycle at different states of charge (pristine, 0.375 V, 0.005 V, 0.875 V, and 2.000 V).

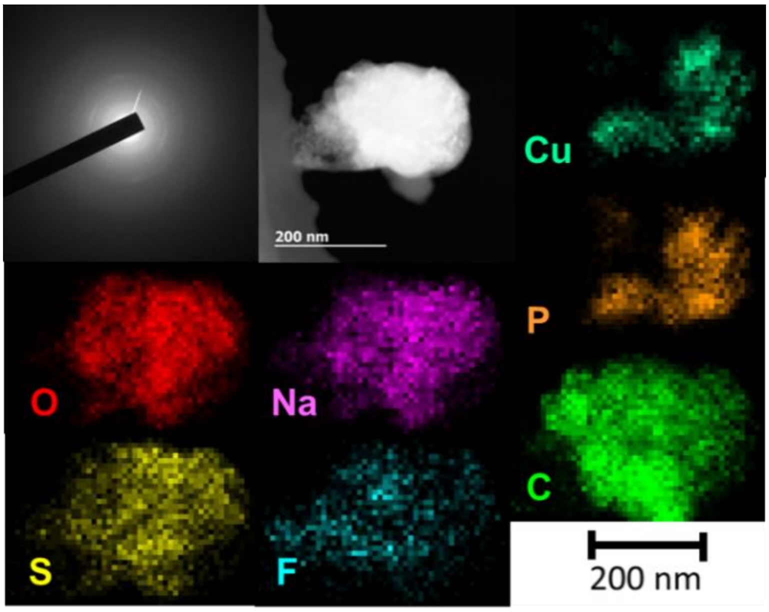

Figure 3-7 *Ex-situ* SAED, annular dark field STEM, and EDS mapping images for the fully discharged CuP_2/C composite (2.000 V) after the initial charge-discharge cycle.

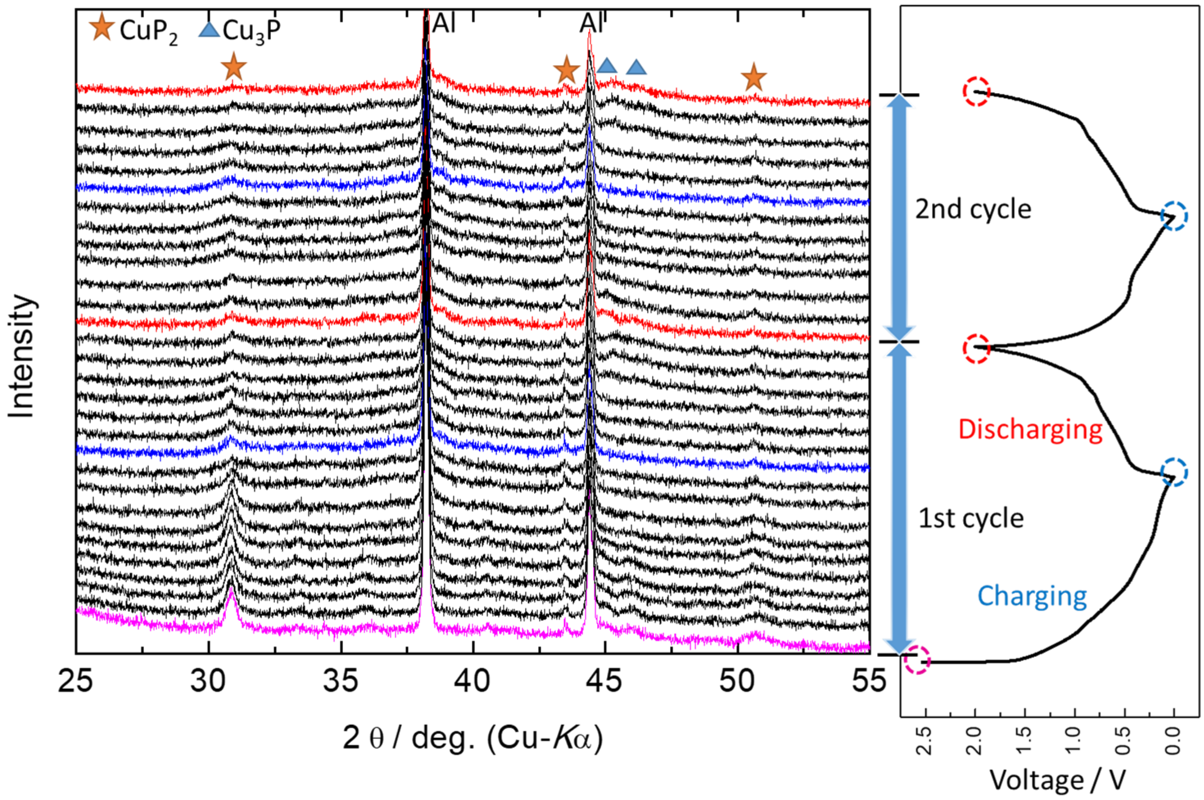

Figure 3-8 *In-situ* XRD for the first and second cycle at 90 °C. Charge-discharge rate: 50 mA g^{-1} (0.05 C). Copper metal impurity appears from the incomplete ball-milling process.

References

[1] F. Zhao, N. Han, W. Huang, J. Li, H. Ye, F. Chen, Y. Li, J. Mater. Chem. A, 3 (2015) 21754-21759.

[2] S. Chen, F. Wu, L. Shen, Y. Huang, S.K. Sinha, V. Srot, P.A. van Aken, J. Maier, Y. Yu, ACS Nano, 12 (2018) 7018-7027.

[3] Y. Zhang, G. Wang, L. Wang, L. Tang, M. Zhu, C. Wu, S.-X. Dou, M. Wu, Nano Lett., 19 (2019) 2575-2582.

[4] S.-O. Kim, A. Manthiram, Chem. Commun., 52 (2016) 4337-4340.

[5] M. Forsyth, H. Yoon, F. Chen, H. Zhu, D.R. MacFarlane, M. Armand, P.C. Howlett, J. Phys. Chem. C, 120 (2016) 4276-4286.

[6] J. Hwang, K. Matsumoto, R. Hagiwara, Adv. Sustainable Syst., 2 (2018) 1700171.

[7] R. Hagiwara, K. Matsumoto, J. Hwang, T. Nohira, Chem. Rec., 19 (2019) 758-770.

[8] H.-C. Chen, J. Patra, S.-W. Lee, C.-J. Tseng, T.-Y. Wu, M.-H. Lin, J.-K. Chang, J. Mater. Chem. A, 5 (2017) 13776-13784.

[9] B.E. Gurkan, Z. Qiang, Y.-M. Chen, Y. Zhu, B.D. Vogt, J. Electrochem. Soc., 164 (2017) H5093-H5099.

[10] H. Usui, Y. Domi, K. Fujiwara, M. Shimizu, T. Yamamoto, T. Nohira, R. Hagiwara, H. Sakaguchi, ACS Energy Lett., 2 (2017) 1139-1143.

[11] C.-Y. Li, J. Patra, C.-H. Yang, C.-M. Tseng, S.B. Majumder, Q.-F. Dong, J.-K. Chang, ACS Sustain. Chem. Eng., 5 (2017) 8269-8276.

[12] S.-O. Kim, A. Manthiram, ACS Appl. Mater. Interfaces, 9 (2017) 16221-16227.

[13] C. Ding, T. Nohira, R. Hagiwara, J. Mater. Chem. A, 3 (2015) 20767-20771.

Chapter 4

Optimization of the Carbon Content in Copper Phosphide-carbon Composite Negative Electrodes

4.1 Introduction

The carbon composites of alloying and conversion based materials have shown improved cycleability and rate capability than the pure materials for NIBs [1-3]. For instance, a FeP/graphite composite prepared by low energy ball-milling (300 rpm) showed more than twice the capacity retention than FeP after 70 cycles [4]. In another report, cobalt phosphide carbon nanosheets prepared by one-step calcination process delivered a high Na-ion storage capacity of ~600 mA h g^{-1} at 100 mA g^{-1} and capacity retention of 98.5% after 900 cycles at 1000 mA g^{-1} [5]. The presence of P-C bond, confirmed by XPS, was suggested to provide robust contact between CoP and carbon improving the electrode kinetics and buffer against the large volume change. Hollow microspheres Sn_4P_3 coated with N-doped carbon showed a significant improvement in cycleability and rate capability than only Sn_4P_3 owing to the better electrode kinetics [6].

The content of the carbon in the composite also influence the electrochemical performance in NIBs. The insufficient amount of carbon fails to provide enough buffer and electronic contact between active material which leads to electrode mechanical failure and sluggish kinetics. On the other hand, large amount of carbon leads to lower tap density as well as high surface area resulting in lower volumetric capacities and elevated electrolyte decomposition leading to thicker SEI layers [7], respectively. A carbon coated anatase TiO_2 prepared by hydrothermal method in various carbon contents (0, 3.5, 6.8, 10.3 and 12.6 wt%)

was analyzed as negative electrode for NIBs and this study showed that TiO_2/C (6.8 wt%) delivered the optimum performance [8].

The interaction between the active material and carbon can be improved by chemical bonding which can boost the electrochemical performance. For example, P chemically bonded on the carboxyl-groups-functionalized carbon nanotubes (CNTs) provided a high capacity of 2134 mA h g^{-1} and ~92% capacity retention after 100 cycles [9]. The presence of P-O-C bond was proposed to maintain the electrical contact of P to carbon during the cycling. In recent studies regarding phosphide based materials (CuP_2/C [10], GeP_3/C [11], NiP_3/CNT [12]) P-O-C bond have been reported as the key component for enabling high performance in these materials [13].

Electrolytes strongly influence the electrochemical performance of negative electrode, especially for those based on high volume change during charging and discharging (P/AB [14], Sn [15]) by forming stable SEI layer. Moreover, suppression of large volume change has also been observed in Si negative electrode in LIBs using IL [16]. An antimony sulfide Sb_2S_3, was investigated using 1 mol dm^{-3} Na[FSA]-[C_3C_1pyrr][FSA] IL and various organic electrolytes at 25 and 60 °C [17]. High first cycle discharge capacities of 710 and 660 mA h g^{-1} were delivered with 1 mol dm^{-3} Na[ClO_4]-PC/FEC and 1 mol dm^{-3} Na[FSA]-[C_3C_1pyrr][FSA] at 25 °C, respectively. At 60 °C, better cycleability and rate capability was observed in the IL case. In the previous chapter, CuP_2/C (80:20) also demonstrated high performance with IL electrolyte. However, the underlying mechanism was not well-understood.

In this chapter, investigation of copper phosphide containing various contents of AB ranging from 10 to 40 wt% using the Na[FSA]–[C_3C_1pyrr][FSA] (20:80) IL electrolyte is described. The obtained CuP_2/C composite materials are subsequently characterized by XRD, TEM, and XPS to obtain the optimized CuF_2/C ratio. Furthermore, their charge-discharge behaviors are investigated by electrochemical tests, including EIS and the GITT.

4.2 Experimental

All air-sensitive materials were handled in a glove box. The copper powder (Kojundo Chemical Lab, purity 99.9%) and phosphorus powder (Wako Pure Chemical Industries, purity 98%) were ball-milled (Planetary Micro Mill Pulverisette 7, Fritsch, 20 mL grinding bowl and 3 mm zirconium oxide balls) for 30 h at 400 rpm under an Ar atmosphere in a 1:2 molar ratio to obtain CuP_2. The as-prepared CuP_2 was further ball-milled with AB (Wako Pure Chemical Industries) for 3 h at 900 rpm. The copper phosphide carbon composites containing various AB weight percentages are represented as CuP_x-Cy ($x = 2$ for $y = 10$, 20, and $x = 1/3$ for $y = 30$, 40), where x represents the stoichiometry of phosphorus in CuP_x ($x = 2$ or 1/3) and y denotes the weight percentage of AB in the composite, respectively. A control sample was prepared in which CuP_2 was ball-milled with AB in a 70:30 w/w ratio at 500 rpm for 3 h. The XRD patterns of the resulting samples were obtained using a Rigaku SmartLab diffractometer (40 kV and 30 mA). The particle size, morphology, and elemental composition were analyzed by SEM (Hitachi SU-8020) and EDX (Horiba EMAXEvolution X-max). XPS was carried out with using a JEOL XPS instrument (JPS-9010, MgKα, 10 kV−10 mA). The binding energy was corrected using the binding energy of indium foil (The Nilaco Corporation) as a reference (443.8 eV). The obtained spectra were fitted using the SpecSurf software (SpecSurf, ver. 1.8.3.7, JEOL, Ltd.). Argon ion etching was performed at an ion energy of 400 eV for 60 s with an interval of 20 s for the CuP_x-C30 sample and for 15 s with an interval of 5 s for the CuP_x-C20 sample.

The negative electrode was prepared by mixing the active material (CuP_x-Cy), AB as a conductive additive, and PAI binder in a 75:15:10 weight ratio in NMP (Wako Pure Chemical Industries, purity 99%). The resulting slurry was subsequently cast on Al foil and dried under vacuum at 90 °C for 10 h in an oven and in an airtight cell connected to a vacuum line at 110 °C overnight. The mass loading of the active material in the electrode was approximately 1.5 mg

cm^{-2}. Coin cells (2032-type) were assembled in a glove box to measure the electrochemical performance of each material.

Electrochemical impedance spectra were recorded using a VSP potentiostat (Bio-Logic) at 90 °C over a frequency range of 100 kHz to 10 mHz with an amplitude of 20 mV. In the GITT measurements, charge-discharge was carried out at 100 mA g^{-1} for 1 h followed by resting for 8 h at 90 °C. The GITT measurement was performed at the 3rd, 50th, and 100th cycles, and other cycles were charge-discharged at the same conditions as the cycle test.

The sample preparation method for TEM was similar to that employed for *ex-situ* XRD, but the powder was scratched from the Al foil after drying. The collected CuP_x-C*y* sample was then dispersed onto a molybdenum TEM grid coated with a porous amorphous carbon film. TEM observations, selected area electron diffractions, and EDX combined with scanning TEM (STEM) were performed using a JEOL JEM-2100F microscope, operated at 60 kV.

4.3 Results and discussion

The CuP_x-C*y* electrode materials were prepared by a two-step ball-milling process; the first step involved the reaction of stoichiometric quantities of Cu and P at 400 rpm to give CuP_2, while the second step involved CuP_2 and AB in a target ratio at 900 rpm to give the desired composite material. The description CuP_x is used herein since transformation from CuP_2 to Cu_3P (CuP_x where x =1/3) was observed in some cases as shown below. The weight percentage of carbon in the composite is represented as *y* in the formula CuP_x-C*y*. Figure 4-1 shows the XRD patterns of (a) CuP_2, (b) CuP_x-C10, (c) CuP_x-C20, (d) CuP_x-C25, (e) CuP_x-C30, and (f) CuP_x-C40. After ball-milling, the carbon contents of CuP_x-C20 and CuP_x-C30 were confirmed to be 19.1 and 28.8 wt% by combustion analysis which were close to the theoretical values. Overall, the main diffraction pattern changes from CuP_2 to Cu_3P with increasing carbon content. More specifically, the broad peaks observed in Figure 4-1(a) are indexable to CuP_2 [18] (space group: *P*21/c), indicating the formation of pure CuP_2 by ball-milling. Peak broadening was observed after ball-milling over 30 h [19]. In addition, the crystallinity of CuP_2 was improved in CuP_x-C10 and CuP_x-C20 after ball-milling, with the appearance of small Cu_3P peaks at 45.12 and 46.20° being observed, as shown in Figures 4-1(b) and 4-1(c). This phenomenon can be explained by the heat evolution during the high speed ball-milling process. The conversion of CuP_2 to Cu_3P may also have been induced by the presence of AB; however, the appearance of Cu_3P peaks was enhanced in the case of CuP_x-C25 (Figure 4-1(d)) with the concurrent weakening of the CuP_2 peaks, and their complete disappearance in the spectra of CuP_x-C30 and CuP_x-C40 (Figures 4-1(e) and 4-1(f)). The conversion of CuP_2 to Cu_3P at higher carbon contents can be partially explained by the thermal reaction induced by the increased carbon content during the high-energy ball-milling process. Ball-milling is reported to facilitate reduction at lower temperatures compared to un-milled conditions owing to the increased interfacial area and lower activation barrier for the reaction [20]. According to some reports, the temperature inside the ball-milling vial can rise up to several hundred degrees Celsius, depending on many factors, and in particular the ball diameter and rotation speed [21, 22]. The XRD pattern of the CuP_2 ball-milled at a lower speed of 500 rpm containing AB in a 70:30 weight ratio was similar to that of CuP_x-C20 (see Figure 4-2), thereby indicating that the speed of the ball-milling operation is a key factor in determining the oxidation state of copper phosphide in the product, where carbon acts as a catalyst for the extraction of phosphorus from the metal phosphide to provide a separated amorphous phosphorus phase.

Figure 4-3 shows the TEM images and related observations for the CuP_x-C20 and CuP_x-C30 particles. More specifically, the spots in the fast Fourier transform (FFT) power spectrum of CuP_x-C20 (Figure 4-3(c)) obtained from the high resolution (HR)TEM image (Figure 4-3(b)) are clearly indexed to the *d*-spacing of CuP_2. In contrast, the selected area electron diffraction of CuP_x-C30 shown in Figure 4-3(e) shows a single weak diffraction spot with a *d*-spacing of

0.194 nm, which was assigned to the 113 diffraction line of Cu_3P. Moreover, energy-dispersive X-ray spectroscopy (EDX) combined with scanning TEM (STEM) showed an even distribution of the constituent elements (C, O, P, and Cu) in the particles (Figure 4-3(f)), and so these results support the XRD data presented in Figure 4-1.

To understand the bonding states of the constituent elements, XPS depth profiling of the pristine CuP_x-C20 and CuP_x-C30 samples was carried out by Ar etching. Thus, Figure 4-4 shows the Cu2p, P2p, O1s, and C1s XPS spectra of CuP_x-C20 (a–d) and CuP_x-C30 (e–h). In the case of CuP_x-C20, the outer oxide layer is thinner than that of CuP_x-C30, as is evident from the absence of an oxide peak in the Cu2p spectrum (Figure 4-4(a)) and a reduction in the intensity of the P-O-C peak at a binding energy of approximately 133 eV after 5 s of etching, as depicted in Figure 4-4(b). Furthermore, no significant changes were observed in the O1s and C1s spectra following etching (Figures 4-4(c) and 4-4(d)). In the Cu2p spectrum of CuP_x-C30 (Figure 4-4(e)), a broad peak at 934.7 eV and a shoulder peak at 932.8 eV were assigned to CuO and CuP_x, respectively [23, 24]. After Ar etching for 20 s, only the peak corresponding to CuP_x remained, and this exhibited a greater intensity to that observed in the pristine material. No change was observed in the spectra after etching for 40 and 60 s. In the P2p spectrum (Figure 4-4(f)), two fairly distinct peaks assigned to the formation of P-O bonds and CuP_x were observed at 134 and 130 eV, respectively. Similar to the Cu2p spectrum, the P-O peak disappeared after etching for only 20 s. In addition, the O1s spectrum exhibited a slight shift towards lower energies after etching for 20 s, accompanied by significant weakening of the peak, as shown in Figure 4-4(g), thereby indicating the presence of P-O-C bonds at the surface of CuP_x-C30. In the C1s spectrum (Figure 4-4(h)), oxidation of the carbon present in the pristine sample (~286 eV) was detected, and the oxidized layer was found to be stripped after 20 s of etching, again suggesting the formation of surface P-O-C bonds. These results therefore conform that CuP_x-C30 contains a relatively thick oxide layer.

Figure 4-5 presents the electrochemical performances of CuP_2 and of the various CuP_2/C composites (i.e., CuP_x-C10, CuP_x-C20, CuP_x-C30, and CuP_x-C40) in the IL electrolyte. More specifically, Figure 4-5(a) shows the galvanostatic charge-discharge curves for the first cycle at 90 °C, where the capacity is calculated based on the weight of the CuP_2 and CuP_x/C. A current rate of 100 mA g^{-1} was applied, in addition to a high charge capacity of 1293 mA h $g^{-1}$and a low discharge capacity of 454 mA h g^{-1}, thereby resulting in a large irreversible capacity of 839 mA h g^{-1} for the pure CuP_2, owing to the low electrical conductivity and large volume change after sodiation. However, the introduction of only 10 wt% carbon into the composite significantly improved the discharge capacity to 789 mA h g^{-1}, while the discharge capacities for CuP_x-C20, CuP_x-C30 and CuP_x-C40 decreased in the order of 595, 504, and 463 mA h g^{-1}, respectively. As shown in Figure 4-5(b), the capacity is calculated based on the weight of CuP_2 without including carbon. The capacity contribution of ball-milled AB was estimated to be 72 mA h g^{-1} based on the discharge of a ball-milled AB electrode, as shown in Figure 4-6. Thus, it was clearly observed that the discharge capacities of CuP_x-C20, CuP_x-C30, and CuP_x-C40 exhibit similar capacities of 745, 720, and 790 mA h g^{-1}, respectively, whereas CuP_x-C10 (90:10) gave a remarkably larger discharge capacity of 876 mA h g^{-1}. In addition, Figure 4-5(c) shows the cycle performance of the CuP_x/C composites at 90 °C and at the rate of 500 mA g^{-1} (100 mA g^{-1} for the first three cycles for activation). Over 150 cycles, CuP_x-C30 and CuP_x-C40 demonstrated excellent cycleabilities, retaining 100% of their capacities based on the 4th cycle, whereas severe capacity loss was observed for CuP_x-C10, in addition to 71% capacity retention for CuP_x-C20. Furthermore, Figure 4-5(d) shows the Coulombic efficiencies upon cycling for all composites. More specifically, CuP_x-C10 demonstrated the highest Coulombic efficiency of 78.2% for the first cycle, and reached 98.2% at the 20th cycle, although this value dropped significantly after 20 cycles. The first cycle Coulombic efficiency was also found to decrease upon increasing the carbon content (*i.e.*, 70.8, 70.6, and 62.7% for CuP_x-C20, CuP_x-C30, and

CuP_x-C40, respectively). However, it improved with cycling, and reached 99.63, 99.85, and 99.98%, respectively, at the 150th cycle. The inset shows the magnified Coulombic efficiency during cycling to demonstrate that the Coulombic efficiency of the composite improved upon increasing the carbon content, although it decreased slightly after 100 cycles in the case of CuP_x-C20. This result is further supported by the SEM images obtained for the CuP_x-C20 and CuP_x-C30 electrode samples after 50 cycles, as shown in Figure 4-7. More specifically, after 50 cycles, huge cracks are clearly observed for the CuP_x-C20 electrode (Figures 4-7(a) and 4-7(c)), whereas a comparatively smooth surface is observed for the CuP_x-C30 electrode with little volume expansion of the particles (Figures 4-7(b) and 4-7(d)). These results therefore indicate that CuP_x-C30 provides the optimal electrochemical performance in terms of the reversible capacity and cycleability. In the following discussion, the detailed electrochemical performance will be discussed for the case of CuP_x-C30.

To elucidate the influence of the ball-milling speed, the electrochemical performance of CuP_2 ball-milled with AB (70:30 w/w) prepared at a lower speed of 500 rpm (CuP_x-C30-500 rpm) was measured in the IL electrolyte at 90 °C (see Figure 4-2 for the XRD pattern of this material). Figure 4-8(a) shows the galvanostatic charge-discharge curves of CuP_x-C30-500rpm at 100 mA g^{-1} and at a cut-off voltage of 0.005–2.0 V. A slightly higher discharge capacity of 536 mA h g^{-1} than the value of 504 mA h g^{-1} obtained for CuP_x-C30 prepared at 900 rpm was observed in the first cycle. However, a lower Coulombic efficiency of 61% (*c.f.*, 70.6% for the sample prepared at 900 rpm) was observed due to the presence of the CuP_2 phase with a low electronic conductivity. However, the capacity retention decreased to 81% after only 50 cycles (Figure 4-8(b)), suggesting that ball-milling at 900 rpm facilitated P-O-C bond formation, and that the Cu_3P phase was required for a high cyclability.

The electrochemical performance of CuP_x-C30 in the IL electrolyte was also investigated at 25 °C for its possible application at approximately room temperature. Thus,

Figure 4-9 compares the electrochemical performances of CuP_x-C30 at 25 and 90 °C using the IL electrolyte. More specifically, Figure 4-9(a) shows the galvanostatic charge-discharge curves at 25 °C for 3 cycles at a rate of 100 mA g^{-1} and a 0.005–2 V cut-off voltage. A discharge capacity of 430 mA h g^{-1} with a Coulombic efficiency of 73.2% was observed in the first cycle, and the charge-discharge curves in the following cycles overlapped with each other, thereby indicating the excellent reversibility of the reaction. In addition, Figure 4-9(b) shows the rate capability of CuP_x-C30 at 25 and 90 °C. In this case, discharge capacities of 495, 456, and 358 mA h g^{-1} were obtained at rates of 100, 1000, and 8000 mA g^{-1} at 90 °C, while values of 421, 276, and 3 mA h g^{-1} were obtained at 25 °C (see the corresponding charge-discharge curves in Figure 4-10). These data obtained at the two temperatures clearly indicate the advantages of intermediate-temperature operations in terms of the rate capability of CuP_x-C30, and this was attributed to enhanced electrode kinetics and ion transport in the IL electrolyte. Furthermore, Figure 4-9(c) shows the cycleability of CuP_x-C30 at 25 and 90 °C at a rate of 500 mA g^{-1} (first three cycles = 100 mA g^{-1}) over 350 cycles. Discharge capacities of 394 and 458 mA h g^{-1} were obtained at 25 and 90 °C at the 350th cycle, representing capacity retentions of 111.2 and 98.9% based on the 4th cycle, respectively. *Ex-situ* XPS of CuP_x-C30 was carried out after charging and discharging at 0.005 and 2.0 V at 90 °C, respectively, and Figure 4-11 shows the P2p spectra of the pristine, charged, and discharged samples. As observed in the figure, the peak intensity at 130 eV (assigned to CuP_x) weakened after charging, but recovered after discharging, again indicating the reversibility of the reaction. In contrast, the peak intensity at higher binding energies for the pristine (assigned to the P-O bonds) remained unchanged in all cases, suggesting the inertness of this surface species and surface protection from pulverization, as observed in Figure 4-7.

Figure 4-12 shows the *ex-situ* XRD patterns of the CuP_x-C30 electrode during the initial two cycles. Peaks attributable to Cu_3P are observed in the pristine CuP_x-C30 sample as discussed above (Figure 4-1(e)). After sodiation in the first cycle, the peaks of Cu_3P disappeared and a peak ascribed to Na_3P at 36.26° appeared, concurrent with NaF peaks at 38.82 and 56.07°, since NaF is a common product of the SEI layer on the negative electrode. This indicates the conversion of Cu_3P along with sodiation and SEI layer formation, although the formation of Na_3P can also occur upon the reaction of any amorphous phosphorus that may be present. The SEI formation is also evident from the *ex-situ* TEM/EDX after charging and discharging in the first cycle (Figure 4-13). After desodiation, the peaks corresponding to Na_3P disappeared, weak peaks attributed to Cu_3P were observed once again, and the peaks arising from NaF also remained. This phenomenon was also observed in the second cycle, indicating the high reversibility of the reaction, as also suggested from the XPS data (Figure 4-11). In the second cycle, the second highest peak corresponding to Na_3P was apparent after sodiation, which resulted from the improved crystallization of Na_3P compared to the first cycle. A number of unknown peaks were also observed in the charged states (i.e., 30.58 and 37.73° at 0.005 V for the first cycle and 31.88, 32.40, 34.65, and 35.04° at 0.005 V for the second cycle), which are a matter for future investigation.

To understand the different cycleabilities of CuP_x-C20 and CuP_x-C30, EIS was carried out for the Na/CuP_x-Cy half-cell with cycling at 90 °C. Thus, Figure 4-14 shows the changes in interfacial resistance with cycling in the cases of CuP_x-C20 and CuP_x-C30. The cell was charged and discharged up to the target cycle and then charged to 0.5 V. In Figures 4-14(a) and 4-14(b), the spectra comprise of two semicircles at the higher and middle frequencies followed by a straight line at a lower frequency, which represents the interfacial and Warburg resistances, respectively. All spectra were fitted by the equivalent circuit in the inset of Figure 4-14(c), where the R_1 resistance represents the bulk resistance of the system. Table 4-1 summarizes the EIS fitting parameters for CuP_x-C20 and CuP_x-C30. The characteristic frequencies for the semicircles fall under the range of 3000–40000 Hz for the higher frequency region and 100–

500 Hz for the middle frequency region, indicating the film resistance domain (R_2) and charge transfer domain (R_3), respectively [25]. Although R_2 and R_3 decrease with cycling for CuP_x-C30 (6.25 (1st) and 1.68 (100th) ohm for R_2, and 8.84 (1st) and 3.01 (100th) ohm for R_3), the corresponding values for CuP_x-C20 exhibit complicated behavior, whereby R_2 decreases during the initial 10 cycles and increases subsequently (42.25 (1st), 1.44 (10th), and 10.17 (100th) ohm), and R_3 does not change significantly, staying relatively constant in the range of 1.79–6.17 ohm. This result indicates the importance in the R_2 value, whereby the SEI displayed an increase in stability upon increasing the carbon content in the composite from 20 to 30 wt%.

Figure 4-15 shows the galvanostatic intermittent titration technique (GITT) curves for CuP_x-C20 (a, b, c) and CuP_x-C30 (d, e, f) measured at 90 °C and at a rate of 100 mA g^{-1} for 1 h, followed by relaxation for 8 h at the 3rd cycle (a, d), 50th cycle (b, e), and 100th cycle (c, f). In the 3rd cycle, both CuP_x-C20 and CuP_x-C30 exhibit low overpotentials at all titration points, and their capacities are similar to those obtained from the continuous galvanostatic charge-discharge measurement (Figures 4-15(a) and 4-15(d)), which indicates high kinetics in both the cases. However, at the 50th cycle, a large polarization is observed at the beginning of the charging process for CuP_x-C20 compared to that of CuP_x-C30 (Figures 4-15(b) and 4-15(d)), and an increase in the overpotential is observed at the end of the discharge process. A more distinct difference is observed at the 100th cycle (Figures 4-15(c) and 4-15(f)), whereby the overpotential significantly increased for CuP_x-C20 at all states of charge. The high polarization indicates low kinetics because of the insufficient electronic conductivity derived from the low carbon content. In addition, the OCV hysteresis between the equilibrium voltage of the charge and discharge processes increased gradually over 100 cycles in the case of CuP_x-C20, thereby suggesting deviation from the original reaction pathway after 100 cycles, whereas the OCV hysteresis remained similar to the case of CuP_x-C30. This result demonstrates the improved kinetics over long-term cycling in the case of CuP_x-C30, which is in good agreement with the EIS results.

4.4 Conclusions

In this chapter, a range of copper phosphide-carbon composites containing different Cu/C ratios (CuP_x-Cy) were investigated for use as a negative electrode material in sodium secondary batteries, whereby the Na[FSA]–[C_3C_1pyrr][FSA] IL electrolyte was employed to optimize the ratio. In this work, phase transition from CuP_2 to Cu_3P and the formation of P-O-C bonds enabled by high energy ball-milling were reported for the first time which were confirmed for CuP_x-C30 (C30 = 30 wt% carbon) and CuP_x-C40 by XRD, TEM, and XPS measurements. The control sample prepared by the ball-milling of CuP_2 and AB in a ratio of 70:30 (w/w) at a lower speed of 500 rpm provided 81% capacity retention after 50 cycles, whereas the sample prepared at 900 rpm exhibited almost 100% capacity retention after 350 cycles, thereby indicating the strong influence of the ball-milling speed on the final electrochemical performance of the material. In addition, CuP_x-C30 exhibited an optimal electrochemical performance compared to the various previous materials, giving a high rate capability of 358 mA h g^{-1} at 8000 mA g^{-1} and 100% capacity retention after 350 cycles at 90 °C. The results of *ex-situ* XRD and XPS analysis of CuP_x-C30 revealed the reversible conversion of Cu_3P and the formation of Na_3P upon charging. The results of EIS tests and the GITT with cycling indicated a clear difference in the electrochemical performances of CuP_x-C20 and CuP_x-C30 during the cyclability tests. More specifically, the interfacial resistance continuously decreased over 100 cycles for CuP_x-C30, whereas it gradually increased after 10 cycles for CuP_x-C20. Overall, this chapter provides better understanding of influence of carbon content in composite materials and demonstrated a high electrochemical performance using CuP_x-C30 and IL electrolyte at both 25 and 90 °C, which renders it suitable for high energy and power density negative electrode material in NIBs. Future work will focus on further scrutiny of the charge-discharge mechanism along with the solid electrolyte interface layer properties in IL electrolytes. In particular, the low sensitivity of X-ray absorption spectroscopy on phosphorus redox renders clarification of the mechanism difficult, and further analytical methods are required. Moreover, effects of mass loading of CuP_x-C30 on rate capability needs to be studied under more practical conditions.

Table 4-1 EIS fitting parameters, R_1, R_2, R_3, Q_2, Q_3, a_2 and a_3, during charge-discharge cycling for CuP$_x$-C20 and CuP$_x$-C30 in the IL electrolyte (see Figure 4-14 for the spectra).

		Resistance / Ω			**CPE / F s$^{(a-1)}$**			
Sample	**Cycle**	R_1	R_2	R_3	Q_2	a_2	Q_3	a_3
CuP$_x$-C20	1	6.02	42.25	3.12	4.87×10^{-6}	0.773	6.04×10^{-5}	0.974
	3	5.87	30.88	6.17	7.49×10^{-6}	0.745	2.62×10^{-5}	0.999
	10	7.05	1.44	4.75	1.83×10^{-5}	1	3.10×10^{-6}	0.863
	50	6.07	7.47	1.79	1.54×10^{-5}	0.75	2.10×10^{-6}	0.915
	100	4.97	10.17	4.52	3.36×10^{-5}	0.646	1.82×10^{-3}	0.469
CuP$_x$-C30	1	4.12	6.25	8.84	5.80×10^{-6}	0.913	6.19×10^{-6}	1
	3	4.18	6.72	7.26	8.03×10^{-6}	1	5.77×10^{-6}	0.903
	10	4.41	2.97	3.61	2.79×10^{-6}	0.963	6.22×10^{-6}	1
	50	3.55	1.21	5.38	4.86×10^{-6}	0.711	1.69×10^{-5}	0.801
	100	4.79	1.68	3.01	9.04×10^{-6}	0.994	8.54×10^{-6}	0.844

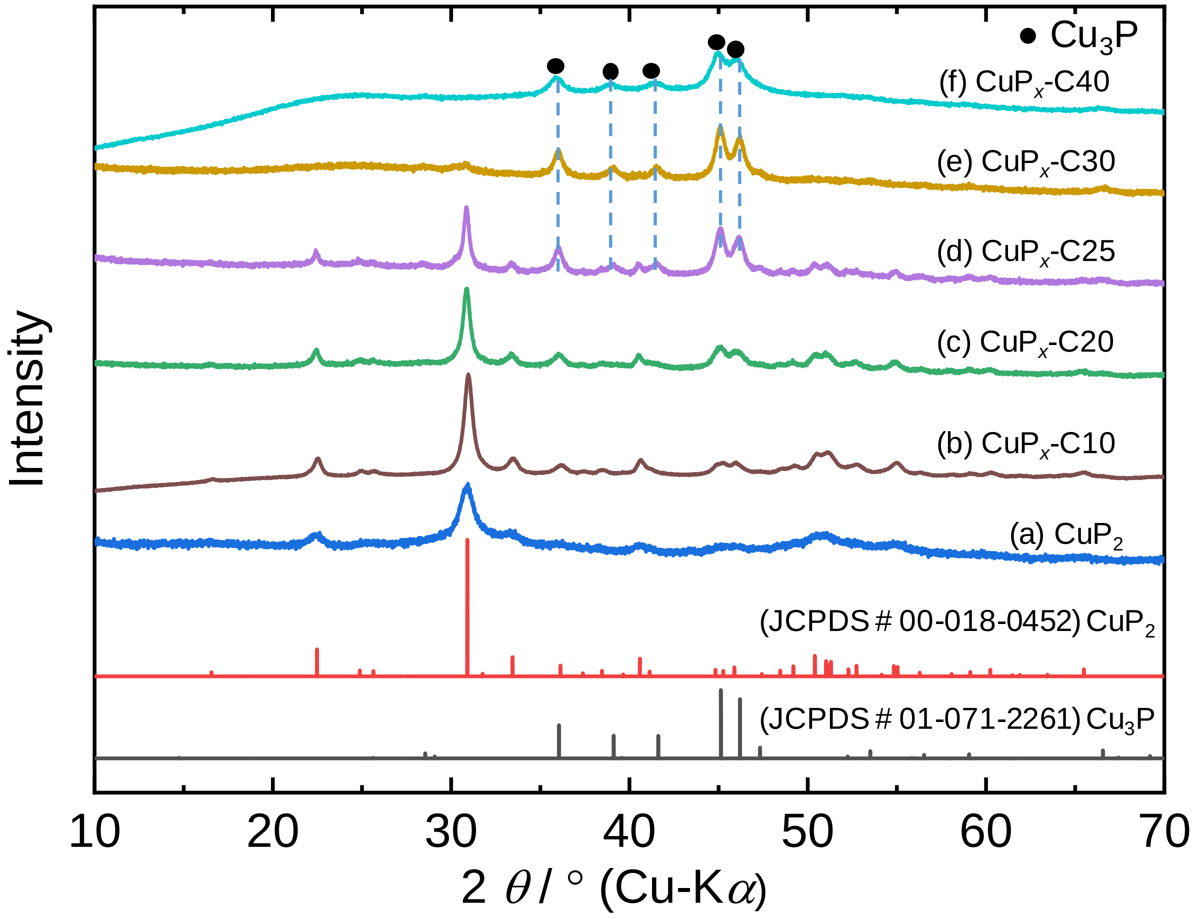

Figure 4-1 XRD patterns of (a) CuP_2, (b) CuP_x-C10, (c) CuP_x-C20, (d) CuP_x-C25, (e) CuP_x-C30, and (f) CuP_x-C40.

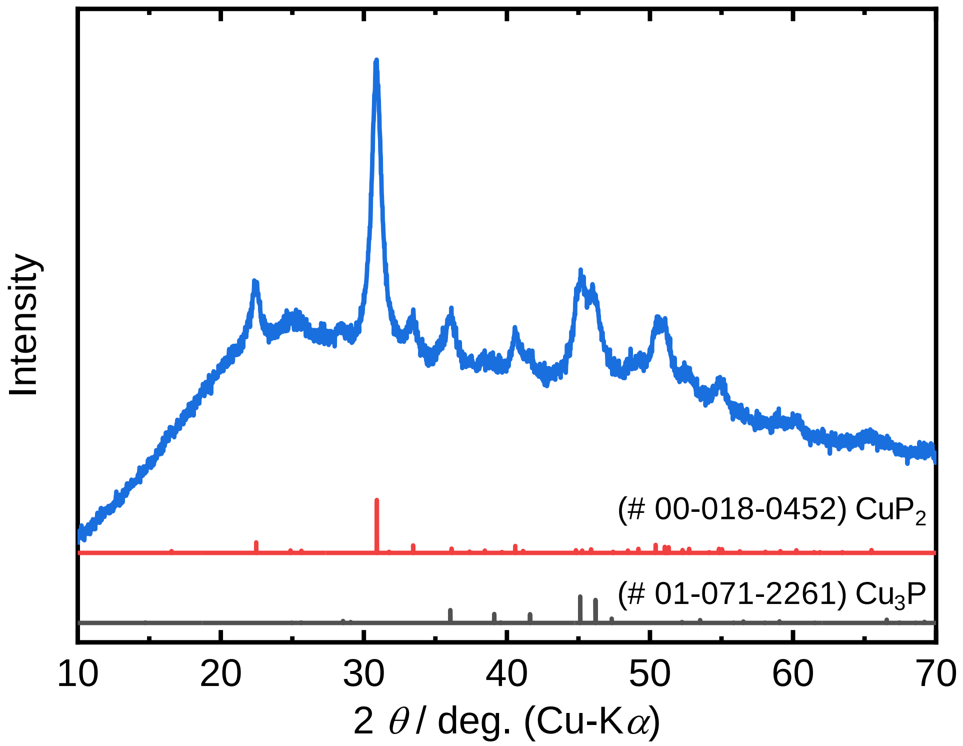

Figure 4-2 XRD patterns of CuP_2 ball-milled with AB in the ratio of 70:30 w/w at 500 rpm for 3 h (CuP_x-C30-500rpm).

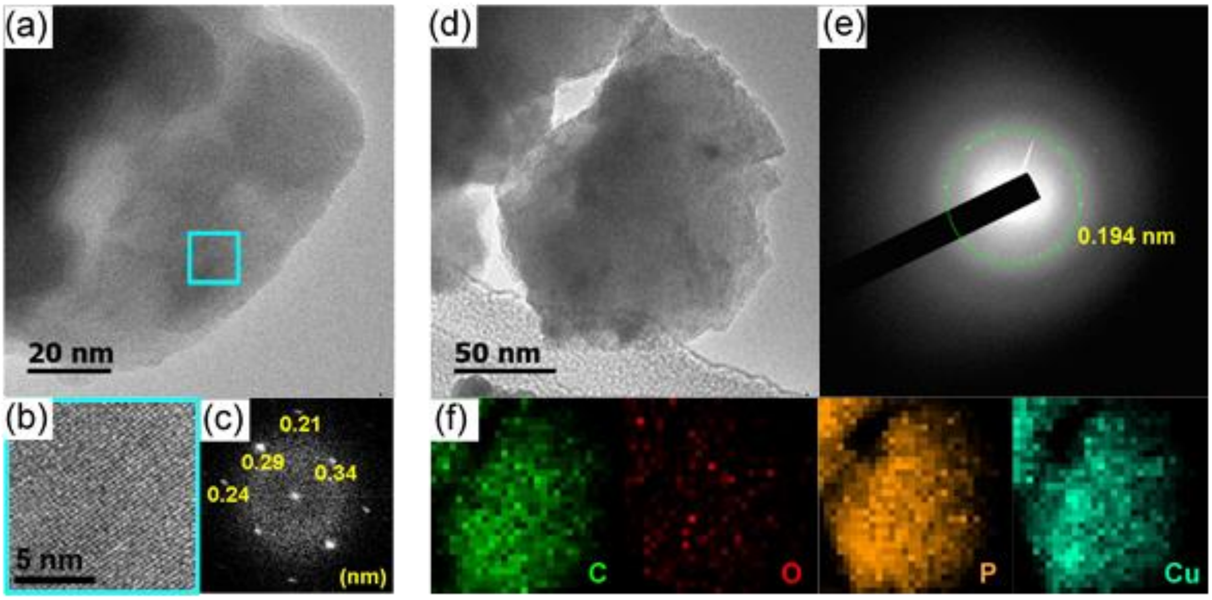

Figure 4-3 (a) TEM image of the pristine CuP$_x$-C20 powder, (b) HRTEM image, and (c) its FFT power spectrum of the selected area indicated by the blue square in (a). (d) TEM image, (e) SAED pattern, and (f) STEM-EDX elemental mappings of the CuP$_x$-C30 pristine powder.

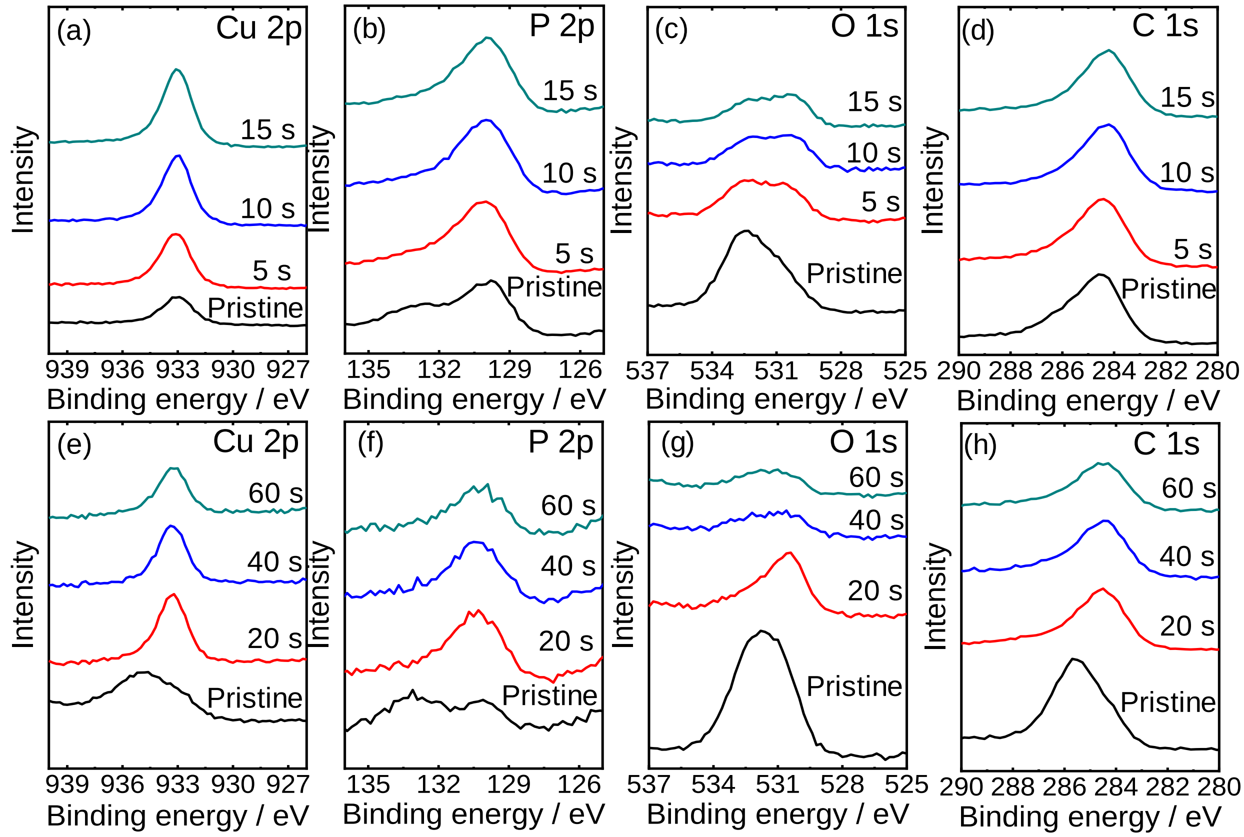

Figure 4-4 The Cu2p, P2p, O1s, and C1s regions of the XPS for the pristine (a–d) CuP$_x$-C20 and (e–h) CuP$_x$-C30 powders.

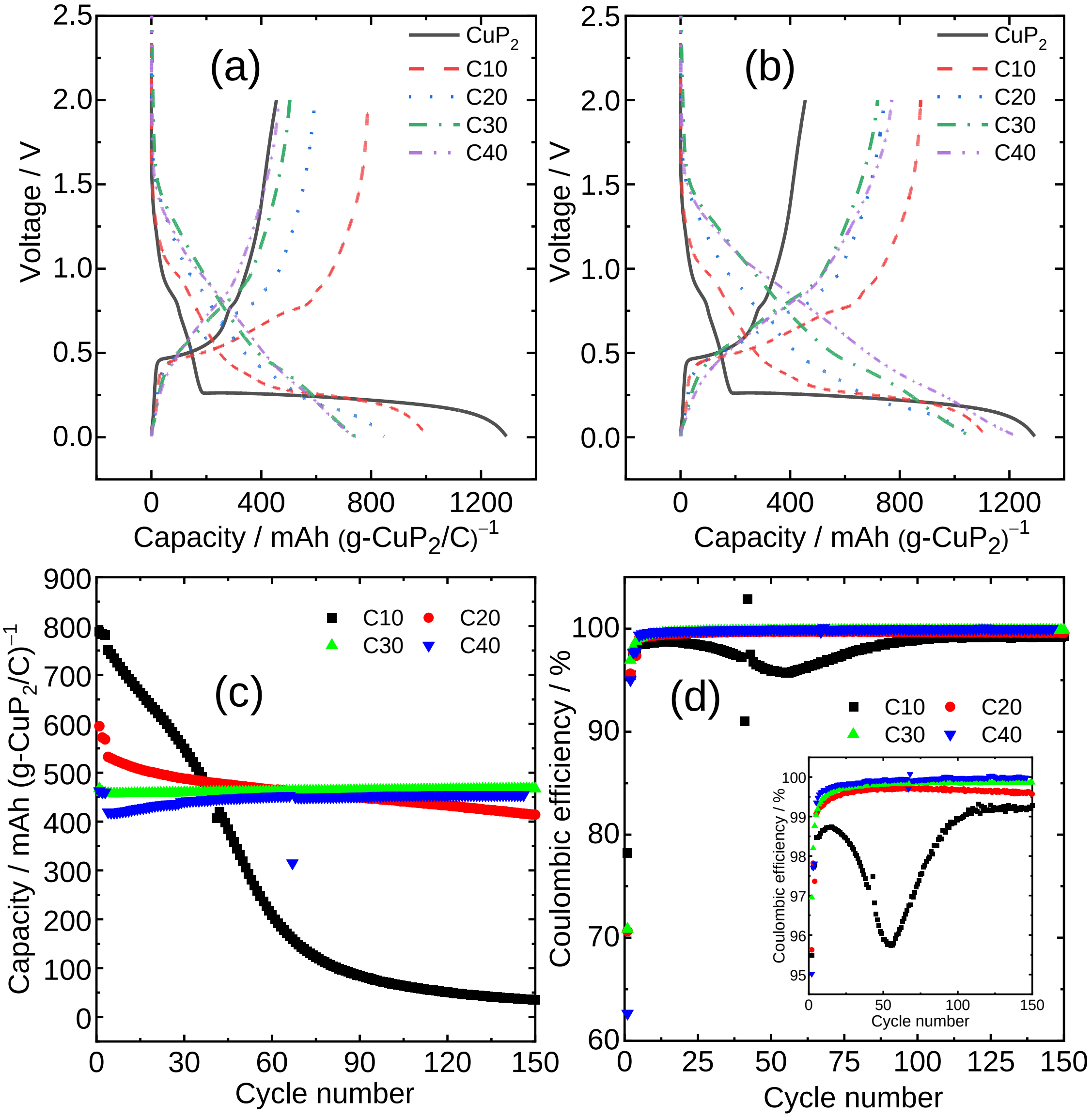

Figure 4-5 (a,b) Galvanostatic charge-discharge curves for the CuP_2 and CuP_x-C composites (C10: CuP_x-C10, C20: CuP_x-C20, C30: CuP_x-C30, and C40: CuP_x-C40) in the IL electrolyte at 90 °C for the first cycle ((a) capacity based on the weight of the composite and (b) capacity based on the weight of CuP_2). Current density = 100 mAg^{-1} and cut-off voltage = 0.005–2.0 V. (c) discharge capacity based on the weight of the composite. (d) Coulombic efficiencies of all composites at 90 °C at a rate of 500 mAg^{-1} (first three cycles at 100 mAg^{-1} for activation) over 150 cycles. The inset in (d) shows the magnified region.

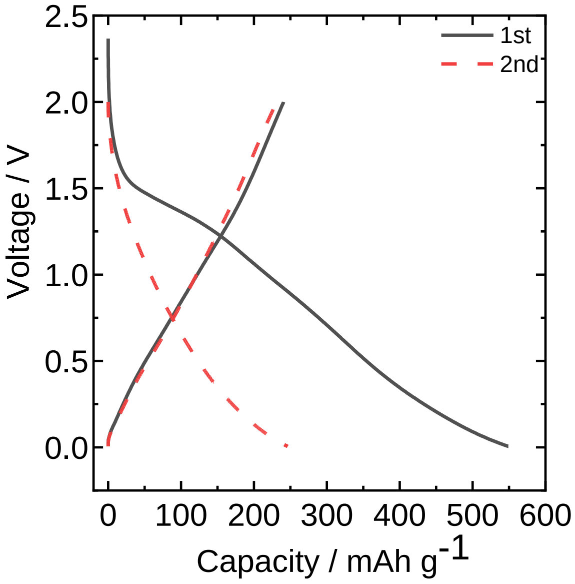

Figure 4-6 Charge-discharge curves of ball-milled AB for 2 cycles at 100 mA g^{-1} at 90 °C using IL. The ball-milling process was carried out at 900 rpm for 3 h. The obtained powder was used as active material for preparing the electrode in the ratio of 90:10 to PAI binder. Capacity contribution of ball-milled AB in CuP_x-C30 is calculated to72 mA h g^{-1} (out of 500 mA h g^{-1}) by 240 x 0.3 mA h g^{-1}.

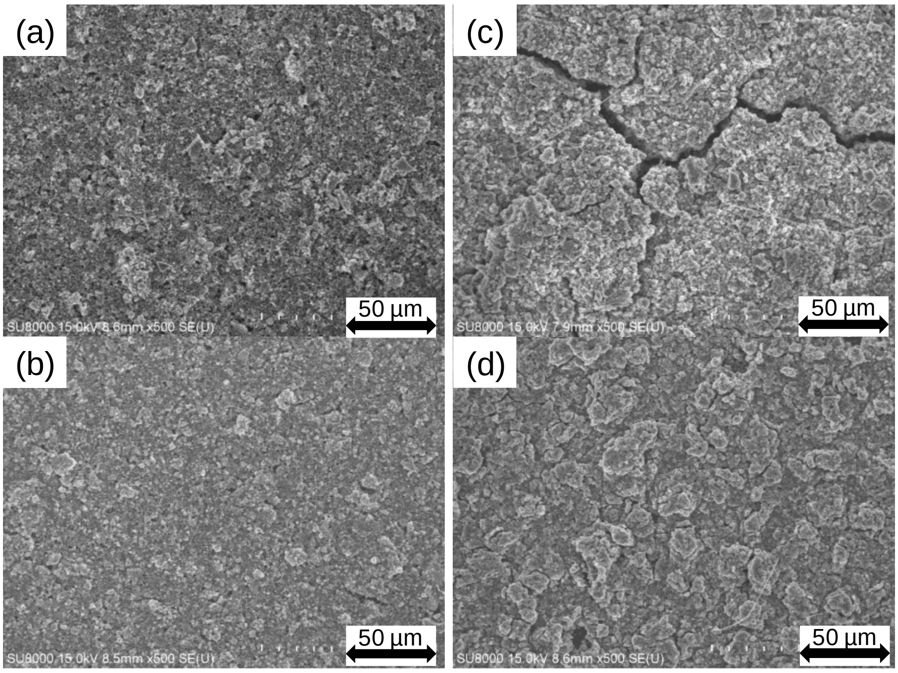

Figure 4-7 SEM images of CuP$_x$-C20 ((a) pristine and (b) after 50 cycles) and CuP$_x$-C30 ((c) pristine and (d) after 50 cycles).

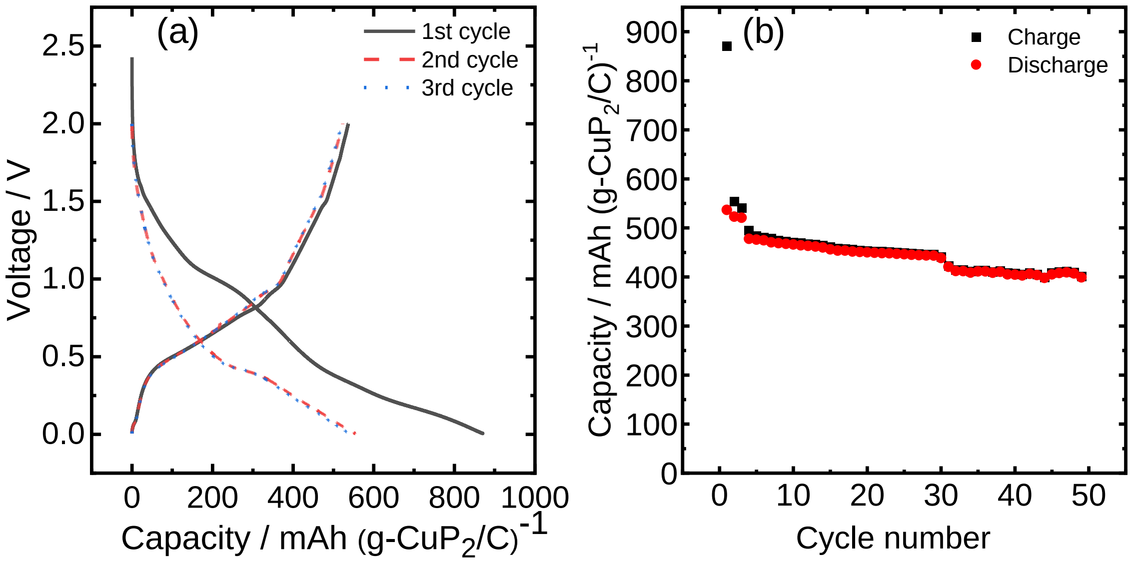

Figure 4-8 (a) Galvanostatic charge-discharge curves of CuP_2-C30 prepared at 500 rpm for 3 h at a current density of 100 mA g^{-1} and cut-off voltage = 0.005–2.0 V at 90 °C for the first three cycles and (b) cycleability at 90 °C at the rate of 500 mA g^{-1} (first three cycles at 100 mA g^{-1} for activation). Electrolyte: IL.

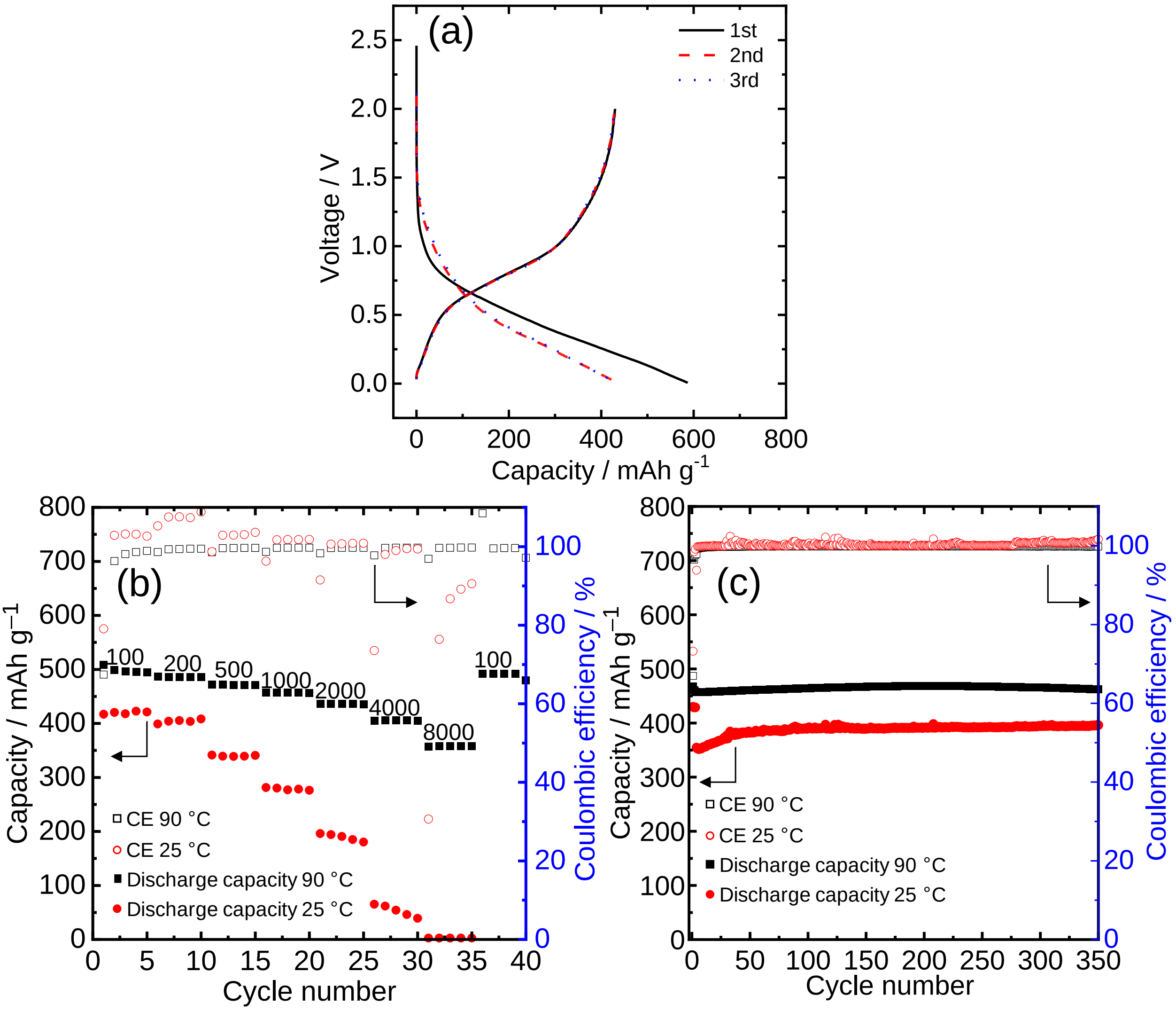

Figure 4-9 Galvanostatic charge-discharge curves of CuP$_x$-C30 in the IL electrolyte at 25 °C at a current density of 100 mA g^{-1} and a cut-off voltage = 0.005–2.0 V for the first three cycles. (b) Rate capability of CuP$_x$-C30 at 25 and 90 °C (rate = 100–8000 mA g^{-1}). (c) Cyclability of CuP$_x$-C30 over 350 cycles at 25 and 90 °C at a rate of 500 mA g^{-1} (first three cycles at 100 mA g^{-1} for activation).

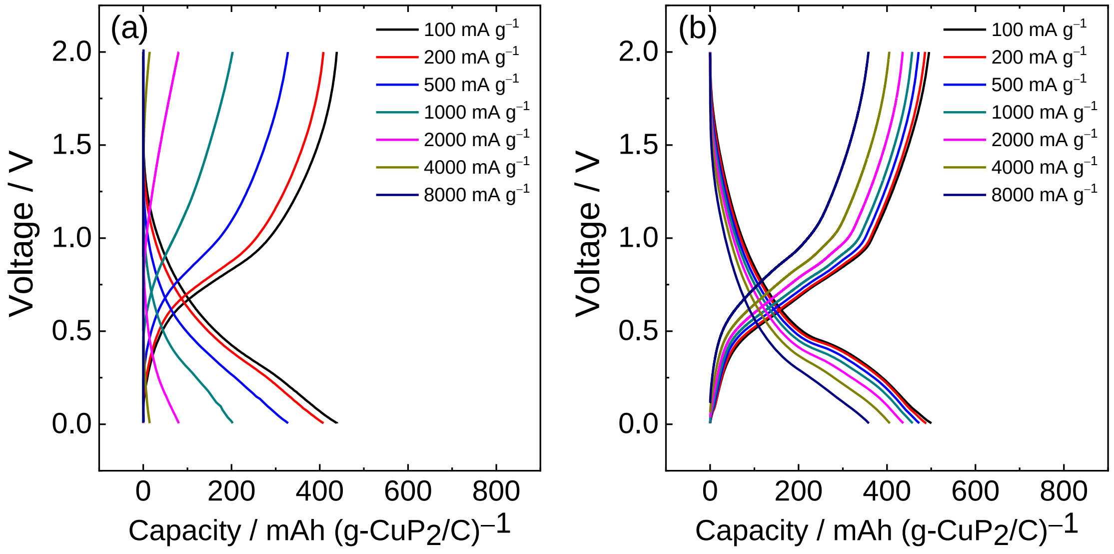

Figure 4-10 Charging and discharging curves of the 5th cycle corresponding to each current mentioned during the rate capability test of CuP$_x$-C30 (see Figure 4-9 (b)) at (a) 25 and (b) 90 °C. cut-off voltage of 0.005–2.0 V using IL.

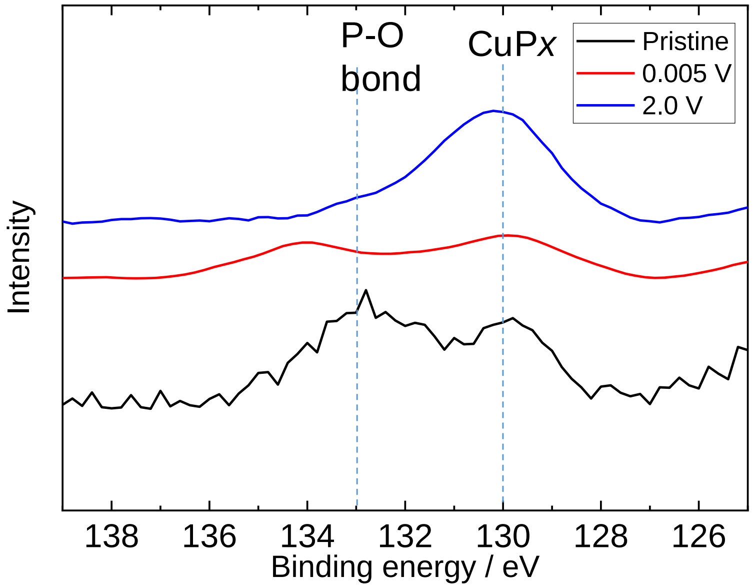

Figure 4-11 P2p XPS spectra of CuP$_x$-C30 (pristine, charged (0.005 V), and discharged (2.0 V)). Charge-discharge test was conducted at 90 °C at the rate of 100 mA g^{-1}, cut-off voltage of 0.005–2.0 V using IL.

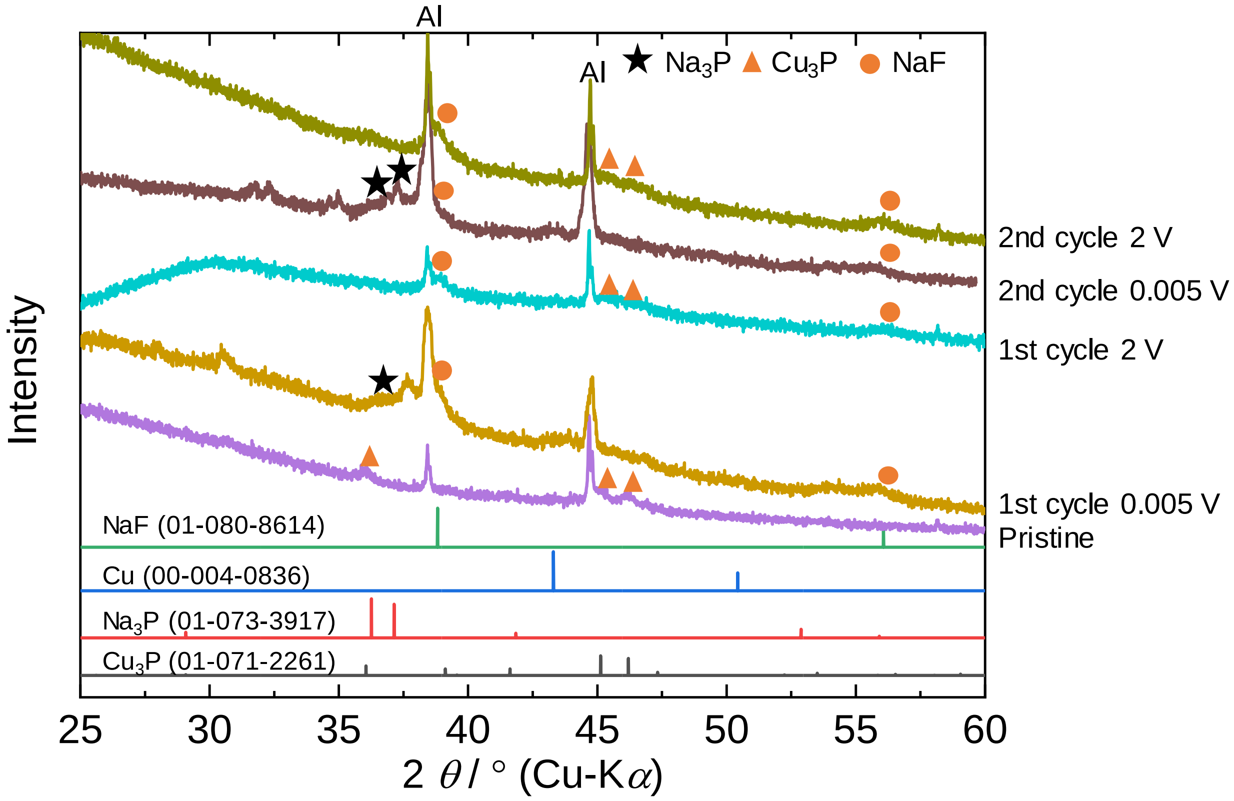

Figure 4-12 *Ex-situ* XRD patterns of the CuP_x-C30 electrode (pristine, charged to 0.005 V (first and second cycles), and discharged to 2 V (first and second cycles)) (see Figure 4-5 (a) for the charge-discharge curves). Current density = 100 mA g^{-1}, cut-off voltage = 0.005–2V, and temperature = 90 °C. The numbers for the reference patterns denote the corresponding ICDD-PDF numbers.

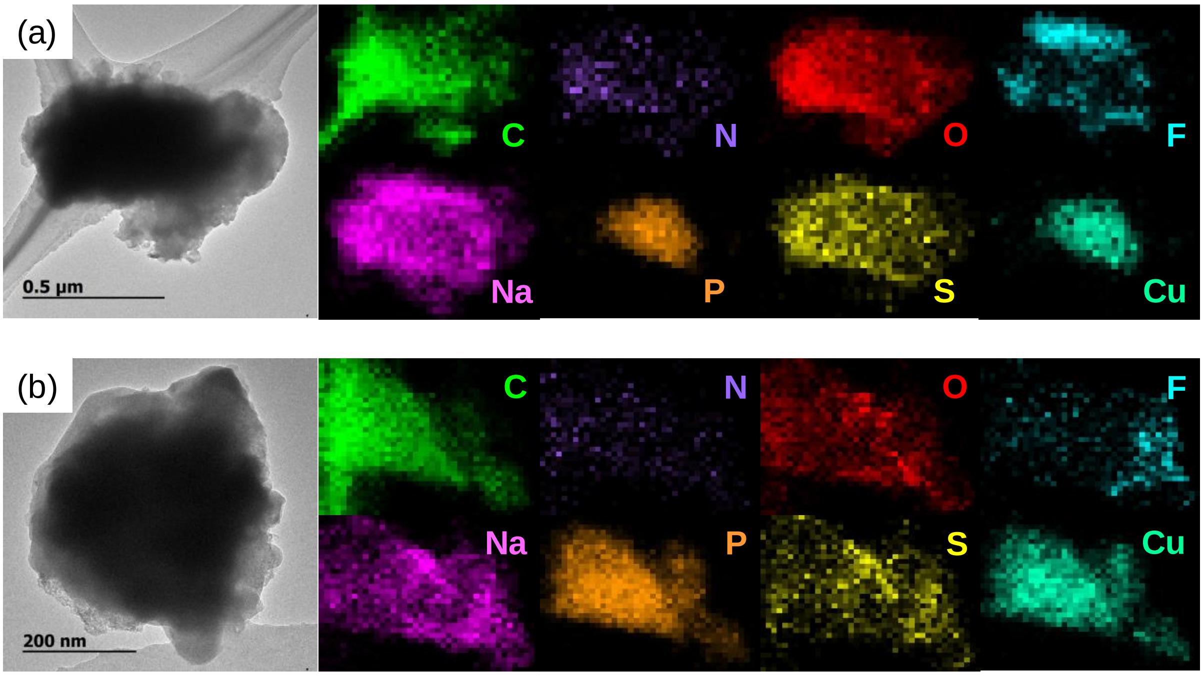

Figure 4-13 *Ex-situ* TEM and EDX of CuP$_x$-C30 after (a) charging and (b) discharging in the first cycle. Charge-discharge test was conducted at 90 °C at the rate of 100 mA g^{-1}, cut-off voltage of 0.005–2.0 V using IL. The elements, N, O, F, Na, and S, are observed over the C mapping, suggesting SEI formation on the entire composite.

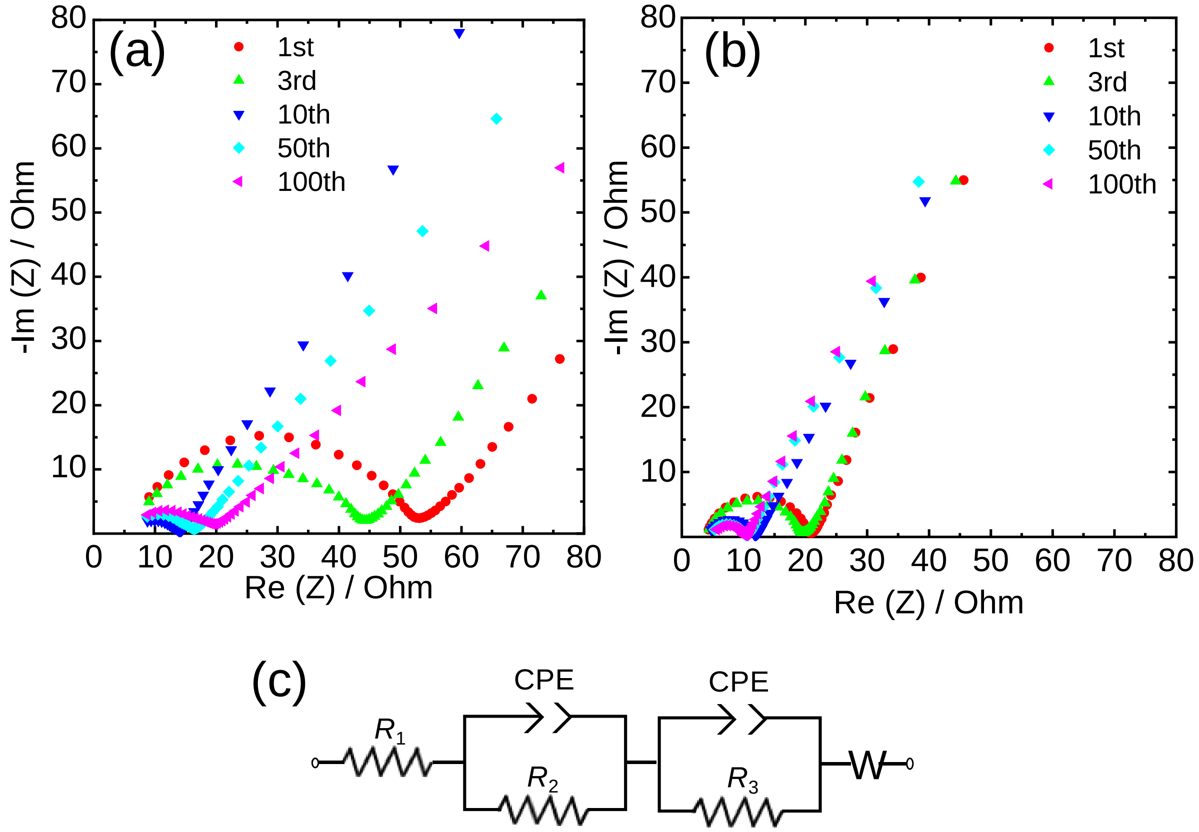

Figure 4-14 EIS results for (a) CuP$_x$-C20 and (b) CuP$_x$-C30 over 100 cycles in the IL electrolyte at 90 °C. Charge-discharge conditions: rate = 500 mA g^{-1} (100 mAg^{-1} for the first three cycles) and cut-off voltage = 0.005–2 V. The electrodes were charged and discharged for 1, 3, 10, 50, and 100 cycles, and then charged to 0.5 V during the subsequent charging step. Impedance spectra were measured at a constant cell voltage of 0.5 V with an amplitude of 20 mV and frequency range of 100 kHz−10mHz. (c) The equivalent circuit to fit the EIS data (see Table 4-1 for fitting parameters).

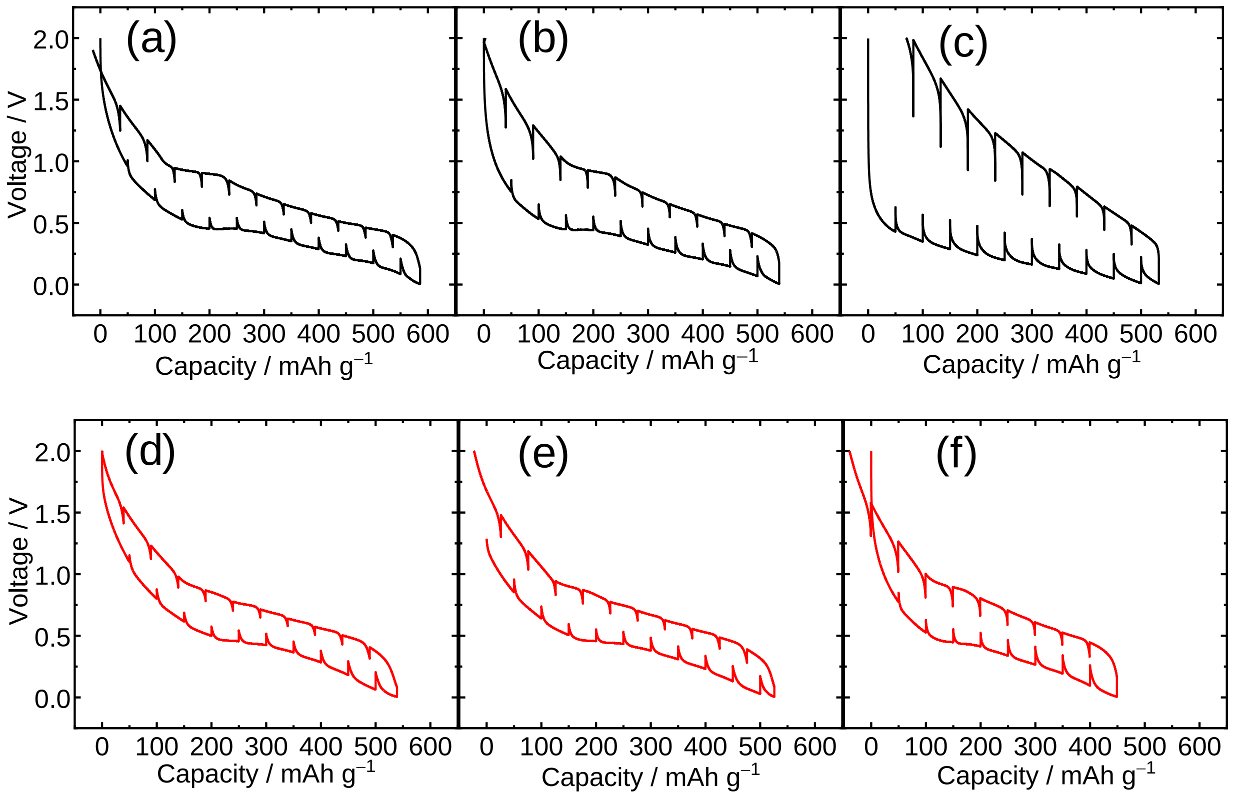

Figure 4-15 GITT curves for (a–c) CuP$_x$-C20 and (d–f) for CuP$_x$-C30 ((a, d) 3rd cycle, (b, e) 50th cycle, and (c, f) 100th cycle) in the IL electrolyte at 90 °C. The cut-off voltage was 0.005–2.0 V. A current density of 100 mA g^{-1} was applied for 1 h, followed by 8 h relaxation.

References

[1] J. Wang, C. Luo, T. Gao, A. Langrock, A.C. Mignerey, C. Wang, Small, 11 (2015) 473-481.

[2] C. Wu, P. Kopold, P.A. van Aken, J. Maier, Y. Yu, Adv. Mater., 29 (2017) 1604015.

[3] L. Wu, X. Hu, J. Qian, F. Pei, F. Wu, R. Mao, X. Ai, H. Yang, Y. Cao, J. Mater. Chem. A, 1 (2013) 7181-7184.

[4] Q.-R. Yang, W.-J. Li, S.-L. Chou, J.-Z. Wang, H.-K. Liu, RSC Adv., 5 (2015) 80536-80541.

[5] K. Zhang, M. Park, J. Zhang, G.-H. Lee, J. Shin, Y.-M. Kang, Nano Res., 10 (2017) 4337-4350.

[6] E. Pan, Y. Jin, C. Zhao, M. Jia, Q. Chang, M. Jia, J. Alloys Compd., 769 (2018) 45-52.

[7] J. Lee, Y.-M. Chen, Y. Zhu, B.D. Vogt, RSC Adv., 5 (2015) 99329-99338.

[8] S.-M. Oh, J.-Y. Hwang, C.S. Yoon, J. Lu, K. Amine, I. Belharouak, Y.-K. Sun, ACS Appl. Mater. Interfaces, 6 (2014) 11295-11301.

[9] J. Song, Z. Yu, M.L. Gordin, X. Li, H. Peng, D. Wang, ACS Nano, 9 (2015) 11933-11941.

[10] S.-O. Kim, A. Manthiram, Chem. Commun., 52 (2016) 4337-4340.

[11] W. Qi, H. Zhao, Y. Wu, H. Zeng, T. Tao, C. Chen, C. Kuang, S. Zhou, Y. Huang, Sci. Rep., 7 (2017) 43582.

[12] M. Ihsan-Ul-Haq, H. Huang, J. Cui, S. Yao, J. Wu, W.G. Chong, B. Huang, J.-K. Kim, J. Mater. Chem. A, 6 (2018) 20184-20194.

[13] Y. Zhang, H. Tao, J. Li, X. Yang, Ionics, 26 (2020) 3377-3385.

[14] M. Dahbi, M. Fukunishi, T. Horiba, N. Yabuuchi, S. Yasuno, S. Komaba, J. Power Sources, 363 (2017) 404-412.

[15] J. Huang, X. Guo, X. Du, X. Lin, J.-Q. Huang, H. Tan, Y. Zhu, B. Zhang, Energy Environ. Sci., 12 (2019) 1550-1557.

[16] Y. Domi, H. Usui, K. Yamaguchi, S. Yodoya, H. Sakaguchi, ACS Appl. Mater. Interfaces, 11 (2019) 2950-2960.

[17] C.-Y. Li, J. Patra, C.-H. Yang, C.-M. Tseng, S.B. Majumder, Q.-F. Dong, J.-K. Chang, ACS Sustain. Chem. Eng., 5 (2017) 8269-8276.

[18] O. Olofsson, Acta Chem. Scand., 19 (1965) 229-241.

[19] T.D. Shen, W.Q. Ge, K.Y. Wang, M.X. Quan, J.T. Wang, W.D. Wei, C.C. Koch, Nanostruct. Mater., 7 (1996) 393-399.

[20] M. Nusheh, H. Yoozbashizadeh, M. Askari, N. Kuwata, J. Kawamura, J. Kano, F. Saito, H. Kobatake, H. Fukuyama, ISIJ Int., 50 (2010) 668-672.

[21] Y.-S. Kwon, K.B. Gerasimov, S.-K. Yoon, J. Alloys Compd., 346 (2002) 276-281.

[22] R. Schmidt, H. Martin Scholze, A. Stolle, Int. J. Ind. Chem, 7 (2016) 181-186.

[23] F. Parmigiani, G. Pacchioni, F. Illas, P.S. Bagus, J. Electron. Spectrosc. Relat. Phenom., 59 (1992) 255-269.

[24] V.I. Nefedov, Y.V. Salyn, E.P. Domashevskaya, Y.A. Ugai, V.A. Terekhov, J. Electron. Spectrosc. Relat. Phenom., 6 (1975) 231-238.

[25] J. Hwang, K. Matsumoto, R. Hagiwara, J. Phys. Chem. C, 122 (2018) 26857-26864.

Chapter 5

Fabrication and Performance of Vanadium Phosphide–phosphorus Composite Negative Electrode

5.1 Introduction

Recently, phosphorus-based compounds are being widely used as negative electrodes in NIBs owing to the high theoretical capacity (~2596 mA h g^{-1}) of elemental phosphorous, due to the formation of Na_3P after sodiation [1, 2]. However, due to the low electrical conductivity of phosphorus (~10^{-14} S cm^{-1}) and large change in volume during sodiation and desodiation, severe capacity fade is often observed. The difficulties arising from the large volume change can be attenuated by using metal phosphides, including Cu_3P [3], FeP_4 [4], and Sn_4P_3 [5], which form a conductive matrix of metal after sodiation. However, the cycleability and rate capability are still limited. Although the introduction of carbon to the metal phosphide improves the rate capability and cycle performance as shown in Chapters 3 and 4, the tap density of the material decreases because of the low density of carbon, while the first-cycle Coulombic efficiency reduces due to the side reactions arising from the large surface area. Therefore, a metal phosphide with a buffer, other than carbon, may give a new direction for fabricating negative electrodes for NIBs.

The P–TiP_2–C composite prepared by ball-milling showed excellent cycleability and rate performance as a negative electrode for both LIBs and NIBs [6]. TiP_2 could buffer against the large volume change during the sodiation/desodiation, owing to its structural stability and inactivity toward sodiation/desodiation. Vanadium phosphides (VP, V_4P_7, and VP_2) have been already investigated as negative electrodes for LIBs [7-9]; VP showed a moderate capacity with good cycleability owing to a very low volume change during cycling, while VP_2 exhibited high capacity but poor cycleability. The characteristics of V_4P_7 was intermediate between the other two phosphides, and it exhibited high capacity as well as good cycleability and rate capacity [8]. XRD and XAS analyses suggest that all the aforementioned vanadium phosphides function according to an insertion mechanism. A recent study for V_4P_7 for NIBs showed excellent cycleability and rate performance [10]. This may be related to the relatively low resistivity of V_4P_7 (2×10^{-4} ohm cm) [11]. However, for seeking high energy density of batteries, a higher capacity of negative electrode materials is required. From this point of view, it will be interesting V_4P_7/P composite as a strong candidate for the negative electrode the NIBs.

Several studies in the past few years have suggested that some negative and positive electrodes exhibit better performance with ILs than with organic electrolytes [12-14]. This is partly explained by the formation of a uniform solid electrolyte interface (SEI) layer in the first cycle and suppression of large volume change in negative electrodes [15]. Another advantage of using ILs is their compatibility with operation at elevated temperatures because of their thermal stability. This is because both the diffusion of Na^+ ions and the electrode reactions are enhanced at elevated temperatures; such a temperature range above room temperature is defined as the intermediate temperature [16, 17]. A recent report demonstrated a considerable reduction in the interfacial resistance at intermediate temperatures using ILs [18]. Pyrrolidinium-based binary ILs are known to provide a stable passivation layer, especially in phosphorus-based systems [19, 20]. All these observations motivated the author to investigate ILs as electrolytes in the present study. A vanadium phosphide–phosphorus composite, V_4P_7/5P (and analogues with different V/P ratio), was investigated as a negative electrode in NIBs at 25 and 90 °C, using the Na[FSA]–[C_3C_1pyrr][FSA] IL electrolyte. This IL is used owing to its remarkable electrochemical performance observed in NIBs [21, 22].

5.2 Experimental

The vanadium phosphide/phosphorus composite, V_4P_7/5P, was prepared by one-step HEBM of vanadium metal (Kojundo Chemical Lab, purity 99.9%) and phosphorus powder (Wako Pure Chemical Industries, purity 98%) in a stoichiometric ratio under Ar atmosphere. The ball to powder ratio was kept at 50:1 at 400 rpm for 20 h. In order to see the effect of the V/P ratio, V_4P_7, V_4P_7/5P (V:P = 4:12), V_4P_7/9P (V:P = 4:16), and V_4P_7/13P (V:P = 4:20) were prepared by HEBM in the same condition. Based on the capacity value and capacity retention of the composites, V_4P_7/5P was selected as the main material for investigation (Figure 5-1). The XRD patterns of the samples were obtained with the aid of a Rigaku SmartLab diffractometer (Cu Kα, 40 kV−30 mA). Particle size, morphology, structural parameters, and elemental composition were analyzed by SEM (Hitachi SU-8020) and STEM (JEOL JEM-2100F). The chemical bonding states were analyzed by XPS (JEOL, JPS-9010, MgKα, 10 kV-10 mA).

The test electrodes were prepared by mixing the active material (V_4P_7, V_4P_7/5P, V_4P_7/9P, V_4P_7/13P), AB (Wako Pure Chemical Industries), and a carboxymethyl cellulose/styrene-butadiene binder in a weight ratio of 75:15:5:5 in water. The resulting slurry was subsequently cast on an Al foil and dried under vacuum, first at 90 °C for 10 h and then overnight at 120 °C (mass loading: ~1 mg cm^{-2}). A glass fiber filter (Whatman, GF-A, 260 μm in thickness and 16 mm in diameter) was used as a separator, and a Na metal disc (Aldrich, purity 99.9%) was used as a counter electrode. Electrochemical performance was tested by assembling a 2032 coin cell under Ar atmosphere. The electrochemical impedance spectroscopy measurements were performed with a VSP potentiostat (Bio-Logic) at 25 and 90 °C over a frequency range from 100 mHz to 100 kHz, with an AC amplitude of 20 mV.

5.3 Results and discussion

Figure 5-2 (a) shows the XRD pattern of V_4P_7/5P prepared by HEBM. All the peaks are assigned to tetragonal V_4P_7 (space group *P*−4m2) that has a partial occupancy of 0.75 for one of the two P sites; [11] however, a slight deviation in the stoichiometry is possible. The XRD pattern suggests the formation of a crystalline V_4P_7 phase with an amorphous red phosphorus phase (5P, considering the mixing ratio of V and P in the beginning), although the latter cannot be detected by XRD. On the other hand, the peaks of V_4P_7, V_4P_7/9P, and V_4P_7/13P are also indexed to V_4P_7 (Figure 5-3), suggesting the increase of the P/V ratio simply leads to the increase of the amorphous phosphorus phase. The particle size and morphology were analyzed by SEM (Figure 5-2(b)). Continuous collision and fracture during ball-milling resulted in a random morphology of the particles. The size of the particles ranges from 500 nm to a few micrometers. Elemental mapping in the energy-dispersive X-ray (EDX) spectrum suggests that the elements in the V_4P_7/5P composite were uniformly distributed in the particle (Figure 5-2(c)). A small amount of oxygen, as confirmed from the mapping, can be attributed to the oxidation of the elements during ball-milling owing to the high rotational speed of operation. This was further confirmed by the presence of oxide (V^{2+}) peaks around 522.1 and 513.6 eV and V^{5+} peaks (516.7 and 523.2 eV) in the V2p XPS and at 134 eV in the P2p XPS owing to -PO_4- bond in $VOPO_4$ (Figure 5-4 (a) and (b)). The peaks in V2p and P2p (512.7 and 130.1 eV, respectively) can be indexed to both the existence of elemental vanadium (512.6 eV), phosphorus (130.1 eV), and the formation of V_4P_7 because the binding energies are very close to each other. Although there is no XPS data for V_4P_7, its binding energy is considered to be close to that of VP (V2p;512.6 and $P2p_{3/2}$; 129.1 eV) because the binding energies of the same elements in the most 3d transition metal phosphides, including phosphorus, are similar to each other ($P2p_{3/2}$ for FeP, MnP, and TiP are 129.5, 129.4, and 128.4 eV, respectively) [23].

To obtain the composition of V_4P_7/5P and to confirm the presence of excess elemental phosphorus in the amorphous structure, further characterization is required. Therefore, the high-resolution HRTEM image of the pristine powder was captured (Figure 5-5 (a)). The *d*-spacing of V_4P_7/5P was estimated by the fast Fourier transformation (FFT, Figure 5-5 (b)) of two specific regions. The results confirmed the formation V_4P_7 nanocrystallites of size 5–15 nm, embedded within the amorphous phosphorus matrix. Elemental mapping of the composite also supports this argument, as the excess phosphorus can be observed around the nanocrystallites of V_4P_7 (Figure 5-5 (c)). The atomic ratio of P and V, calculated for several particles by STEM-electron energy loss spectroscopy, was in the range 2.3–2.6 (Figure 5-6), which is in good agreement with the ratio of the materials examined by HEBM.

The electrochemical performance of the V_4P_7/5P composite with IL as the electrolyte is shown in Figure 5-7. Figures 5-7 (a) and (b) represent the galvanostatic charge–discharge curves at 25 and 90 °C, respectively, for the first three cycles at 100 mA g^{-1} in the voltage range 0.005–2 V. The curves at 25 °C for the charging process (Figure 5-7 (a)) of the first cycle consists of a sloping profile with one indistinct plateau around 0.15 V. A high first-cycle Coulombic efficiency of 88% indicates that the side reactions in the first cycle are highly suppressed in this electrode in an IL, in contrast to that reported for other negative electrodes such as hard carbon and phosphides, wherein the efficiency was typically lower than 75% [4, 24]. During desodiation, all the curves for the first three cycles overlap with each other, which indicates a reversible extraction of sodium from the composite matrix. The curves obtained at 90 °C (Figure 5-7 (b)) are indicative of lesser polarization and contains more plateaus owing to the increase in temperature. The plateau at 0.25 V is more distinct than that at 25 °C for the same voltage. Details on plateau potentials are further discussed by cyclic voltammetry (Figure 5-8). At 100 mA g^{-1}, the high first-cycle discharge capacities at 25 and 90 °C were 560 and 738 mA h g^{-1}, respectively, while the Coulombic efficiencies at 25 and 90 °C were 88% and 86%, respectively. In the rate capability test at 90 °C (Figure 5-7 (c)), this system exhibited high discharge capacities of 695, 537, and 360 mA h g^{-1} at the rates of 100, 1000, and 8000 mA g^{-1}, respectively.

Even at 25 °C, reasonable discharge capacities of 588, 271, and 155 mA h g^{-1} were observed at the rates of 100, 1000, and 2000 mA g^{-1}, respectively. Figure 5-7 (d) shows the cycle performance (the first two cycles were performed at 100 mA g^{-1}) for 100 cycles at 25 °C (rate:200 mA g^{-1}) and 90 °C (rate: 500 mA g^{-1}). In the fourth cycle, the discharge capacities at 25 and 90 °C were 548 and 613 mA h g^{-1}, respectively, while the Coulombic efficiencies at the same temperatures were 99.2% and 99.3%, respectively. The capacity increased for the first 20 cycles at 25 °C owing to the activation and then gradually decreased. Cycleability test at 90 °C indicated a constant capacity for few cycles, followed by a decrease in the capacity. This is similar to that observed at 25 °C. After 100 cycles, the capacity retention reached 54 and 48% at 25 and 90 °C, respectively, with corresponding Coulombic efficiencies of 98.1 and 99.1%, respectively. The cycleability was also evaluated at 25 °C using 1 mol dm^{-3} $NaPF_6$ in an organic electrolyte, ethylene carbonate/diethylene carbonate (1:1 (v/v)), in order to compare the performance with that in the IL electrolyte. The first charge–discharge curves at the rate of 100 mA g^{-1} (cut-off voltage range 0.005–2.0 V) delivered a discharge capacity of 605 mA h g^{-1}, with a Coulombic efficiency as high as 88% (Figure 5-9 (a)). Although the reaction was reversible till the fifth cycle, severe capacity degradation was observed after that (Figure 5-9 (b)). A similar behavior was also reported for Sn_4P_3 and phosphorous negative electrodes [19], wherein the SEI layer was found to be non-uniform in the organic electrolyte. Na[FSA]-[C_3C_1pyrr][FSA], however, provided a uniform passivation layer.

The electrochemical performance of the V_4P_7 electrode was measured at 25 and 90 °C for comparison. Figures 5-10 (a) and 5-1 (a) show the charge-discharge curves at 100 mA g^{-1} for the first three cycles at 25 and 90 °C, respectively. The obtained reversible discharge capacity at 25 °C with IL is 270 mA h g^{-1} (~1 Na^+ per $VP_{1.75}$ unit) which is similar to the reported value in the previous report [10] but when the temperature is raised to 90 °C, the discharge capacity for first cycle reaches 470 mA h g^{-1} (1.85 Na^+ per $VP_{1.75}$ unit) with the initial

Coulombic efficiency of 71%. Although V_4P_7 exhibits a high cycleability, V_4P_7/5P has an advantage in capacity. Increase of phosphorus content in the composite (V_4P_7/9P, and V_4P_7/13P) increases the first cycle capacity at the cost of severe capacity fading. By considering these data, V_4P_7/5P is regarded as a well-balanced material in this series in terms of capacity and cycleability.

The charge–discharge mechanism was investigated by *ex-situ* XRD (Figure 5-11). The rate of charging and discharging were 100 mA g^{-1}, in the cut-off voltage range of 0.005–2 V. The XRD pattern of the pristine sample shows peaks corresponding to V_4P_7. There is no difference between the XRD patterns of the pristine sample and the one charged at 0.24 V. Peaks for Na_3P could be observed after charging to 0.005 V, although the peaks corresponding to V_4P_7 remained intact. This result is similar to the previous report which observed no change in the peaks of V_4P_7 [10]. Na_3P was desodiated during discharging, as evident from the decrease in the number and intensities of the XRD peaks of Na_3P at 0.54 V. The peaks completely disappeared at 2 V. The XRD patterns in the second cycle indicates the reversibility of the reaction. Moreover, the *ex-situ* XRD of the V_4P_7 electrode also supports the arguments above as there is no change in the peaks for charged and discharged samples (Figure 5-12).

To see the change in resistance with cycling in different electrolytes, impedance spectra of V_4P_7 /5P were measured in a half cell configuration with IL (25 and 90 °C) and organic electrolytes at 25 °C (Figure 5-13 (a), (b) (inset: magnified plot) and (c)), respectively. The V_4P_7/5P electrode was charged and discharged for one, three, and ten cycles, and then charged to 0.5 V during the next charging step. A constant decrease in the interfacial resistance until the tenth cycle is performed in IL at both 25 and 90 °C, although the initial value of interfacial resistance for IL at 25 °C is larger than that for organic electrolyte due to the development of surface film between Na metal and IL electrolyte, [18] while the interfacial resistance increases drastically after the first cycle in the organic electrolyte. This correlates with the cycleability test, confirming the benefit of IL over organic electrolytes with respect to the performance. This result is further supported by the surface analysis of electrode after 10 cycles in IL and organic electrolyte by SEM (Figure 5-14 (b) and (c), respectively). Substantial increase in particle size is clearly evident in the case of organic electrolyte whereas it is almost the same as pristine (Figure 5-14 (a)) in IL electrolyte. Similar results were reported in case of silicon negative electrode in LIBs [15].

The enthalpy of formation [25] and reaction mechanism for some selected 3d transition metal phosphides (MP_x with low x value) used in LIBs and NIBs are summarized in Table 5-1. The enthalpy of formation of MP_x (per mole of the respective transition metals) increases with increasing atomic number, and titanium and vanadium phosphides have significantly small (large negative) enthalpies of formation. This prevents the conversion reaction of these phosphides with high lattice energy in both LIBs and NIBs, and it was certainly reported that V_4P_7 works based on the topotactic insertion mechanism [10]. All the late 3d transition metal phosphides are active for the conversion reaction because of their low negative enthalpies of formation. Further discussion from the viewpoint of thermodynamics is difficult here because of the lack of reliable data.

5.4 Conclusions

In this chapter, the use of a $V_4P_7/5P$ composite as a negative electrode for NIBs was investigated, using an IL as the electrolyte. The XRD, HRTEM, SEM, and XPS analyses confirmed the formation of $V_4P_7/5P$ and revealed the morphology and particle size. High reversible capacities of 560 mA h g^{-1} with a Coulombic efficiency of 88%, and 738 mA h g^{-1} with a Coulombic efficiency of 86% were observed at 25 and 90 °C, respectively, in the absence of carbon materials as conductive additive. A capacity of 360 mA h g^{-1} was obtained even at a high rate of 8000 mA g^{-1} at 90 °C, and 47.2% capacity retention was achieved at 100th cycle.

The *ex-situ* XRD analysis revealed the reversible sodiation and desodiation of phosphorus in Na_3P and the insertion mechanism of V_4P_7 phase. The advantage of V_4P_7 is to provide mechanical integrity, electrical conductivity and capacity to the electrode for better performance. Moreover, the interfacial layer in IL is better than that in the organic electrolyte. The results obtained here demonstrates a good performance and safer operation by utilizing metal phosphide and IL in NIBs to extend to the practical applications of large-scale batteries without the use of rare elements.

Table 5-1 Enthalpy of formation (per mole of the respective transition metal) and type of reaction mechanism of selected transition metal phosphides (MP_x) for LIBs and NIBs [25] (insertion = I, conversion = C, and not available = NA).

MP_x	**Enthalpy of formation**	**Type of reaction mechanism**	
		LIBs	NIBs
TiP	−265 kJ mol^{-1} [35]	NA	NA
TiP_2	NA	I [6]	Inactive [6]
V_4P_7	−260 kJ mol^{-1} [36]	I [8]	I (this work, [10])
VP	−234 kJ mol^{-1} [36]	I [7]	NA
MnP	−173 kJ mol^{-1} [36]	I +C [26]	NA
FeP	−140 kJ mol^{-1} [36]	I +C [27]	C [28]
CoP	−126 kJ mol^{-1} [36]	C [29]	C [30]
NiP_3	−112 kJ mol^{-1} [36]	C [31]	C [32]
CuP_2	−88 kJ mol^{-1} [37]	C [33]	C [33]
Zn_3P_2	−54 kJ mol^{-1} [37]	I +C [32]	C [34]

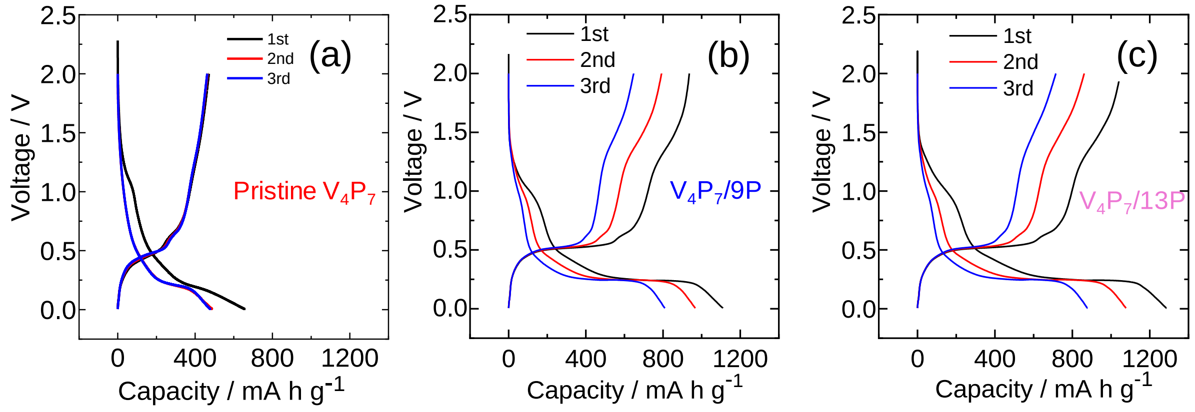

Figure 5-1 Galvanostatic charge–discharge curves of the (a) V_4P_7, (b) V_4P_7/9P (V:P = 4:16), and (c) V_4P_7/13P (V:P = 4:20) composite electrodes in IL electrolyte at 90 °C (rate: 100 mA g^{-1}, voltage range: 0.005–2.0 V) for the first three cycles.

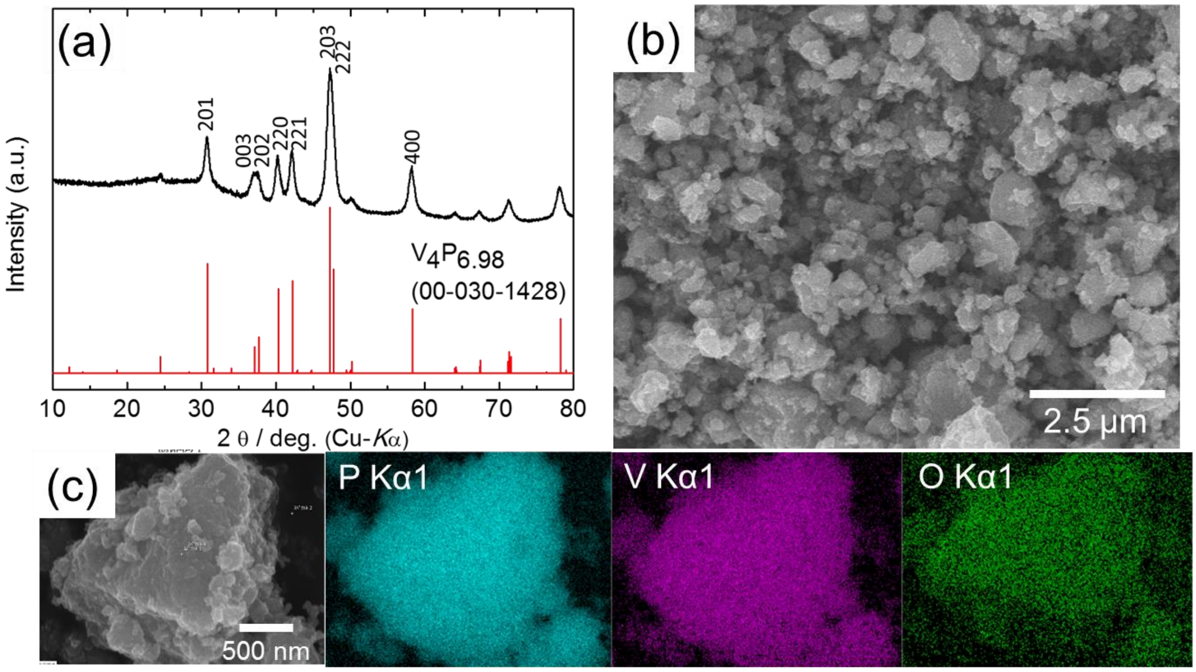

Figure 5-2 (a) XRD pattern, (b) SEM image, and (c) EDX mappings of V_4P_7/5P particles.

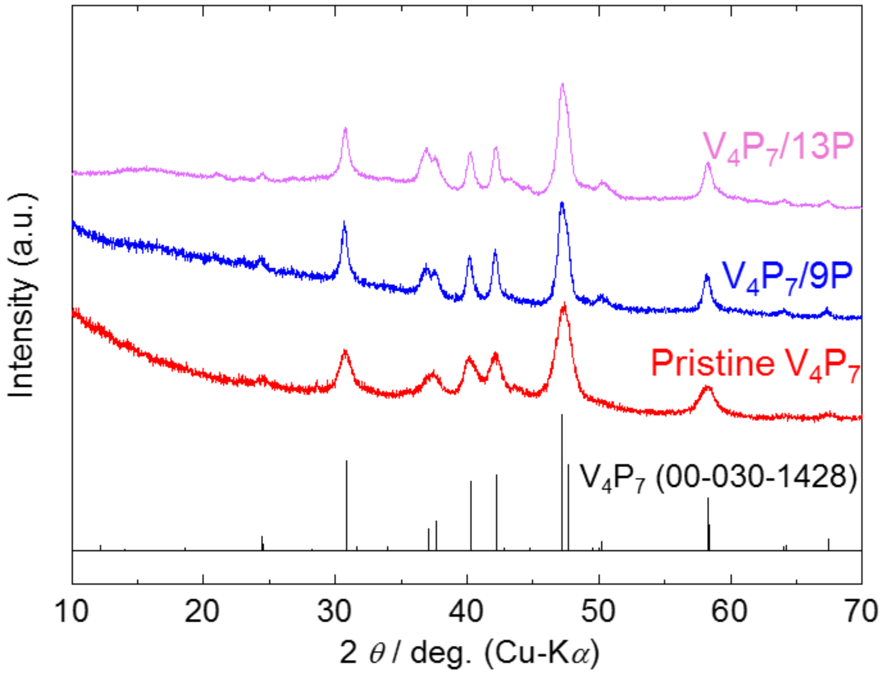

Figure 5-3 XRD patterns of the pristine V_4P_7, V_4P_7/9P, and V_4P_7/13P.

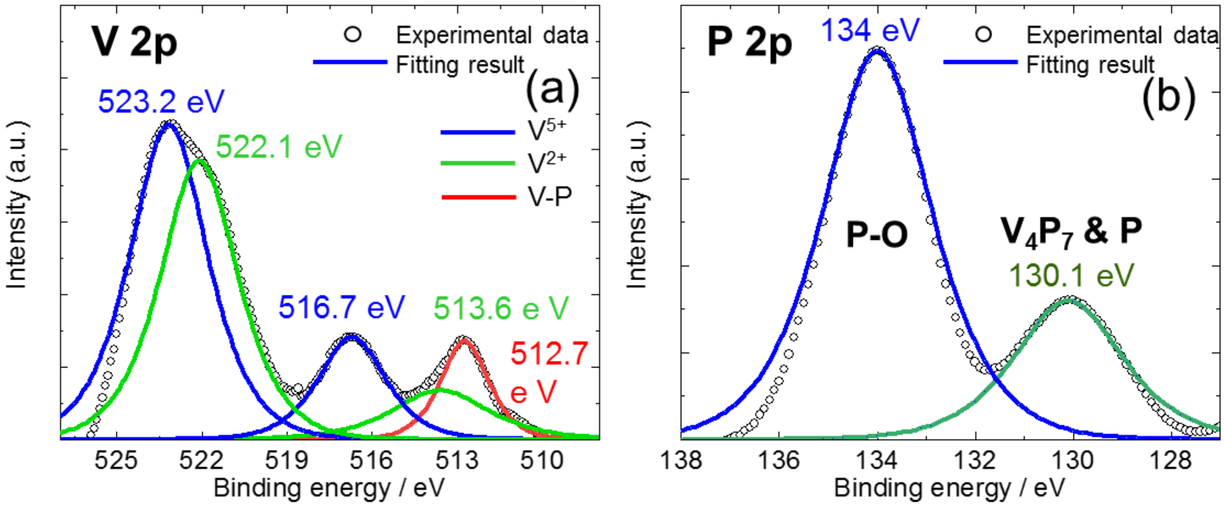

Figure 5-4 XPS spectra with fitting results for (a) V2p and (b) P2p regions of the pristine V_4P_7/5P.

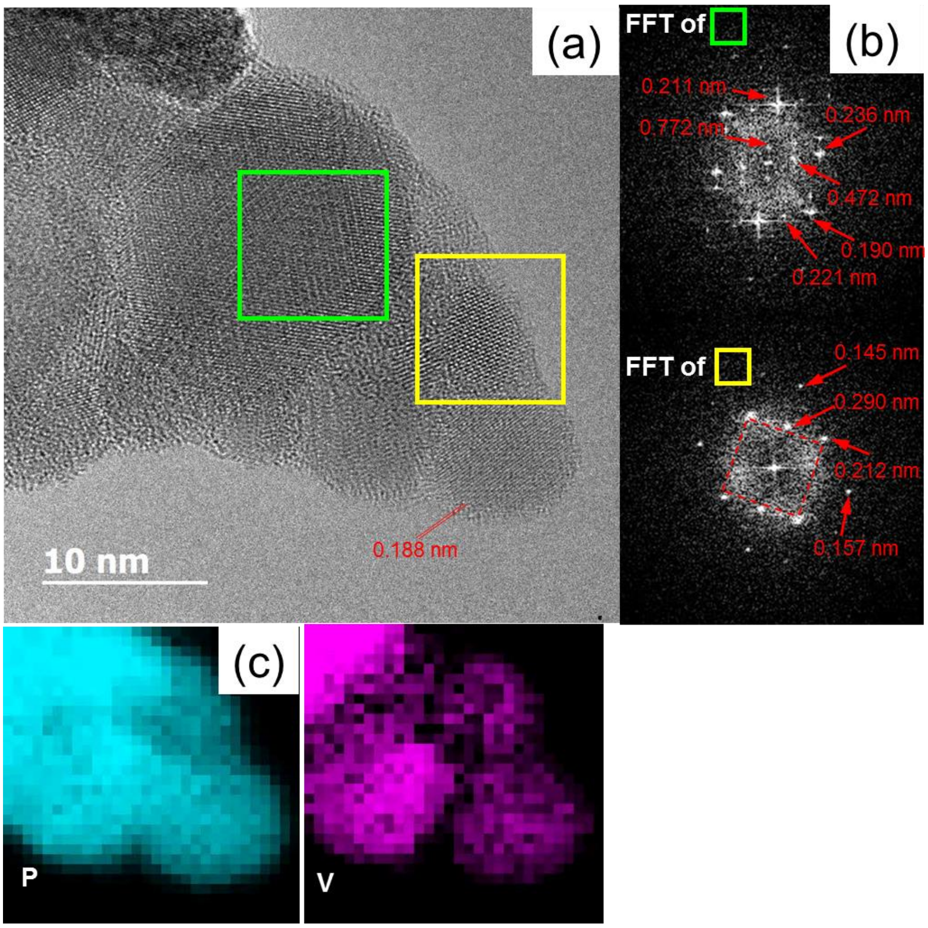

Figure 5-5 (a) HRTEM image of the V_4P_7/5P particles, (b) FFT of the particles in the two areas marked in (a), and (c) elemental mappings of the particles.

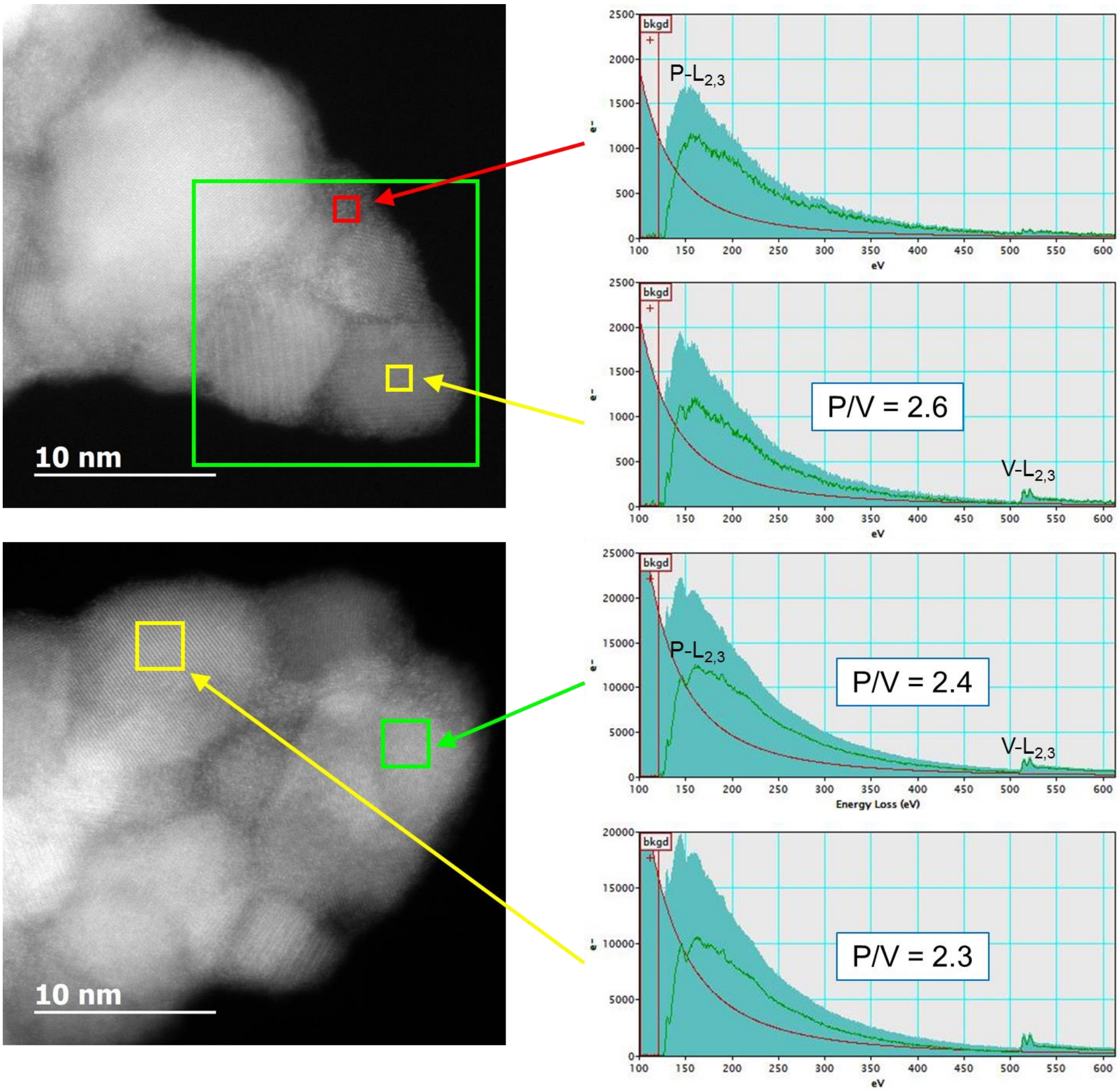

Figure 5-6 STEM images (left hand side) and EELS (right hand side) of V_4P_7/5P.

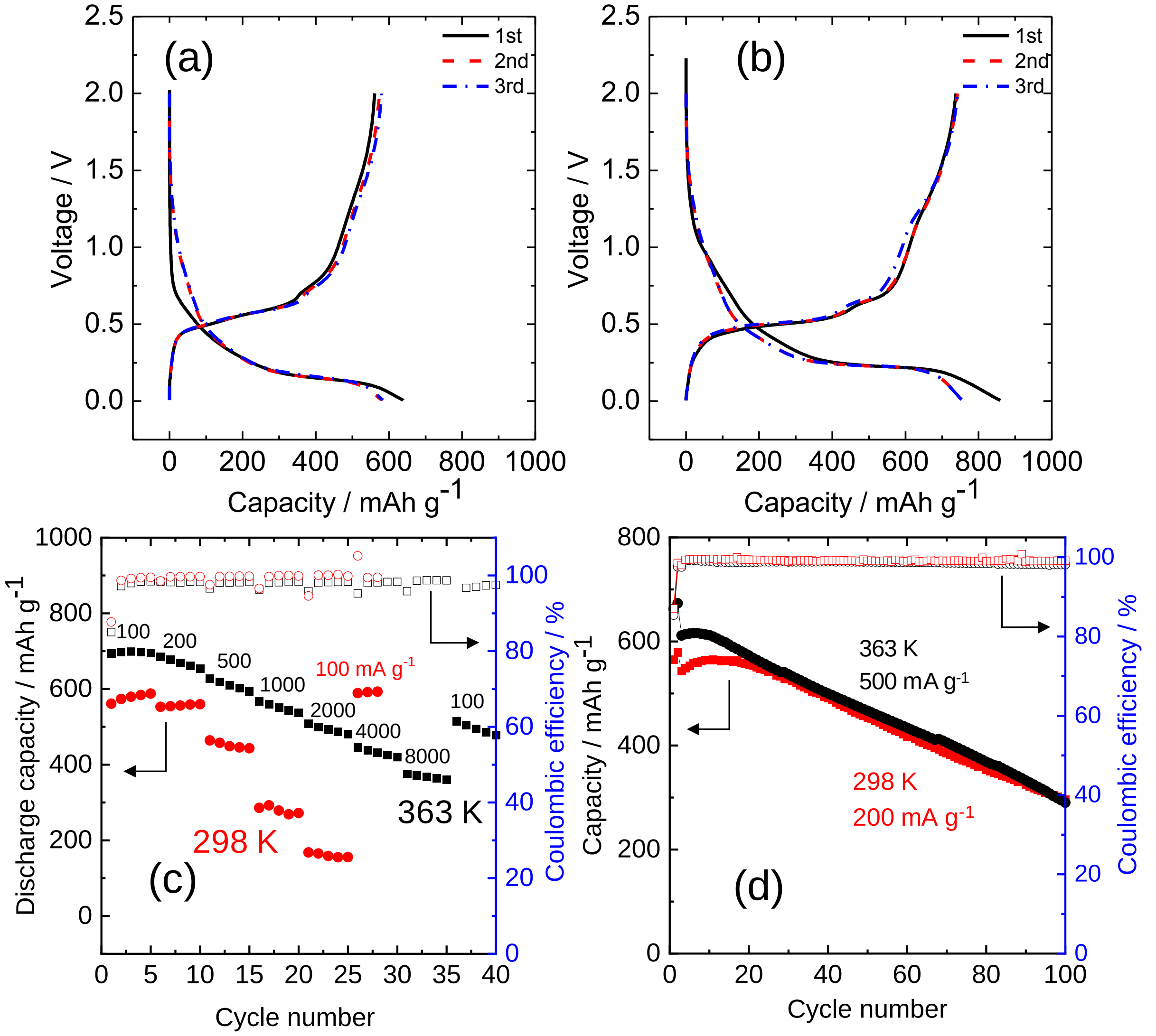

Figure 5-7 Galvanostatic charge–discharge curves of the $V_4P_7/5P$ composite electrode in IL electrolyte (half-cell configuration) at (a) 25 °C and (b) 90 °C (rate: 100 mA g^{-1}, voltage range: 0.005–2.0 V), (c) rate capability at 25 °C and 90 °C (rate: 100−8000 mA g^{-1}), and (d) cyclability at 25 °C (rate: 200 mA g^{-1}) and 90 °C (rate: 500 mA g^{-1}) for the first two cycles at 100 mA g^{-1}.

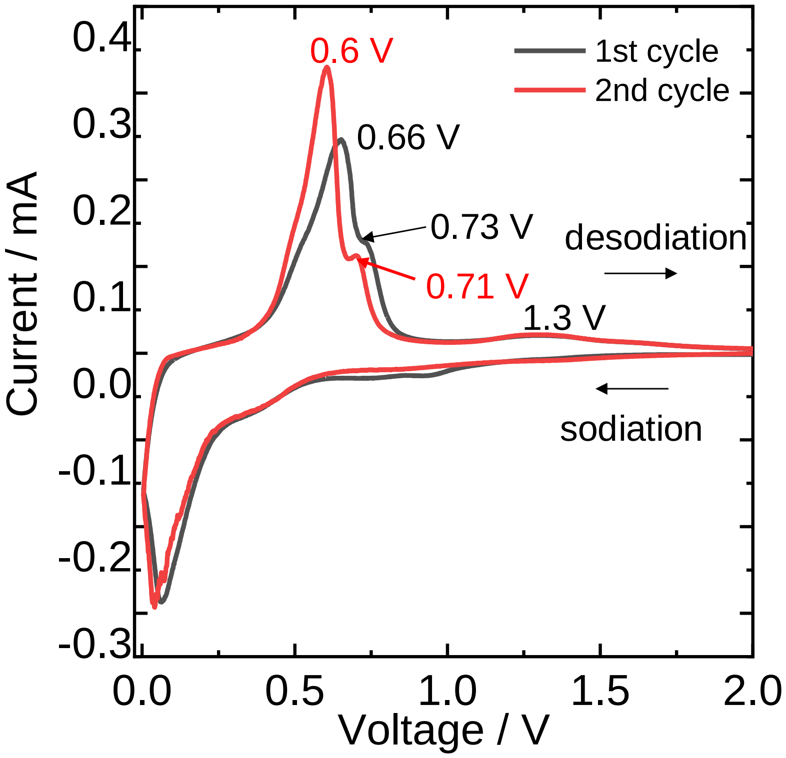

Figure 5-8 Cyclic voltammetry curves of the V_4P_7/5P electrode in the IL electrolyte at 90 °C for first two cycles at a scan rate of 0.05 mV s^{-1}.

Comments of Figure 5-8:

During the first cathodic scan, a very small amount of irreversible electrolyte decomposition from 1.0 to 0.52 V and a broad peak corresponding to the sodium ion insertion at the low voltage can be observed. In the anodic scan, the peaks at 0.66, 0.73 and 1.3 V correspond to the stepwise desodiation of Na_3P. In the second cycle, the cathodic scan overlaps the first cycle but the two anodic peak potentials decrease to 0.6 and 0.71 V, which indicates polarization less than that in the first cycle.

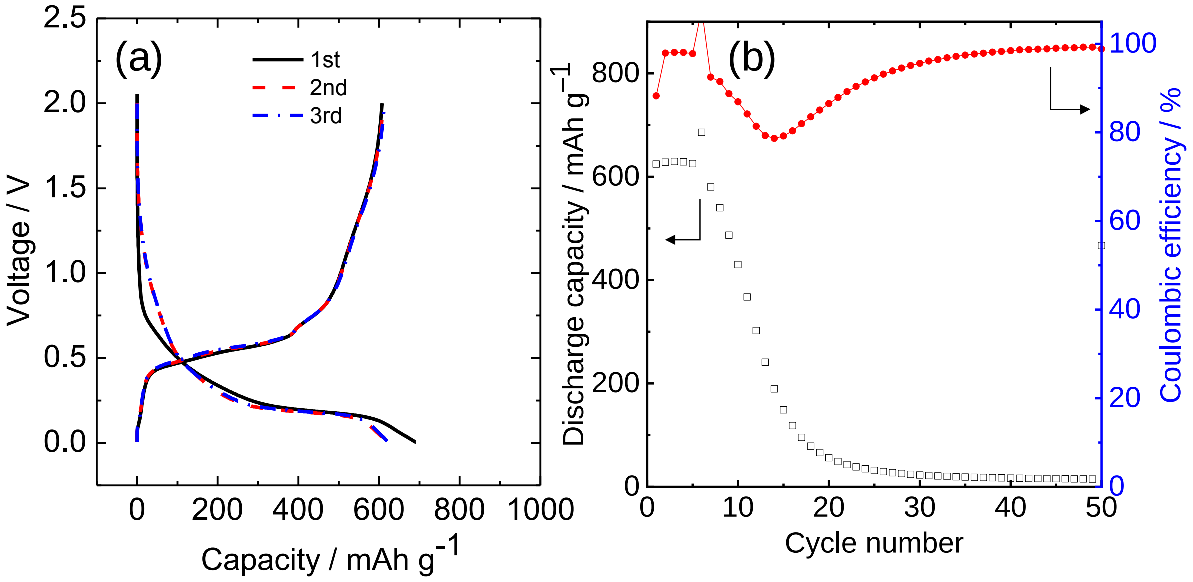

Figure 5-9 (a) Galvanostatic charge-discharge curves of the V_4P_7/5P electrode at 25 °C using 1 mol dm^{-3} $NaPF_6$ in EC:DEC (1:1 v/v) (rate: 100 mA g^{-1}, cut-off voltage: 0.005–2.0 V), (b) cycle test (rate: 100 mA g^{-1}, cut-off voltage: 0.005–2.0 V). The sudden increase in discharge capacity in Figure 5-9 (b) may be caused by formation of unstable solid-electrolyte interphase.

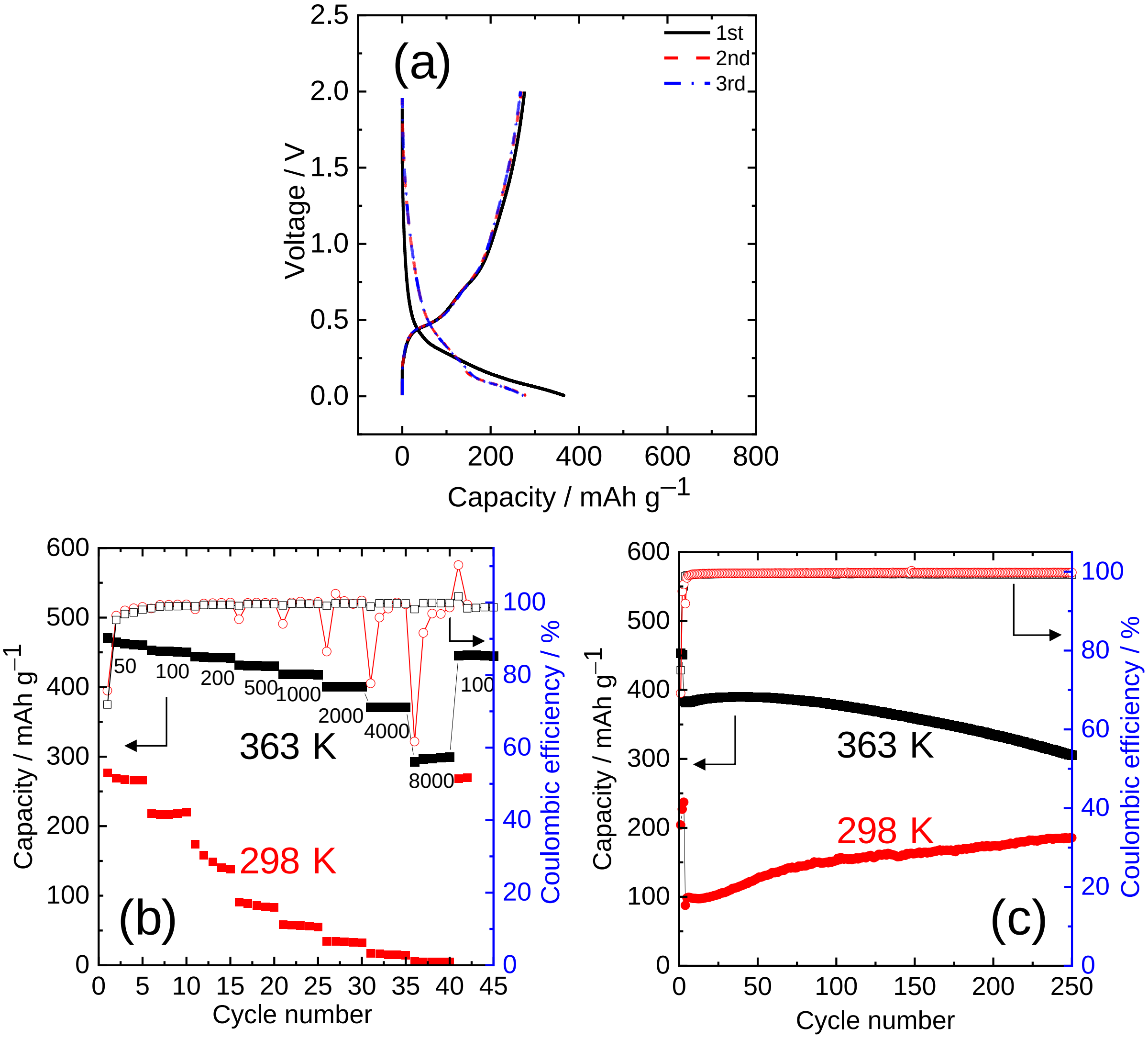

Figure 5-10 Galvanostatic charge–discharge curves of the V_4P_7 composite electrode in the IL electrolyte (half-cell configuration) at (a) 25 °C (rate: 100 mA g^{-1}, voltage range: 0.005–2.0 V), (b) rate capability at 25 °C and 90 °C (rate: 100−8000 mA g^{-1}), and (c) cyclability at 25 °C and 90 °C (rate: 500 mA g^{-1}) for the first two cycles at 100 mA g^{-1}.

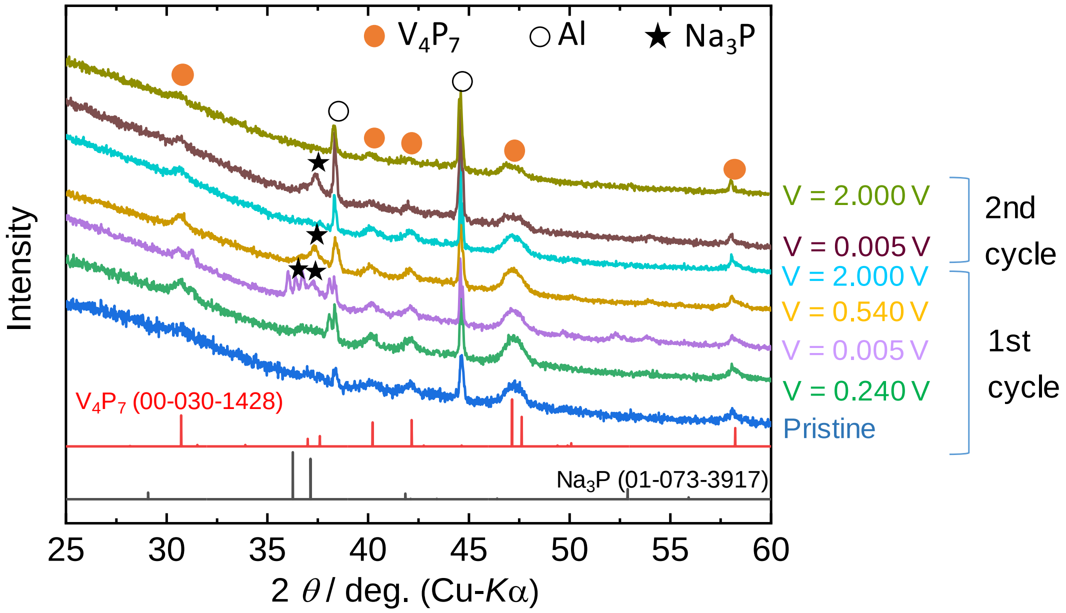

Figure 5-11 *Ex-situ* XRD patterns of the V_4P_7/5P composite obtained with IL electrolyte for the first cycle (charging: pristine, 0.24 V, 0.005 V and discharging: 0.54 V and 2.0 V) and second cycle (0.005 V and 2.0 V).

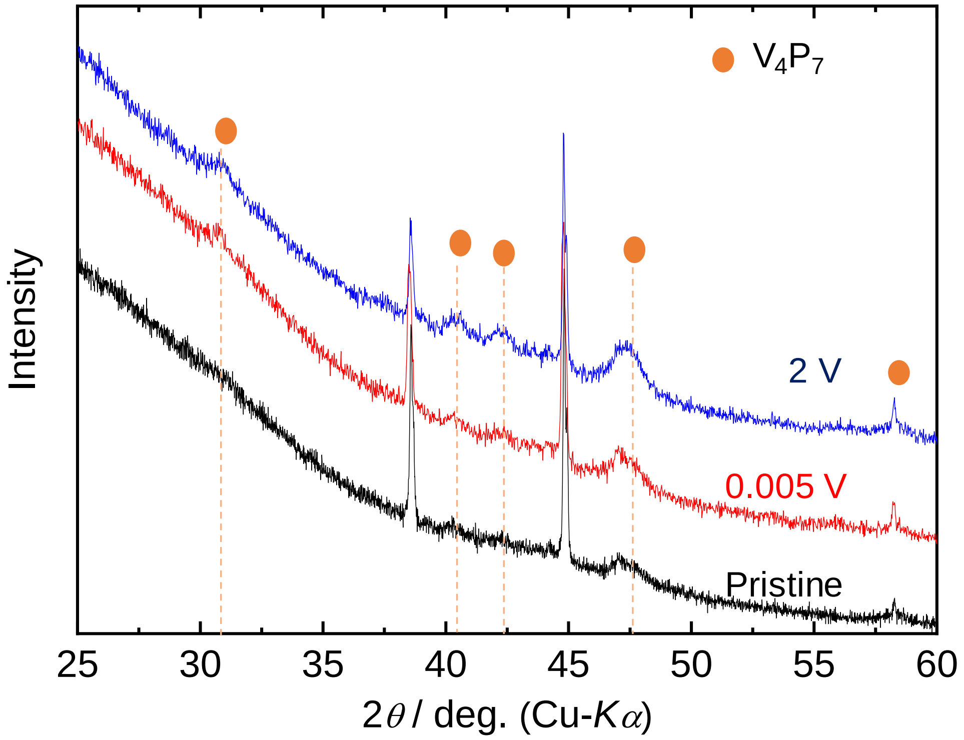

Figure 5-12 *Ex-situ* XRD patterns of the V_4P_7 electrodes in the pristine state, and after first charge and discharge in the IL electrolyte (charging: 0.005 V and discharging: 2.0 V).

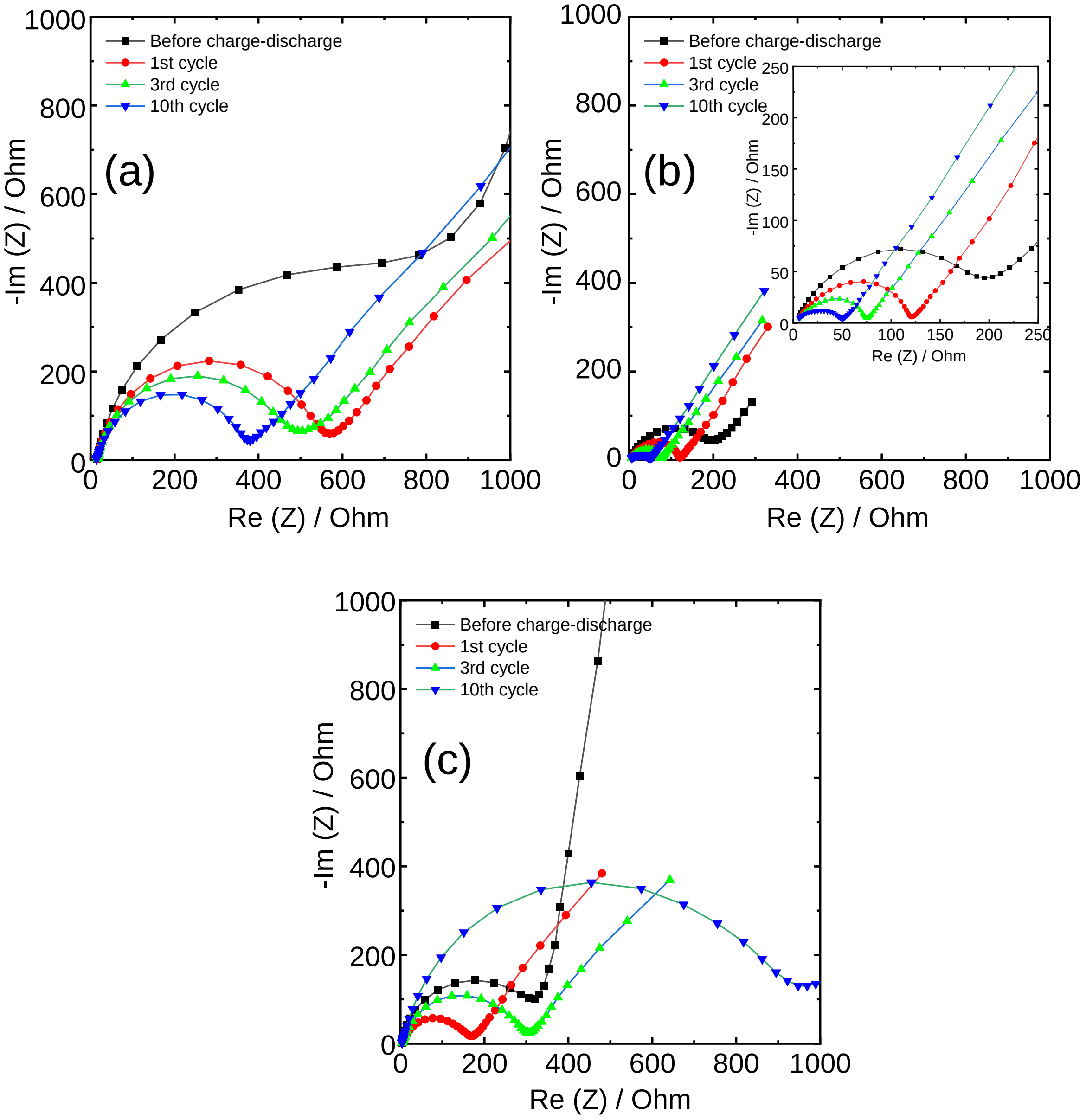

Figure 5-13 Nyquist plots of the V_4P_7/5P electrode (half cell configuration) using (a) IL electrolyte at 25 °C, (b) IL electrolyte at 90 °C (inset is the magnified image) and (c) 1 mol dm^{-3} $NaPF_6$ in EC:DEC (1:1 v/v) at 25 °C (charging-discharging conditions: rate = 100 mA g^{-1}, cut-off voltage = 0.005–2.0 V). The V_4P_7/5P electrode was charged and discharged for one, three, and ten cycles, and then charged to 0.5 V during the next charging step. Impedance spectra were measured at the constant voltage of 0.5 V with an amplitude of 20 mV and frequency range of 100 kHz−10 mHz.

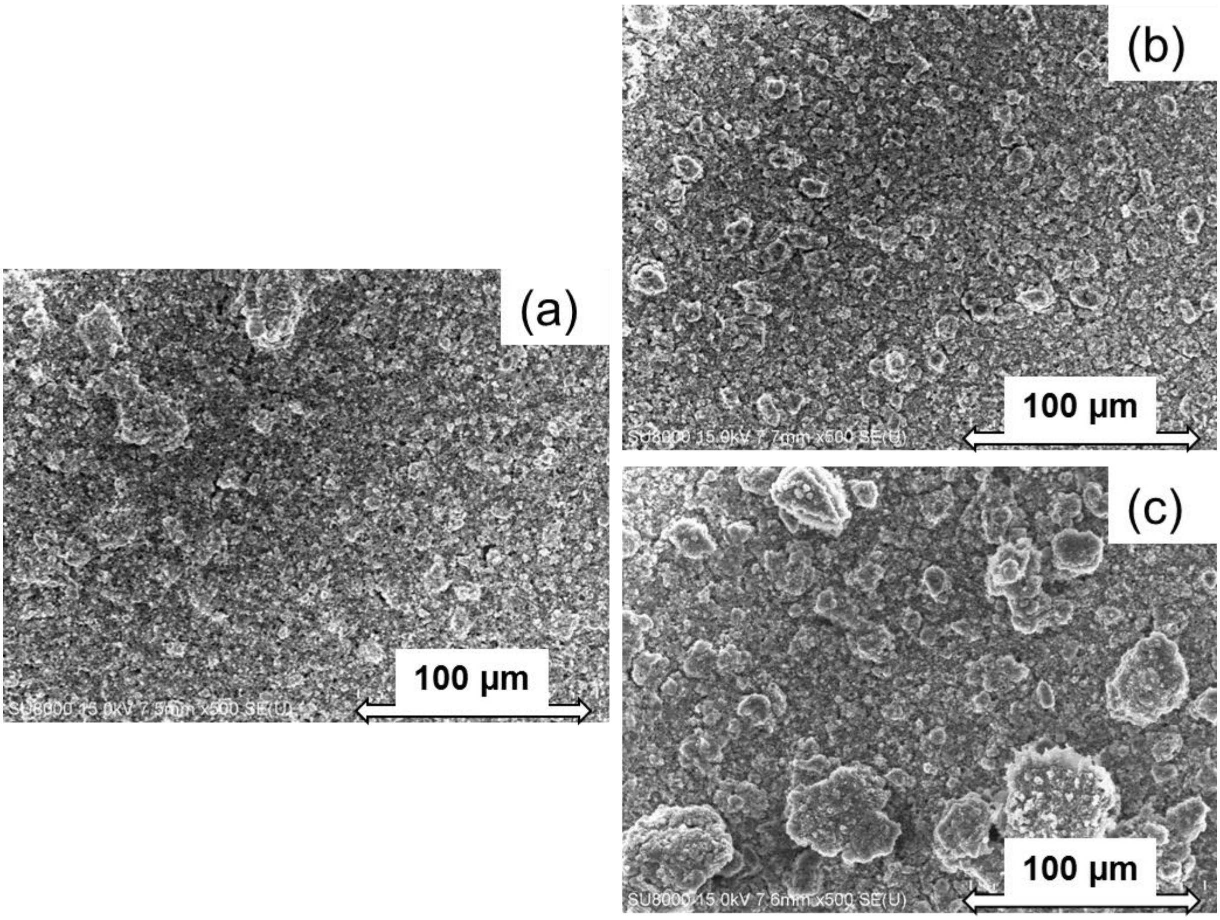

Figure 5-14 SEM images of the V_4P_7/5P electrode (a) in the pristine state, (b) after 10 charge-discharge cycles in the IL electrolyte, and (c) after 10 charge-discharge cycles in the 1 mol dm^{-3} $NaPF_6$ in EC:DEC (1:1 v/v) organic electrolyte.

References

[1] J. Ni, L. Li, J. Lu, ACS Energy Lett., 3 (2018) 1137-1144.

[2] Q. Xia, W. Li, Z. Miao, S. Chou, H. Liu, Nano Res., 10 (2017) 4055-4081.

[3] M. Fan, Y. Chen, Y. Xie, T. Yang, X. Shen, N. Xu, H. Yu, C. Yan, Adv. Funct. Mater., 26 (2016) 5019-5027.

[4] W. Zhang, M. Dahbi, S. Amagasa, Y. Yamada, S. Komaba, Electrochem. Commun., 69 (2016) 11-14.

[5] Y. Kim, Y. Kim, A. Choi, S. Woo, D. Mok, N.-S. Choi, Y.S. Jung, J.H. Ryu, S.M. Oh, K.T. Lee, Adv. Mater., 26 (2014) 4139-4144.

[6] S.-O. Kim, A. Manthiram, Chem. Mater., 28 (2016) 5935-5942.

[7] C.-M. Park, Y.-U. Kim, H.-J. Sohn, Chem. Mater., 21 (2009) 5566-5568.

[8] K.-H. Kim, C.-H. Jung, W.-S. Kim, S.-H. Hong, J. Power Sources, 400 (2018) 204-211.

[9] F. Gillot, M. Ménétrier, E. Bekaert, L. Dupont, M. Morcrette, L. Monconduit, J.M. Tarascon, J. Power Sources, 172 (2007) 877-885.

[10] K.-H. Kim, J. Choi, S.-H. Hong, Chem. Commun., 55 (2019) 3207-3210.

[11] W. Jeitschko, P.C. Donohue, V. Johnson, Acta Crystallogr. Sect. B, 32 (1976) 1499-1505.

[12] D.R. MacFarlane, N. Tachikawa, M. Forsyth, J.M. Pringle, P.C. Howlett, G.D. Elliott, J.H. Davis, M. Watanabe, P. Simon, C.A. Angell, Energy Environ. Sci., 7 (2014) 232-250.

[13] J. Hwang, K. Matsumoto, Y. Orikasa, M. Katayama, Y. Inada, T. Nohira, R. Hagiwara, J. Power Sources, 377 (2018) 80-86.

[14] C. Ding, T. Nohira, R. Hagiwara, J. Power Sources, 388 (2018) 19-24.

[15] Y. Domi, H. Usui, K. Yamaguchi, S. Yodoya, H. Sakaguchi, ACS Appl. Mater. Interfaces, 11 (2019) 2950-2960.

[16] M. Hilder, P.C. Howlett, D. Saurel, H. Anne, M. Casas-Cabanas, M. Armand, T. Rojo, D.R. MacFarlane, M. Forsyth, J. Power Sources, 406 (2018) 70-80.

[17] J. Hwang, K. Matsumoto, R. Hagiwara, Adv. Sustainable Syst., 2 (2018) 1700171.

[18] J. Hwang, K. Matsumoto, R. Hagiwara, J. Phys. Chem. C, 122 (2018) 26857-26864.

[19] H. Usui, Y. Domi, R. Yamagami, H. Sakaguchi, Green Energy Environ., 4 (2019) 121-126.

[20] M. Dahbi, M. Fukunishi, T. Horiba, N. Yabuuchi, S. Yasuno, S. Komaba, J. Power Sources, 363 (2017) 404-412.

[21] K. Matsumoto, Y. Okamoto, T. Nohira, R. Hagiwara, J. Phys. Chem. C, 119 (2015) 7648-7655.

[22] M. Forsyth, H. Yoon, F. Chen, H. Zhu, D.R. MacFarlane, M. Armand, P.C. Howlett, J. Phys. Chem. C, 120 (2016) 4276-4286.

[23] C.E. Myers, H.F. Franzen, J.W. Anderegg, Inorg. Chem., 24 (1985) 1822-1824.

[24] Z. Zhao, T. Yu, S. Zhang, H. Xu, G. Yang, Y. Liu, J. Mater. Chem. A, 7 (2019) 405-411.

[25] M.E. Schlesinger, Chem. Rev., 102 (2002) 4267-4302.

[26] S. Sim, J. Cho, J. Electrochem. Soc. 159 (2012) A669–A672.

[27] S. Boyanov, J. Bernardi, F. Gillot, L. Dupont, M. Womes, J.-M. Tarascon, L. Monconduit, M.-L. Doublet, Chem. Mater. 18 (2006) 3531–3538.

[28] W-J. Li, S-L. Chou, J-Z. Wang, H-K. Liu, S-X. Dou, Chem. Commun. 51 (2015) 3682–3685.

[29] D. Yang, J. Zhu, X. Rui, H. Tan, R. Cai, H. E. Hoster, D. Y. W. Yu, H. H. Hng, Q. Yan, ACS Appl. Mater. Interfaces, 5 (2013) 1093−1099.

[30] W-J. Li, Q-R. Yang, S-L. Chou, J-Z. Wang, H-K. Liu, J. Power Sources, 294 (2015) 627−632.

[31] J. Fullenwarth, A. Darwiche, A. Soares, B. Donnadieu, L. Monconduit, J. Mater. Chem. A, 2 (2014) 2050–2059.

[32] M-P. Bichat, J-L. Pascal, F. Gillot, F. Favier, Chem. Mater. 17 (2005) 6761–6771.

[33] S.-O. Kim, A. Manthiram, ACS Appl. Mater. Interfaces 9 (2017) 16221–16227.

[34] X. Li, W. Lia, J. Yu, H. Zhang, Z. Shi, Z. Guo, J. Alloys Compd. 724 (2017) 932–939.

[35] S.A. Shchukarev, M.P. Motozawa, M-S. Li, J. Gen. Chem. USSR, 29 (1959) 2427–2465.

[36] F. R. De Boer, R. Boom, W. C. M. Mattens, A. R. Miedema, A. K. Niessen, Cohesion in Metals: Transition Metal Alloys, North-Holland: Amsterdam, 1989.

[37] I. Barin, F. Sauert, E. Schultze-Rhonhof, W. S. Sheng, Thermochemical Data of Pure Substances (Part II), VCH: New York (1989) 1104–1107.

Chapter 6

Performance and Charge-discharge Mechanism of Vanadium Diphosphide Negative Electrode

6.1 Introduction

Negative electrode materials showing an insertion-based mechanism in NIBs usually show a lower volume change during sodiation/desodiation than in alloying or conversion based materials, being suitable candidates for applications requiring long cycle life [1]. Hard carbons (HCs) and Ti-based compounds are some of the common insertion-based materials investigated as negative electrode for NIBs. The electrochemical behavior and performance are already discussed in details in Chapter 1. HCs display good cycleability and rate capabilities but the danger related to the Na metal deposition due to the sodiation potential close to 0 V vs Na^+/Na have raised concerns over its application. On the other hand, Ti-based compounds such as sodium titanium phosphates ($NaTi_2(PO_4)_3$) show a high redox voltage (1.7 V vs Na^+/Na) which limits the energy density of NIBs [2]. Additionally, sodium titanates ($Na_2Ti_6O_{13}$ [3] and $Na_4Ti_5O_{12}$ [4]) show only a limited capacity below 50 mA h g^{-1}.

Metal phosphides have emerged as a promising class of materials for secondary batteries showing high theoretical gravimetric and volumetric specific capacities [5-7]. Vanadium phosphides (V_xP_y) are known to their diverse electrochemistry in secondary batteries [8-10]. For instance, V_4P_7 prepared by HEBM shows topotactic insertion of Na^+ and Li^+ for NIBs [11] and LIBs [12], respectively. In the previous chapter, V_4P_7 and its phosphorus composite V_4P_7/5P provided high capacity, good cycleability, and high rate capability using an IL electrolyte. Vanadium diphosphide (VP_2) materials prepared by HEBM and solid state annealing were investigated for LIBs and showed high discharge capacities of 890 and 640 mA h g^{-1}, respectively [10]. From XRD analysis, an amorphous product was observed after lithiation of VP_2 and the redox center at the anion site was proposed because of no change in V *K*-edge spectra in XAFS. A significantly higher discharge capacity of 1290 mA h g^{-1} was observed for VP_4 for LIBs but a conversion/insertion-mixed reaction of VP_4 was observed resulting in the formation of Li_3P and VP and subsequent Li insertion into VP at low voltage [9]. The aforementioned studies suggest that increasing phosphorus content in V_xP_y induces conversion-based mechanism. However, as reported in the case of VP_4, huge volume fluctuation in the conversion reaction results in capacity fading, so the moderate phosphorus content in V_xP_y is considered to exhibit stable cycelability. In spite of intensive investigation in the reported literature, the charge-discharge mechanism of V_xP_y is not yet well-understood. This previous knowledge motivated the author to investigate the unexplored VP_2 negative electrode for NIBs.

The performance of insertion-based materials is also highly dependent on the choice of electrolyte. The SEI components such as Na_2CO_3 formed in conventional electrolytes in NIBs have been observed to be soluble in electrolytes which results in poor cycleability [13]. Additives such as vinylene carbonate and FEC have shown improvements in electrochemical performance by preferentially decomposing and forming a stable film over the electrode surface [14, 15]. However, a contrasting finding was reported in a study investigating HC using 1 mol dm^{-3} $NaClO_4$ in PC with and without FEC. A capacity degradation was observed in the case of addition of FEC, whereas stable capacity retention was obtained without addition of FEC explained by the increase in interfacial resistance caused by FEC addition. This finding was also supported in another study using EC:PC as the electrolyte solvent [16]. In the previous chapters, good electrochemical performance was achieved by employing IL electrolyte. In addition, it ensures a safe operation owing to the low flammability, low volatility and high thermal stability.

In this chapter, the electrochemical performance of vanadium diphosphide (VP_2) is investigated using Na[FSA]–[C_3C_1pyrr][FSA] (20:80 mol ratio) IL for NIBs at 25 and 90 °C. The preparation condition for HEBM was optimized and further characterized by XRD, XPS and TEM. The performance was validated by the measurement with the aid of EIS and SEM along with the cycling. The charge-discharge mechanism is elucidated using *ex-situ* XRD, XPS, and XAFS analysis.

6.2 Experimental

The vanadium (Kojundo Chemical Lab, purity 99.9%) and phosphorus (Wako Pure Chemical Industries, purity 98%) powders were ball-milled (Planetary Micro Mill Pulverisette 7, Fritsch, 20 cm^3 grinding bowl and 3 mm balls made of zirconium oxide) for 20 h at 850 rpm under Ar atmosphere in 1:2 molar ratio to obtain VP_2 powder. The ball-milling parameters were optimized by changing operation time and speed to obtain polycrystalline product.

The negative electrode was prepared by mixing the active material (VP_2), AB conductive additive, and PAI binder in 75:15:10 weight ratios in NMP (Wako Pure Chemical Industries, purity 99%). Another ratio of VP_2:AB:PAI = 90:5:5 was used for a control experiment to elucidate the effects of carbon content on electrochemical behavior. The resulting slurry was subsequently cast on Al foil and dried under vacuum at 90 °C for 10 h in an oven and in an airtight cell connected to a vacuum line at 110 °C overnight. The Na[FSA]-[C_3C_1pyrr][FSA] (20:80 molar ratio) IL was used as an electrolyte. The organic electrolyte 1 M $NaPF_6$ in EC:DEC (1:1 v/v) (Battery grade, Kishida Chemical) was used without any prior treatments. Glass fiber filter (Whatman, GF-A, 260 μm in thickness and 16 mm in diameter) was dried at 110 °C under vacuum and used as a separator, and a Na metal disc (Aldrich, purity

99.9%) was used as a counter electrode. The separator was impregnated with the IL at 80 °C under vacuum overnight prior to use. Coin cells (2032-type) were assembled in the glove box to measure the electrochemical performance without contamination from the air.

Electrochemical behavior of the prepared electrodes (charge-discharge, rate capability, and cycleability tests) were investigated using an HJ1001SD8 charge−discharge test device (Hokuto Denko). All the capacity and current density are described based on the weight of VP_2. The prepared coin cells were kept at an open circuit voltage for more than 3 h prior to the tests. Electrode behavior was analyzed by EIS using a VSP potentiostat (Bio-Logic) at 25 and 90 °C over a frequency range from 100 kHz to 10 mHz with an amplitude of 20 mV. The cells were cycled at the rate of 100 mA g^{-1} for the first three cycles and 500 mA g^{-1} for the subsequent cycles. The EIS spectra were measured at 0.5 V during the charging step of the nth cycle (n = 2, 4, 11, 51, and 101).

The XRD patterns of the pristine and charged/discharged samples were recorded with a Rigaku SmartLab diffractometer (40 kV−30 mA). The samples for *ex-situ* XRD measurement after electrochemical tests were prepared by disassembling the cells followed by rinsing with tetrahydrofuran (Wako Pure Chemical Industries, water content ≤ 10 ppm) and vacuum-drying for one day at room temperature. Particle size and morphology were analyzed by SEM (Hitachi SU-8020). The sample for SEM after 500 cycles was prepared by applying the same procedures as *ex- situ* XRD measurement. Electrode surface was analyzed by XPS using an X-ray photoelectron spectrometer (JEOL, JPS-9010, MgKα, 10 kV−10 mA). For the charged/discharged samples, Ar etching was performed at the ion energy of 600 eV for 30, 60, 90, 120 and 180 s. The TEM samples were prepared in the same manner as that for *ex-situ* XRD measurement, but the powder was scraped off the Al foil after drying. For XAS measurements, the electrodes were charged and discharged to 0.005 and 2.0 V, respectively and scraped off the current collector. The resulting powder was mixed with boron nitride powder to make a pellet

(Active material = 6.7 mg, BN powder = 0.25 g, pelletizing pressure = 60 MPa, 10 mm in diameter) prior to measurements. The XAS data were obtained using the beam line BL-3 at the SRcenter, Ritsumeikan University. The V and P *K*-edge spectra were measured in the transmission mode.

6.3 Results and discussion

The VP_2 sample was prepared by one-step HEBM of vanadium and red phosphorus powder in 1:2 molar ratio at the milling speed of 850 rpm for 20 h using 50:1 (w/w) ball: powder ratio. The HEBM conditions were optimized by varying operation time and speed as shown in Figure 6-1 (a) and (b), respectively. Table 6-1 summarizes ball-milling conditions and the resulting product for V_xP_y compounds including previous works. The ball to powder ratio was maintained at 50:1 (w/w) in the present experiments. The XRD patterns of the products at 400 rpm are assigned to V_4P_7 [17] (space group: $P-4m2$) regardless of the milling time (40, 60, and 80 h) as shown in Figure 6-1 (a), whereas increase of the speed from 600 to 800 rpm induces formation of VP_2 [18] (space group: $C2/m$) with a small amount of VP [19] (space group: $P6_3/mnc$). Further increase of the milling speed to 850 rpm reached nearly pure VP_2 (Figure 6-2).

The VP_2 powder was further characterized by SEM, TEM, EDX, and XPS. According to the SEM analysis, the particle size of the as-prepared VP_2 falls in the range from hundreds of nanometers to a few micrometers (Figure 6-3). Figure 6-4 shows the results of TEM analysis. In the SAED pattern of the pristine VP_2 powder (Figure 6-4(a)), the bright spots in a circular path indicates the polycrystalline nature of the sample, which is also confirmed by the light and dark contrast in HRTEM image (Figure 6-4 (b)). The crystallite size in the HRTEM image ranges from 5 to 20 nm and agrees with 8~20 nm range estimated from the XRD peak by the Scherrer equation (see page 135 for the details on crystallite size estimation). The EDX mapping confirms the uniform distribution of P and V elements over the particle (Figure 6-4 (c)). The lattice fringes of VP_2 are clearly visible in the magnified HRTEM (Figure 6-4 (d)). The use of fast Fourier transform (FFT) power spectrum is an powerful tool to calculate the *d*-spacing from a HRTEM image with clear lattice fringes [20]. The FFT power spectrum obtained from the HRTEM image of VP_2 (Figure 6-4 (d)) provides the *d*-spacings of 0.25 and 0.19 nm which are indexed as the strongest and second strongest diffraction peaks of VP_2 in XRD (indices of 111 and 310, respectively). The XPS spectra of the pristine VP_2 powder are shown in Figure 6-5. In the P2p region, two broad peaks observed at 128.8 and 133.4 eV are assigned to V−P bond in VP_2 [18] and P−O bond [21] on the sample surface owing to the oxidation of phosphorus during ball-milling, respectively (Figure 6-5 (a)). Similarly, V2p region (Figure 6-5 (b)) also shows a strong V-P bond peak at 512.4 eV [22] and weak peaks of VO_x [23] peaks at the higher binding energies. Similar XPS spectra of V2p and P2p was observed in the case of V_4P_7 reported earlier [11]. The aforementioned results indicate successful preparation of polycrystalline VP_2 with oxides of P and V at the surface.

Figure 6-6 shows the electrochemical performance of VP_2 using the Na[FSA]–[C_3C_1pyrr][FSA] (20 : 80 in mol) IL at 25 and 90 °C. The electrode was prepared in the ratio of VP_2:AB:PAI = 75:15:10 in wt%. Figure 6-6 (a) and (b) shows the charge-discharge curves of VP_2 for the first three cycles at 25 and 90 °C, respectively, at a current rate of 100 mA g^{-1} in the voltage range of 0.005–2.0 V. For the initial cycle, a limited discharge capacity of 49 mA h g^{-1} was observed at 25 °C with a Coulombic efficiency of only 37%, whereas the discharge capacity increased considerably to 243 mA h g^{-1} at 90 °C, with an improved Coulombic efficiency of 53%. The following second and third cycles exhibited high reversibility at both the temperatures. The rate capability was measured at 90 °C by varying the current density from 100 to 8000 mA g^{-1} (five cycles per each current density). This material provided a stable capacity at each current rate, showing discharge capacities of 241, 212, and 131 mA h g^{-1} at

100, 1000, and 8000 mA g^{-1} (Figure 6-6 (c)), respectively, with quick recovery of capacity at a low rate after the test at 8000 mA g^{-1}. Figure 6-6 (d) represents the charge-discharge curves of the VP_2 electrode in the last cycle of each current density. The slope and polarization of the discharge curve becomes larger with increasing current density. Figure 6-6 (e) shows the cycle performance of the VP_2 electrode at 500 mA g^{-1} (first three cycles at 100 mA g^{-1} for activation) for 500 cycles at 25 and 90 °C. A high capacity retention of 102.4% was attained with a Coulombic efficiency of 99.92% at the 500 cycle as compared to the 4th cycle (discharge capacity = 207 mA h g^{-1}) at 90 °C. The slight increase of discharge capacity after cycling can be attributed to the activation process of the electrode after raising the current density from 100 to 500 mA g^{-1}. On the other hand, VP_2 provided a limited capacity at 25 °C (24 mA h g^{-1} at the 500 cycle), though the capacity slightly kept increasing over 500 cycles. These results suggest that the improved performance of VP_2 at 90 °C using the IL electrolyte. It was also found that the amount of AB in the electrode influences the irreversible capacity. A control VP_2 electrode containing less AB (VP_2:AB:PAI = 90:5:5 in wt%) gave a higher Coulombic efficiency (first and second cycle Coulombic efficiency: 67.7% and 95.8% for VP_2:AB:PAI = 90:5:5 and 53.2% and 94.2% for VP_2:AB:PAI = 75:15:10) owing to the less electrolyte decomposition on AB that has a high specific surface area (Figure 6-7 (a) and Figure 6-6 (b)). During cycle tests, however, the discharge capacity of the electrode with less AB monotonously decreases till 500 cycles, providing only 39.2% capacity retention, which suggests that cycelability of the VP_2 electrode deteriorates by decreasing the AB content.

Symmetric cell EIS is a facile method to pursue the electrochemical behavior of an electrode material without being affected by the counter electrode material and has been applied to various battery systems,[24, 25] including NIBs [26]. Figure 6-8 shows the Nyquist plot of a VP_2/VP_2 symmetric cell obtained by EIS at 25, 60 and 90 °C. The Na/IL/VP_2 half cells was charged to 0.5 V to prepare the VP_2 electrode used for the symmetric cell EIS test. The semicircle corresponding to charge transfer resistance (characteristic frequency: 1–200 Hz) and intercept to the horizontal axis corresponding to bulk resistance decreased as the temperature increases as shown in Figure 6-8 (a) and inset (see Table 6-2 for the fitted EIS parameters). The equivalent circuit in the Figure 6-8 (c) is used for fitting the curves in Nyquist plot. This result was further supported by EIS tests of the Na/VP_2 half-cell during 500 cycles at 90 °C (the cycling conditions were the same as those in the case of Figure 6-6 (e)). The impedance spectra were measured at the cell voltage of 0.5 V during the charging step at the 2, 4, 11, 51, 101 and 501th cycles. The Nyquist plots showed one depressed semicircle which is composed of two semicircles at high frequency (R_2~10^4 Hz) and medium frequency (R_3~10^2 Hz) (see Table 6-3, for the fitted EIS parameters). Although the medium frequency component is assigned to charge transfer resistance with no doubt, the high frequency one has been a matter of discussion [26, 27]. As the cycle proceeds, both the resistances R_2 and R_3 decreased consistently, which indicates the decline of overall interfacial resistance with cycling.

To elucidate the effects of electrolyte on electrochemical performance, charge-discharge and cycleability tests were performed with a commonly used 1 mol dm^{-3} $NaPF_6$ in EC:DEC (1:1 v/v) organic electrolyte at 25 °C as shown in Figure 6-9. By comparing the charge-discharge curves with the IL and organic electrolytes at 25 °C (Figures 6-6 (a) and 6-9 (a)), higher charge and discharge capacities of 289 and 148 mA h g^{-1} were observed for organic electrolyte (charge capacity, 134 mA h g^{-1} and discharge capacity, 49 mA h g^{-1} for IL). However, the cycle test at the current rate of 500 mA g^{-1} (first three cycles at 100 mA g^{-1}) at 25 °C (Figure 6-9 (b)) shows a continuous capacity fading providing a mere 17 mA h g^{-1} at the 500th cycle. Further performance validation was attempted by using organic electrolyte without additive due to its improved stability with sodium counter electrode [28]. The electrochemical behavior of VP_2 with 1 mol dm^{-3} $NaPF_6$ in EC:DEC (1:1 v/v) with 3 wt% FEC is shown in Figure 6-9 (c) and (d). A similar charge and discharge capacities of 295 and 141 mA h g^{-1} were observed to that in the absence of additive in the first cycle. Moreover, the cycleability result (Figure 6-9 (d)) also showed significant capacity degradation during 500 cycles. The results above suggest the incompatibility of VP_2 with an organic electrolyte and the importance of intermediate-temperature operation and ionic liquid for harvesting good performance.

The properties of SEI layer formed on the negative electrode significantly influences the overall performance of full cells including initial Coulombic efficiency, rate capability, and cycleability. Surface properties of the SEI layer on the VP_2 electrode after charge-discharge at 90 °C in the IL electrolyte were analyzed by SEM and XPS. Figure 6-10 shows the SEM images of the VP_2 electrode before and after cycling. The SEM image of the pristine state shows even distribution of VP_2 particles with a mean diameter of few micrometers in the composite electrode (Figure 6-10 (a)). On the other hand, the electrode surface after 500 cycles was covered with a uniform and partly porous SEI layer with no visible cracks (Figure 6-10 (b)). This result was confirmed by the XPS depth profile of the VP_2 electrode after the electrochemical test. Figure 6-11 shows the P2p and V2p XPS spectra of the VP_2 electrode which was charged and discharged to 2.0 V and etched by Ar-ion bombardment for 0, 30, 60, and 120 s. Although no signals of P and V are visible at 0 s, merely 30 s-etching results in appearance of all the peaks which are assigned to P−O and V−P, indicating very limited thickness of the SEI layer. Further etching lead to little change in the peak position.

The charge-discharge mechanism of VP_2 was investigated by *ex-situ* XRD, XPS, and XAFS for the sample charge-discharged at 90 °C (current density: 100 mA g^{-1}). Figure 6-12 shows XRD patterns and XPS spectra of the pristine, charged (0.005 V), and discharged (2.0 V) VP_2 electrode. All the diffraction peaks in the XRD patterns are indexed to VP_2 in any state and remained unchanged (Figure 6-12 (a)), suggesting the little change in the VP_2 structural frame during charge-discharge. Furthermore, in P2p XPS spectra of charged and discharged VP_2 electrode (etched for 180 s for SEI removal) the relative peak intensity of V-P bond and P-

O bond remain unperturbed as shown in Figure 6-12 (b). However, a reduction of P-O bond is observed after charging as compared to pristine sample which can be explained by partial removal of surface oxide layer by Ar ion etching. Figure 6-13 shows V and P *K*-edge XANES spectra and Fourier transforms of the EXAFS oscillations for the pristine, charged (0.005 V) and discharged (2.0 V) VP_2 electrode. The V *K*-edge and P *K*-edge XANES spectra show insignificant change after charge and discharge as compared to the pristine state. Moreover, the peaks in the pristine state overlap the ones in charged and discharged states in EXAFS, indicating negligible change in the V-P bond length which confirms the aforementioned results of XRD and XPS. This result is also similar to the case of V_4P_7 reported in the previous study [11]. EDX analysis of the VP_2 electrode after charging and discharging was performed to provide an estimation of Na content in the VP_2 as shown in Figure 6-14. For facile comparison, only the normalized weight percentage of Na, V, and P is mentioned. After charging, 46.7, 22.5 and 30.8 wt% of Na, V, and P were observed, respectively, which corresponds to the Na/V molar ratio of 4.6. After discharging, the weight percentage of Na decreased to 16.7%, which resulted in the Na/V molar ratio to 1.0. The remaining Na can be estimated to be used in the reversible charge and discharge process. In that study, a topotactic insertion-type mechanism was proposed in which 0.95 Na^+ ions were inserted reversibly at 50 mA g^{-1} at 25 °C. In the present case, 1.04 Na^+ ions were inserted reversibly at 100 mA g^{-1} at 90 °C according to the calculations from discharge capacity.

6.4 Conclusions

In this chapter, the electrochemical behavior of VP_2 was investigated using the Na[FSA]–[C_3C_1pyrr][FSA] IL electrolyte. The active material VP_2 was prepared by one-step high energy ball-milling process at 850 rpm for 20 h and characterized by XRD, SEM, TEM and XPS. The charge-discharge test of polycrystalline VP_2 conducted using the IL showed a moderate discharge capacity of 243 mA h g^{-1} at 90 °C in the first cycle, whereas a limited capacity of only 49 mA h g^{-1} was observed at 25 °C with a Coulombic efficiency of 53 and 37%, respectively. At 90 °C, this material showed an excellent capacity retention of 102.4% after 500 cycles and a discharge capacity of 131 mA h g^{-1} at 8000 mA g^{-1}. The systematic study employing EIS of symmetric VP_2/VP_2 cell using IL at 25, 60 and 90 °C revealed that charge transfer resistance was highly suppressed at 90 °C. Ionic conductivity and amount of AB were also identified as the major factors for influencing the first cycle irreversible capacity and discharge capacity revealed by investigating $NaPF_6$ in EC:DEC organic electrolyte at 25 °C and a different composition of electrode 90:5:5 (VP_2:AB:binder) as compared to 75:15:10. A continuous decrease in interfacial resistance with cycling in Na/VP_2 half-cell at 90 °C and formation of a uniform and thin SEI layer observed by SEM and XPS depth profile supported the rate capability and good cycleability results. A possibility of the topotactic insertion-type reaction mechanism was suggested by *ex-situ* XRD, XPS, and XAFS measurements because no structural change was observed after charging and discharging. It is interesting to investigate electrochemical behavior and structural change of VP_2 applied for lithium-ion batteries using the IL electrolyte at intermediate temperature.

Table 6-1 Summary of ball-milling conditions and electrochemical performance of V_xP_y compounds for NIBs and LIBs.

V_xP_y Compound	**Ball-milling conditions**				**Electrochemical performance**	
	Speed (rpm)	**Time (h)**	**Ball: powder ratio (w/w)**	**Crystal system (space group)**	**1st cycle discharge capacity (mA h g^{-1})/ rate (mA g^{-1})**	**Electrolyte**
VP/Li[8]	-	6	20:1	Hexagonal ($P6_3/mnc$)	291/100	1 M $LiPF_6$ in EC/DEC(1:1 v/v)
V_4P_7@C/Li[12]	300	60	20:1	Tetragonal ($P{-}4m2$)	882/100	1 M $LiPF_6$ in EC/DMC(1:1 v/v)
V_4P_7/Na[11]	300	60	20:1	Tetragonal ($P{-}4m2$)	240/50	1 M $NaClO_4$ in EC/DMC(1:1 v/v) with 5 vol% FEC
V_4P_7-5P/Na	400	20	50:1	Tetragonal ($P{-}4m2$)	560/100	Na[FSA]-[C_3C_1pyrr][FSA] (20:80 mol ratio)
VP_2/Li[10]	600	50	10:1	Monoclinic ($C2/m$)	890/100	1 M $LiPF_6$ in EC/DMC(1:1 v/v)
VP_4/Li[9]	-	48	20:1	Monoclinic ($C2/c$)	1290/-	1 M $LiPF_6$ in EC/DEC(1:1 v/v)

Table 6-2 EIS fitting parameters, R_1, R_2, R_3, Q_2, Q_3, a_2 and a_3, corresponding to the Nyquist plot of VP_2/VP_2 symmetric cell shown in Figure 6-8 (a).

Temperature / °C	**Resistance / Ω (Characteristic frequency/ Hz)**			**CPE / F $s^{(a\text{-}1)}$**			
	R_1	**R_2**	**R_3**	**Q_2**	**a_2**	**Q_3**	**a_3**
25	34.71	8.47 (7327)	586.10 (12)	$2.57\text{x} 10^{-6}$	1	$4.34\text{x}10^{-5}$	0.843
60	21.33	1.87 (16997)	167.03 (10)	$5.00\text{x} 10^{-6}$	1	$0.52\text{x}10^{-3}$	0.594
90	11.97	1.85 (17922)	5.00 (178)	$4.80\text{x} 10^{-6}$	1	$3.45\text{x}10^{-3}$	0.578

Table 6-3 EIS fitting parameters, R_1, R_2, R_3, Q_2, Q_3, a_2 and a_3, during charge-discharge cycling for VP_2 in the IL electrolyte at 90 °C (see Figure 6-8 (b) for the spectra).

	Resistance / Ω			**CPE / F s$^{(a\text{-}1)}$**			
Cycle	R_1	R_2	R_3	Q_2	a_2	Q_3	a_3
1	5.06	19.95	13.9	7.05x10^{-6}	0.821	6.74x10^{-5}	0.786
3	3.38	21.14	8.91	7.26x10^{-6}	0.810	9.69x10^{-5}	0.802
10	3.08	3.22	7.72	4.49x10^{-6}	0.936	1.25x10^{-4}	0.605
50	3.38	1.11	7.92	2.82x10^{-5}	0.865	3.84x10^{-5}	0.680
100	7.81	2.19	4.42	1.05x10^{-6}	1.000	1.56x10^{-5}	0.844
500	8.41	0.54	3.56	1.91x10^{-5}	0.825	1.91x10^{-5}	0.999

Scherrer equation

$$d = \frac{K\lambda}{\beta \cos\theta}$$

d = mean size of crystallite

λ = X-ray wavelength (0.15406 nm)

K = dimensionless shape factor taken 0.9 here

β = peak width at half of the maximum intensity, the data in degrees are converted in radians

θ = Bragg angle

Calculation for four different diffraction peaks

Diffraction peak	2 θ / deg.	β / deg.	Machine error / deg.	Crystallite size (L) / nm
−201	21.15	0.44	0.05	20.72
−202	26.89	0.62	0.05	14.33
111	36.89	1.00	0.05	8.82
310	47.08	1.04	0.05	8.75

The range of crystallite size was roughly 8~20 nm.

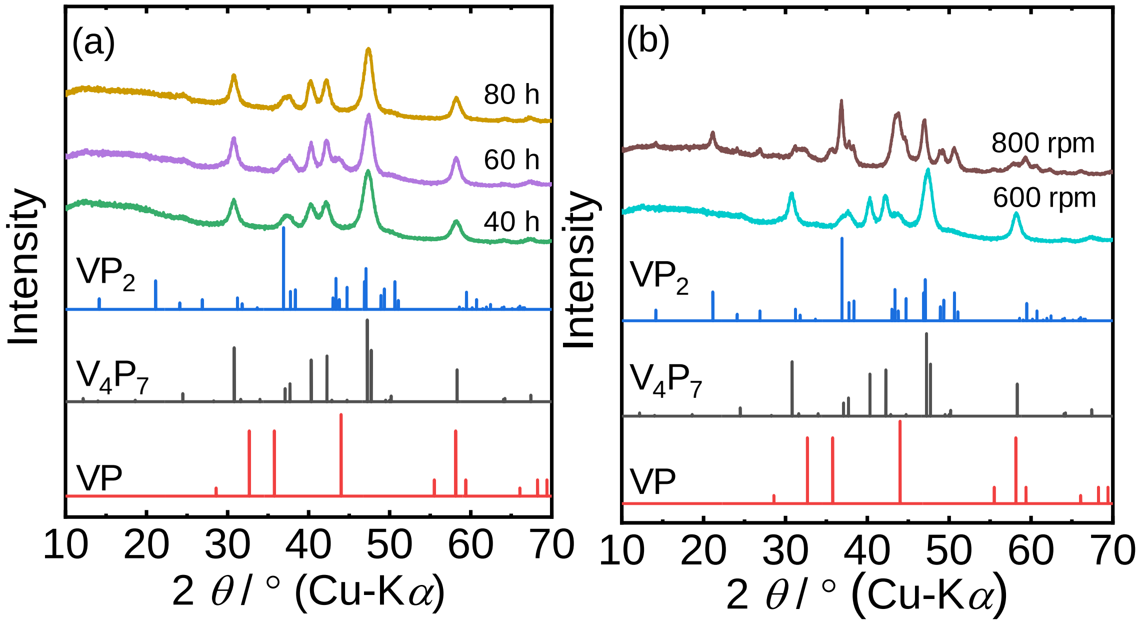

Figure 6-1 XRD patterns of the powder products obtained by HEBM of V and P (V:P = 1:2 in mol). (a) Time dependency (40, 60 and 80 h) at the constant milling-speed of 400 rpm and (b) milling-speed dependency (600 and 800 rpm) in the constant milling-time of 20 h. The ball-to-powder ratio was kept constant at 50:1 in weight for all the experiments. The reference patterns of VP [19], V_4P_7 [17] and VP_2 [18] are shown for comparison.

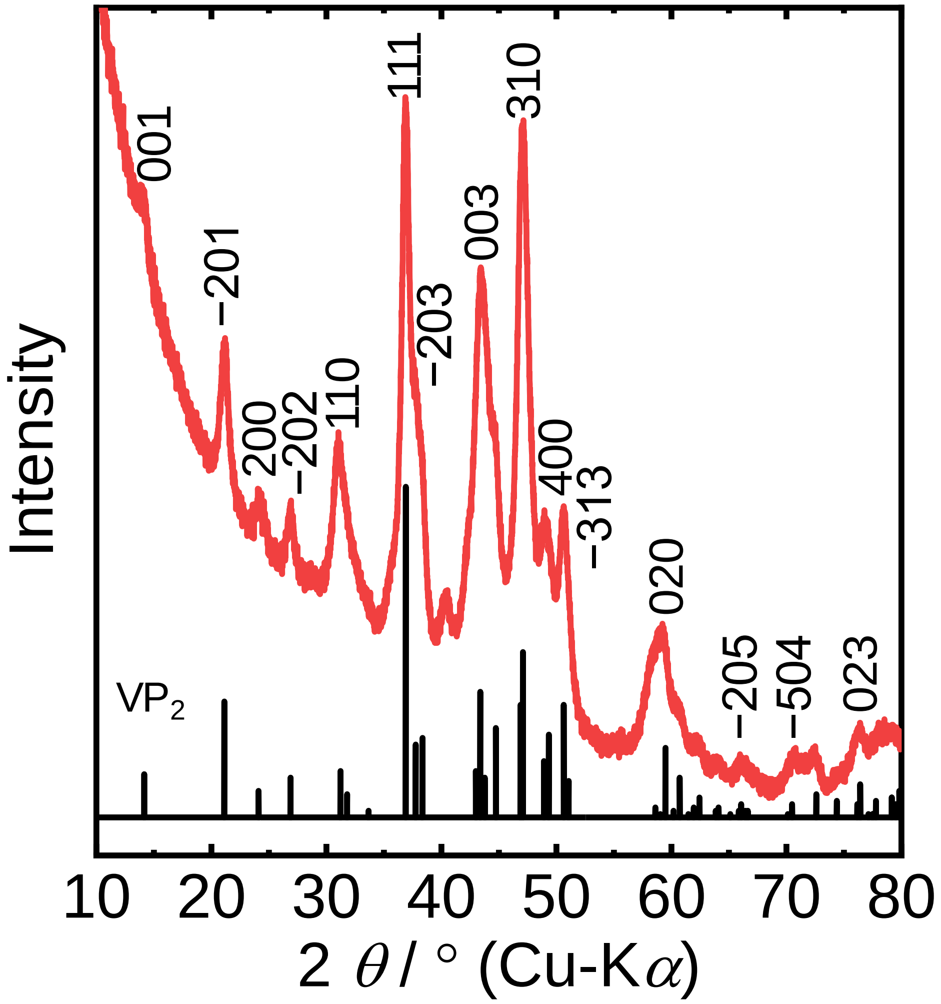

Figure 6-2 The XRD pattern of the pristine VP_2 powder prepared by HEBM. The reference pattern of VP_2 is also shown for comparison [18].

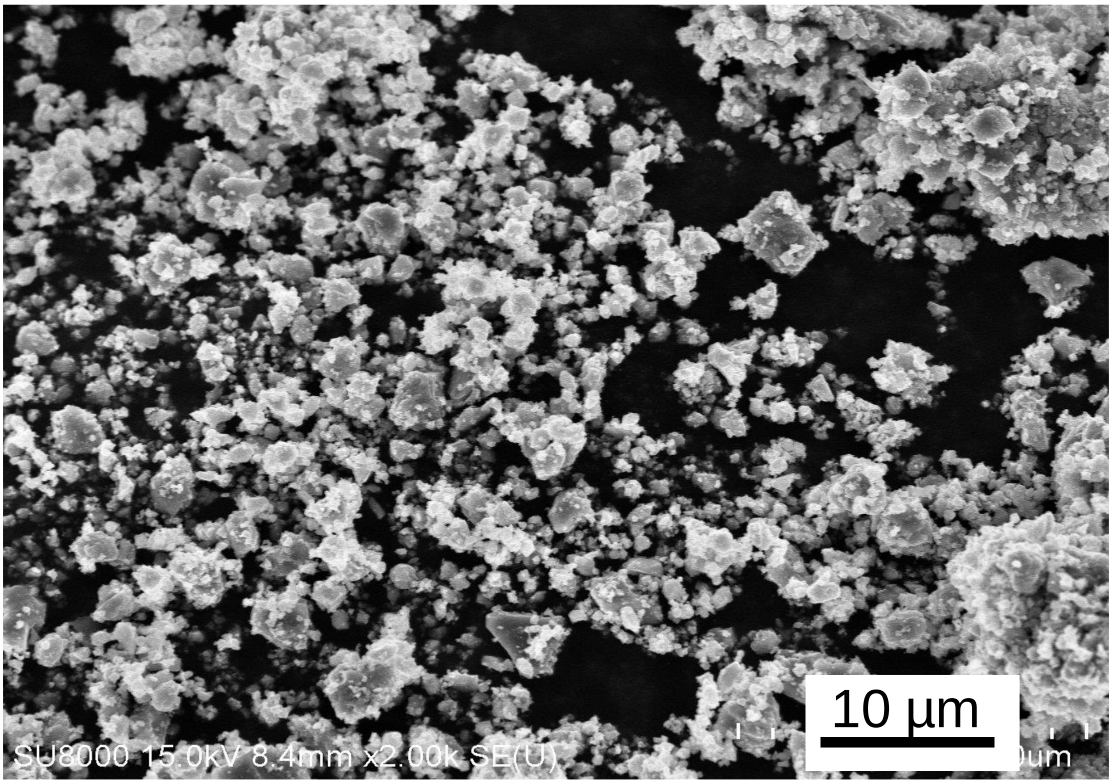

Figure 6-3 SEM image of the pristineVP_2 powder obtained by HEBM of V and P (V:P = 1:2) at 850 rpm for 20 h.

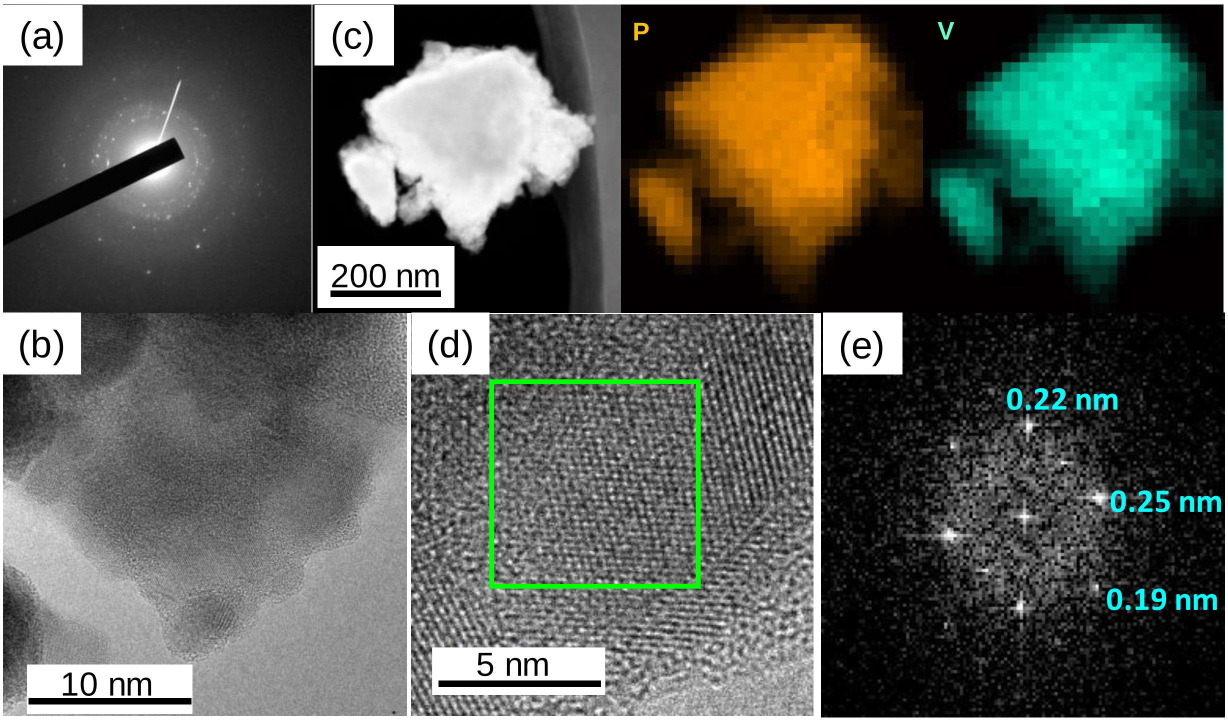

Figure 6-4 (a) SAED pattern, (b) HRTEM image, (c) EDX mapping, (d) magnified HRTEM image, and (e) FFT power spectrum of the pristine VP_2 powder.

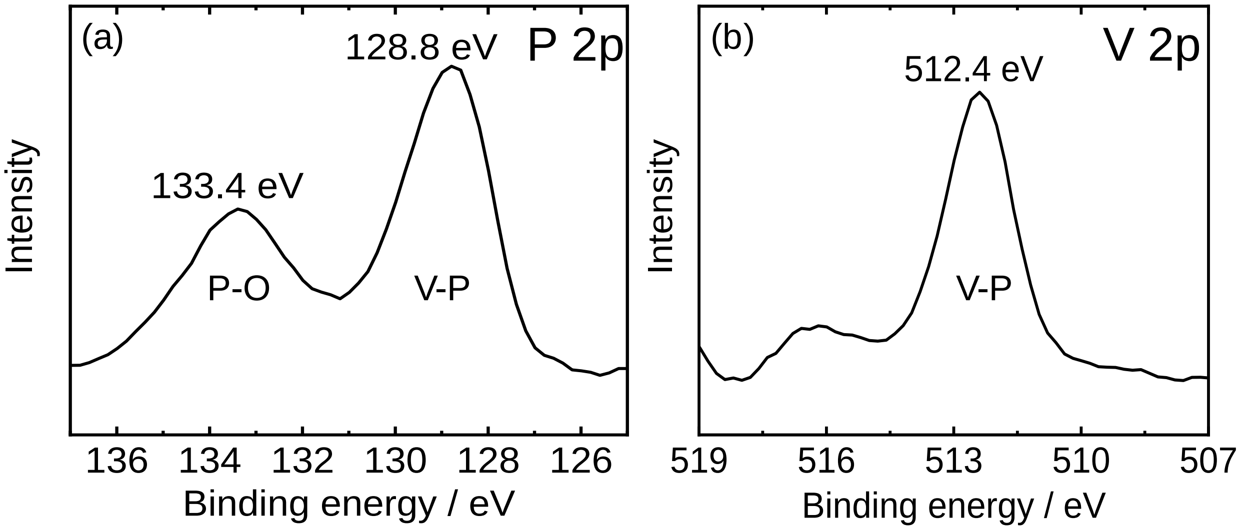

Figure 6-5 XPS spectra of the VP_2 pristine powder in (a) P 2p and (b) V 2p regions.

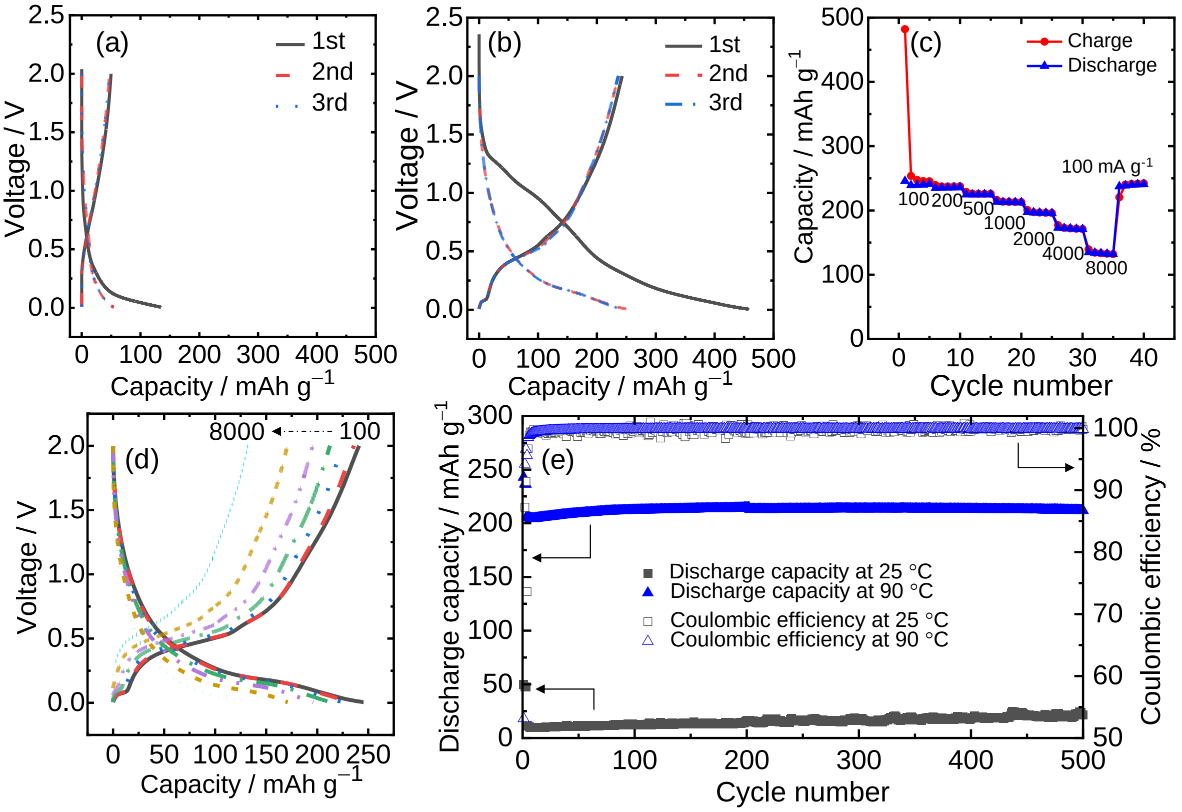

Figure 6-6 Electrochemical behavior of VP$_2$ in a coin-type cell with the IL electrolyte (cut-off voltage: 0.005–2.0 V and counter electrode: Na metal disc). Galvanostatic charge-discharge curves for the first three cycles at (a) 25 and (b) 90 °C (current density: 100 mAg^{-1}). (c) Rate capability at 90 °C (current density: 100–8000 mAg^{-1}) and (d) galvanostatic charge-discharge curves of the last cycle for each rate. (e) Cyclability for 500 cycles at 25 and 90 °C (rate: 100 mAg^{-1} for the first three cycles to activate the electrode and 500 mA g^{-1} for the rest of cycles).

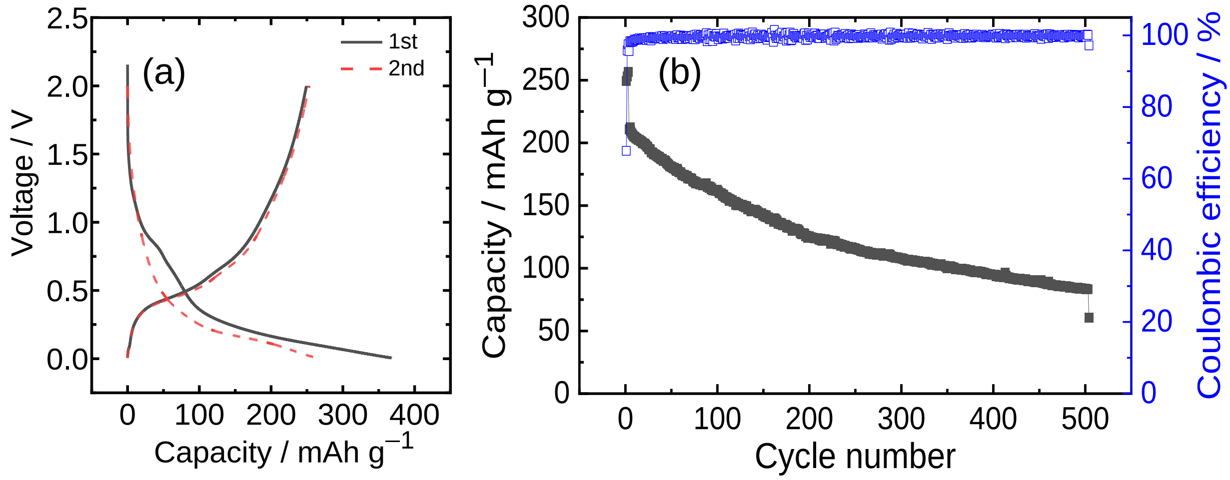

Figure 6-7 Electrochemical behavior of the VP_2 electrode (VP_2:AB:binder = 90:5:5 in wt%) for the first two cycles using the IL electrolyte at 90 °C. (a) Galvanostatic charge-discharge curves (current density: 100 mAg^{-1} and cut-off voltage: 0.005–2.0 V). (b) Cyclability during 500 cycles (rate: 100 mAg^{-1} for the first three cycles to activate the electrode and 500 mA g^{-1} for the rest of cycles). See Figure 6-6 to compare the behavior of the (VP_2:AB:binder = 75:15:10 in wt%).

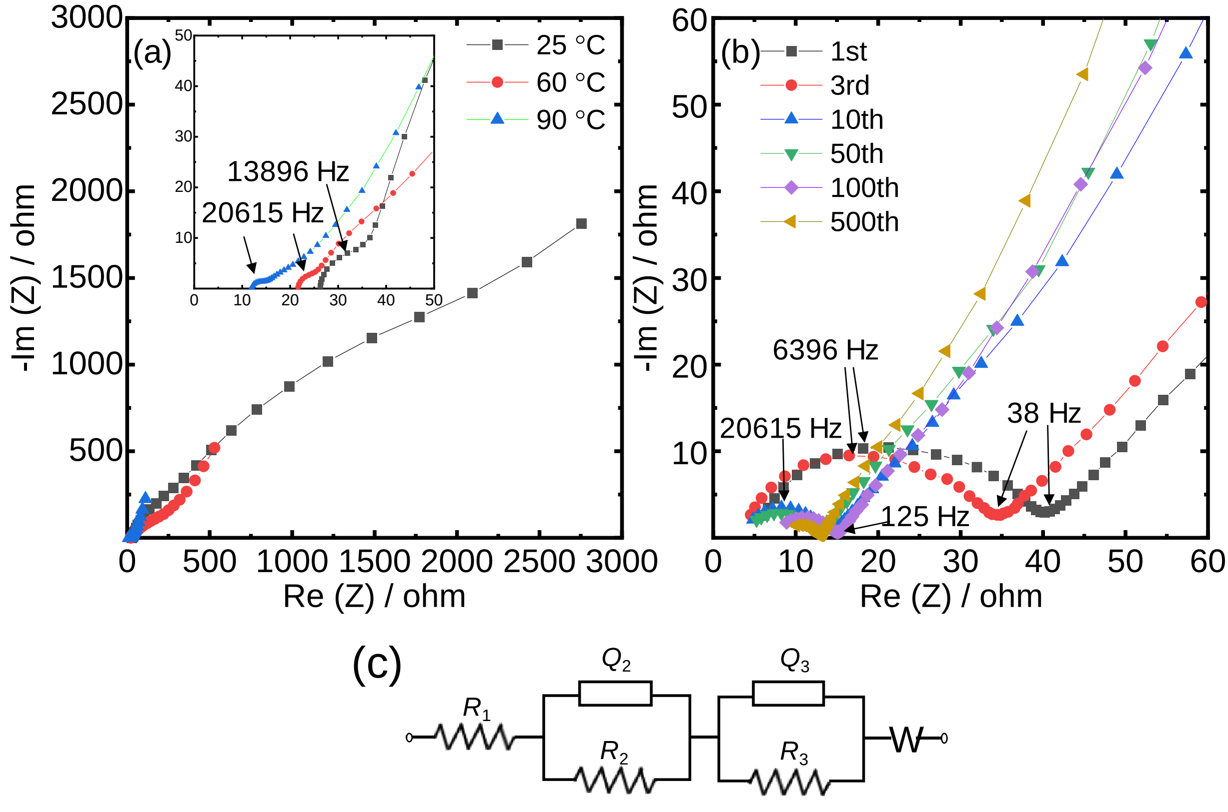

Figure 6-8 (a) Nyquist plots of the VP$_2$/VP$_2$ symmetric cell using the IL electrolyte at 25, 60, and 90 °C. The electrodes were charged in the Na/IL/VP$_2$ half-cell configuration to the cell voltage of 0.5 V and retrieved to prepare the symmetric cells. Inset shows the magnified view of the plots. (b) Nyquist plot of the Na/VP$_2$ half-cell using the IL electrolyte during 500 cycles at 90 °C. (c) Equivalent circuit for fitting Nyquist plots in both symmetric cell and half-cell cases. All the EIS tests were performed with amplitude of 20 mV and frequency range of 100 kHz−10mHz.

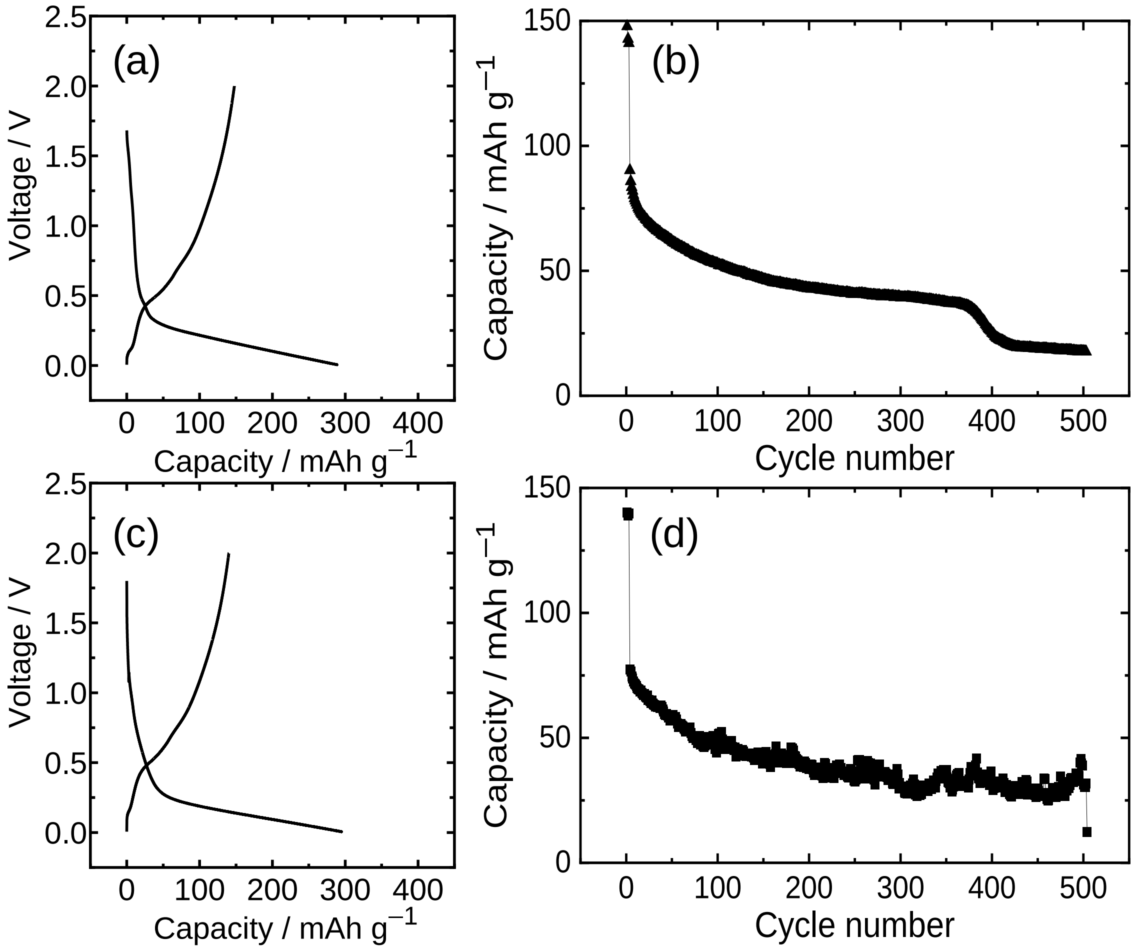

Figure 6-9 Electrochemical behavior of the VP_2 electrode using the 1 mol dm^{-3} $NaPF_6$ in EC:DEC (1:1 v/v) and 1 mol dm^{-3} $NaPF_6$ in EC:DEC (1:1 v/v) with 3 wt% FEC organic electrolyte at 25 °C. (a,c) Galvanostatic charge-discharge curves (current density: 100 mAg^{-1} and cut-off voltage: 0.005–2.0 V). (b,d) Cyclability during 500 cycles (rate: 100 mAg^{-1} for the first three cycles to activate the electrode and 500 mA g^{-1} for the rest of cycles) for 1 mol dm^{-3} $NaPF_6$ in EC:DEC (1:1 v/v) and 1 mol dm^{-3} $NaPF_6$ in EC:DEC (1:1 v/v) with 3 wt% FEC, respectively.

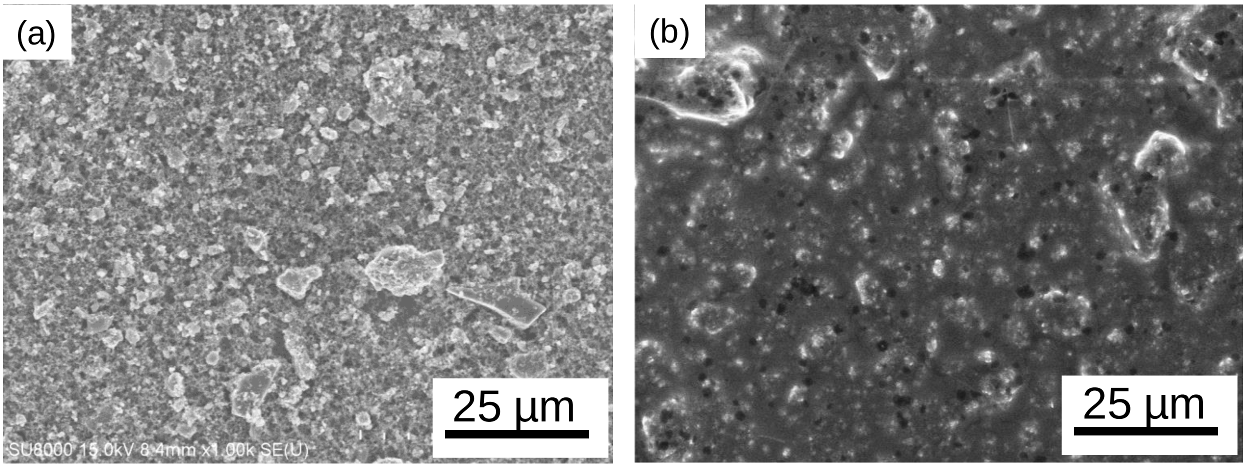

Figure 6-10 SEM images of the VP_2 electrode before and after cycling. (a) Pristine electrode and (b) electrode after 500 cycles at 90 °C using the IL electrolyte.

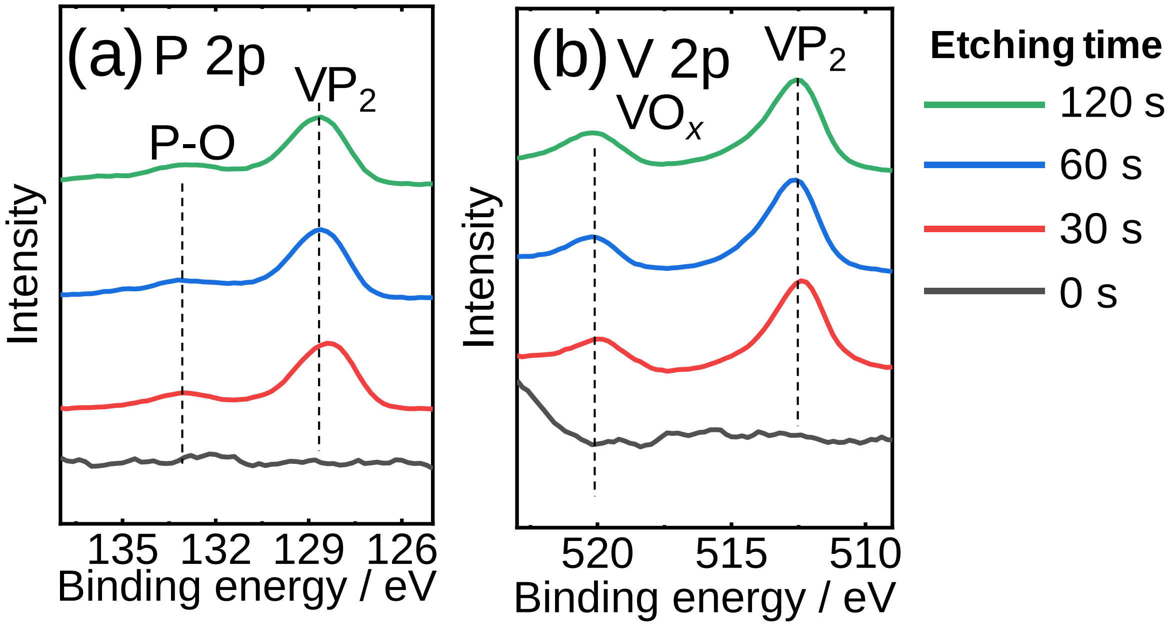

Figure 6-11 XPS depth profiles of the VP$_2$ electrode which was charged and discharged to 2.0 V at 90 °C in the IL electrolyte and etched by Ar-ion bombardment for 0, 30, 60 and 120 s. The 0s sample means the one without etching.

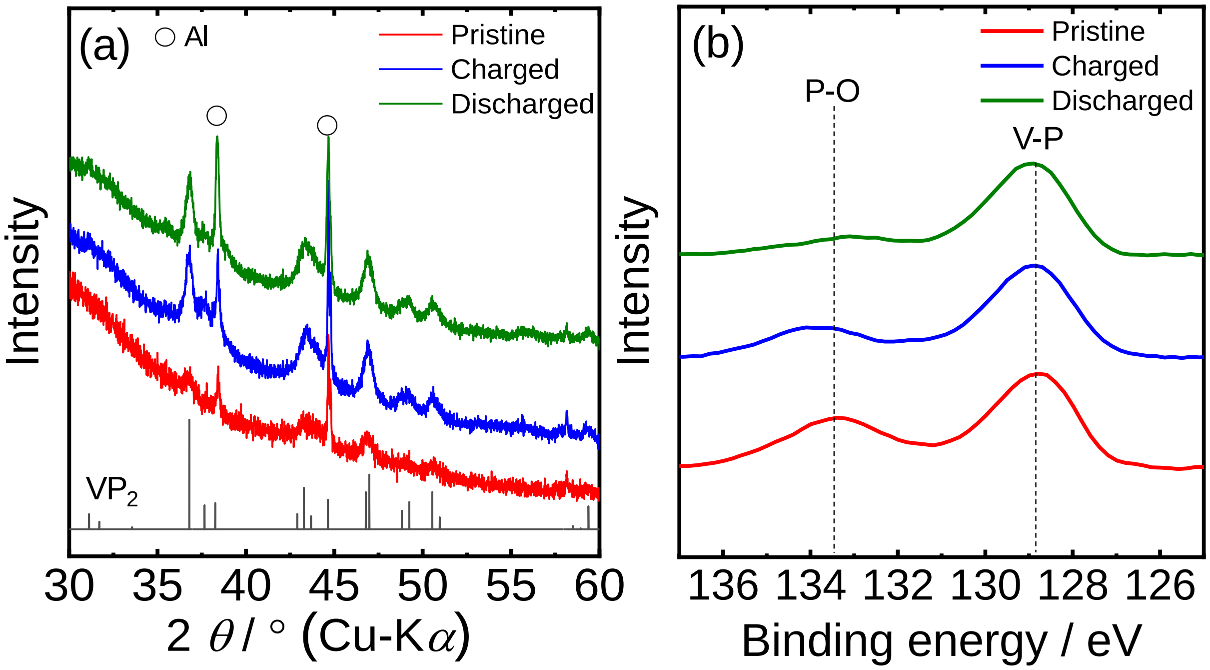

Figure 6-12 (a) *Ex-situ* XRD patterns of the VP_2 electrode in different conditions using the IL electrolyte (pristine, charged to 0.005 V, and discharged to 2.0 V). The reference pattern of VP_2 is also shown for comparison [18]. (b) *Ex-situ* P 2p XPS spectra of the VP_2 electrode (pristine, charged to 0.005 V, and discharged to 2.0 V) after Ar-etching of 180 s for the charged and discharged sample.

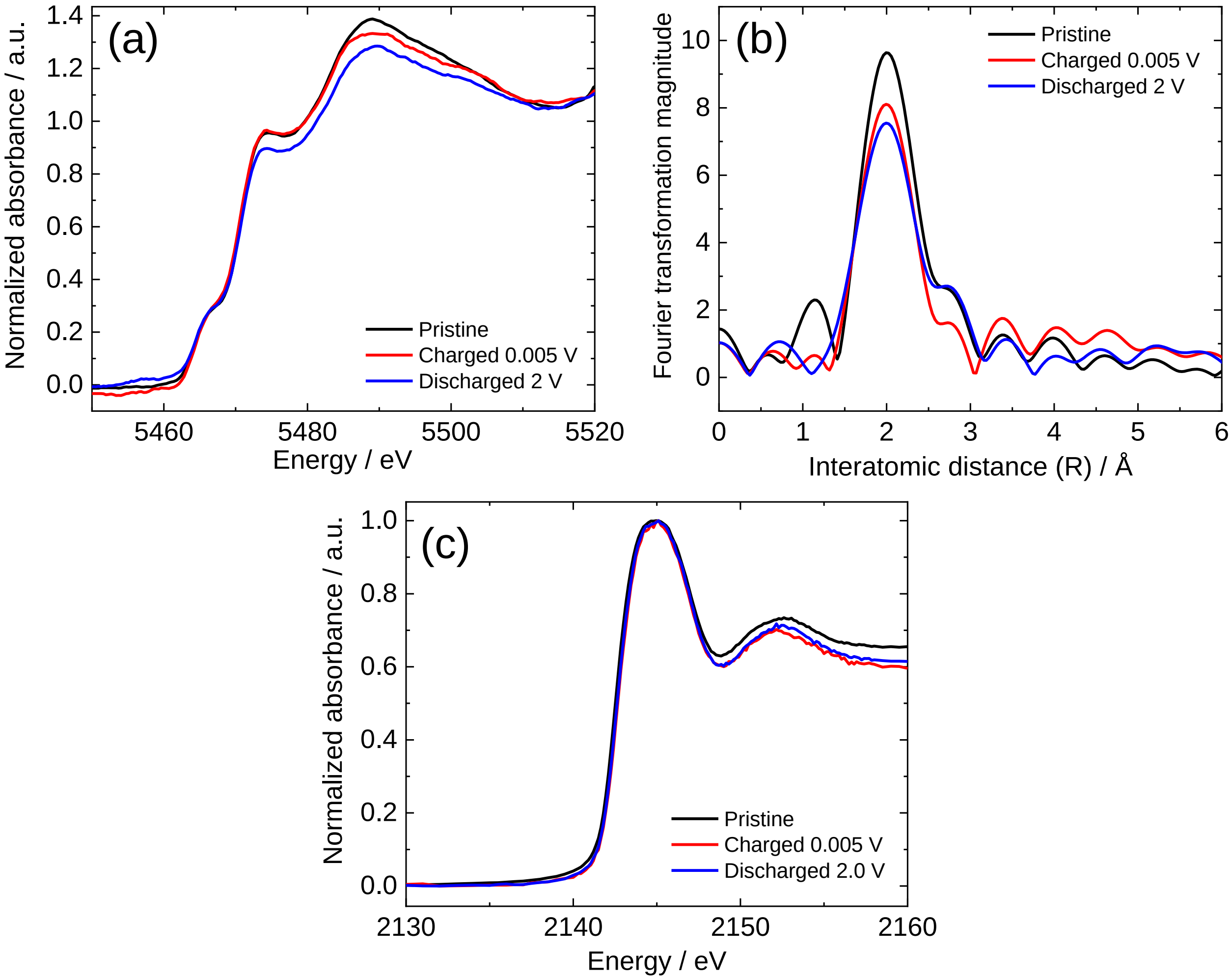

Figure 6-13 XAFS analysis data of the VP_2 electrode in different conditions using the IL electrolyte (pristine, charged to 0.005 V, and discharged to 2.0 V). (a) V *K*-edge XANES spectra, (b) Fourier transforms of the V *K*-edge EXAFS oscillations, (c) P *K*-edge XANES spectra.

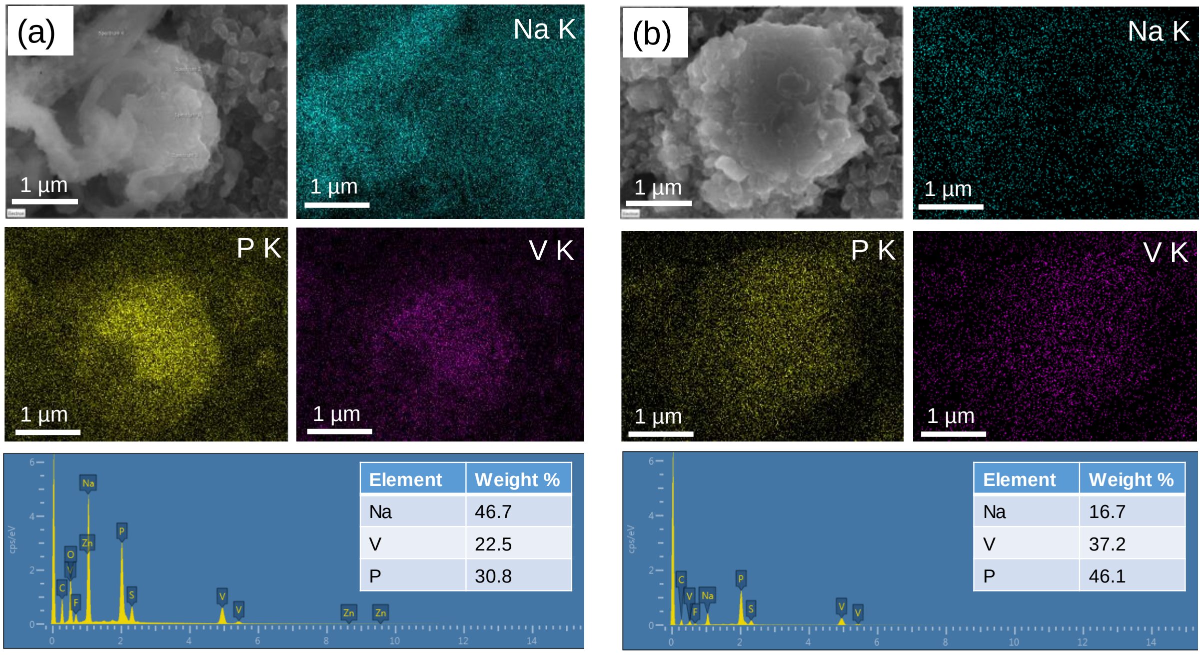

Element	Weight %
Na	46.7
V	22.5
P	30.8

Element	Weight %
Na	16.7
V	37.2
P	46.1

Figure 6-14 SEM/EDX of the VP$_2$ electrode after (a) charged (0.005 V) and (b) discharged (2.0 V) in the first cycle using IL at 90 °C.

References

[1] M. Dahbi, N. Yabuuchi, K. Kubota, K. Tokiwa, S. Komaba, Phys. Chem. Chem. Phys., 16 (2014) 15007-15028.

[2] P. Senguttuvan, G. Rousse, M.E. Arroyo y de Dompablo, H. Vezin, J.M. Tarascon, M.R. Palacín, J. Am. Chem. Soc., 135 (2013) 3897-3903.

[3] A. Rudola, K. Saravanan, S. Devaraj, H. Gong, P. Balaya, Chem. Commun., 49 (2013) 7451-7453.

[4] S.H. Woo, Y. Park, W.Y. Choi, N.-S. Choi, S. Nam, B. Park, K.T. Lee, J. Electrochem. Soc., 159 (2012) A2016-A2023.

[5] Q. Xia, W. Li, Z. Miao, S. Chou, H. Liu, Nano Res., 10 (2017) 4055-4081.

[6] L. Liu, Q. Li, Z. Wang, J. Yan, Y. Chen, Funct. Mater. Lett., 11 (2018) 1830001.

[7] Z. Li, H. Zhao, J. Mater. Chem. A, 6 (2018) 24013-24030.

[8] C.-M. Park, Y.-U. Kim, H.-J. Sohn, Chem. Mater., 21 (2009) 5566-5568.

[9] Y.-U. Kim, B.W. Cho, H.-J. Sohn, J. Electrochem. Soc., 152 (2005) A1475-A1478.

[10] F. Gillot, M. Ménétrier, E. Bekaert, L. Dupont, M. Morcrette, L. Monconduit, J.M. Tarascon, J. Power Sources, 172 (2007) 877-885.

[11] K.-H. Kim, J. Choi, S.-H. Hong, Chem. Commun., 55 (2019) 3207-3210.

[12] K.-H. Kim, C.-H. Jung, W.-S. Kim, S.-H. Hong, J. Power Sources, 400 (2018) 204-211.

[13] M. Moshkovich, Y. Gofer, D. Aurbach, J. Electrochem. Soc., 148 (2001) E155.

[14] U. Purushotham, N. Takenaka, M. Nagaoka, RSC Adv., 6 (2016) 65232-65242.

[15] J.Y. Jang, Y. Lee, Y. Kim, J. Lee, S.-M. Lee, K.T. Lee, N.-S. Choi, J. Mater. Chem. A, 3 (2015) 8332-8338.

[16] A. Ponrouch, A.R. Goñi, M.R. Palacín, Electrochem. Commun., 27 (2013) 85-88.

[17] W. Jeitschko, P.C. Donohue, V. Johnson, Acta Crystallogr. Sect. B, 32 (1976) 1499-1505.

[18] M. Geolin, B. Carlsson, S. Rundqvist, Acta Chem. Scand. A, 29 (1975) 706-708.

[19] K. Selte, A. Kjekshus, A.F. Andresen, Acta Chem. Scand., 26 (1972) 4057-4062.

[20] J.-h. Yang, S.-h. Cheng, X. Wang, Z. Zhang, X.-r. Liu, G.-h. Tang, Trans. Nonferrous Met. Soc. China, 16 (2006) s796-s803.

[21] S.-O. Kim, A. Manthiram, Chem. Commun., 52 (2016) 4337-4340.

[22] C.E. Myers, H.F. Franzen, J.W. Anderegg, Inorg. Chem., 24 (1985) 1822-1824.

[23] H. Igarashi, K. Tsuji, T. Okuhara, M. Misono, J. Phys. Chem., 97 (1993) 7065-7071.

[24] C.H. Chen, J. Liu, K. Amine, J. Power Sources, 96 (2001) 321-328.

[25] N. Ogihara, Y. Itou, T. Sasaki, Y. Takeuchi, J. Phys. Chem. C, 119 (2015) 4612-4619.

[26] J. Hwang, K. Matsumoto, R. Hagiwara, J. Phys. Chem. C, 122 (2018) 26857-26864.

[27] S.S. Zhang, K. Xu, T.R. Jow, Electrochim. Acta, 51 (2006) 1636-1640.

[28] J. Hwang, K. Takeuchi, K. Matsumoto, R. Hagiwara, J. Mater. Chem. A, 7 (2019) 27057-27065.

Chapter 7

Synergistic Effects of Amorphous SiP_2/C Negative Electrode and Ionic Liquid Electrolyte

7.1 Introduction

Apart from transition metal phosphides, phosphides based on elements in group 14 in the periodic table such as GeP_5/C [1] and Sn_4P_3 [2], have shown large reversible capacities for NIBs owing to the activity of both the components. A hybrid (conversion + alloying) reaction mechanism has been reported in these materials discussed in detail in Chapter 1 (section 1.3.4.3). Recently, SiP_2 has also been investigated as a negative electrode material for NIBs. However, the crystalline Si has been reported to be inactive [3], which results in theoretical capacity of SiP_2 to be 1780 mA h g^{-1} based on sodiation of P only. However, in the same study, amorphous Si showed limited activity (~75 mA h g^{-1}), which attracts attention for further investigation. The first study on SiP_2/Na was reported in 2016 by Monconduit group. The SiP_2 was prepared by HEBM and showed a high discharge capacity of 843 mA h g^{-1} at 890 mA g^{-1} in the first cycle, but rapid capacity fading occurred in the subsequent cycles [4]. The same group investigated the underlying charge-discharge mechanism by employing *in-situ* XRD and MAS NMR technique which revealed the amorphization of SiP_2 after charging and absence of Na_3P peaks [5]. MAS NMR showed the absence of any negative or positive chemical shifts after charging and a difficulty of reaction between Na and SiP_2 was suggested. The electrochemical performance of SiP_2 was significantly improved by the preparation of carbon composite (SiP_2/Super P) using HEBM [6]. The SiP_2/C (60:40 w/w) delivered a discharge capacity of 501 mA h g^{-1} at 50 mA g^{-1} and 80% capacity retention after 500 cycles. Furthermore, *in-situ* XRD and *in-situ* TEM studies showed the formation of Na_3P and $NaSi_6$ after charging and partial reversibility to recover SiP_2 after discharging. In another study, SiP_2/multiwalled carbon nanotube composite (62.5:38.5 w/w) displayed a large capacity of 925 mA h g^{-1} at 200 mA g^{-1}, 129% capacity retention after 200 cycles and 491 mA h g^{-1} at 2000 mA g^{-1} [7]. These studies have indicated that the electrochemical performance of SiP_2 was highly improved by preparing SiP_2/C(nanotube) composites although the charge-discharge mechanism is not well understood.

Another decisive factor for improving electrochemical performance is electrolyte. As shown in all the previous chapters, employing IL has resulted in achieving high performance at room temperature as well as intermediate temperature. Especially, the rate capability is considerably improved at intermediate temperature in our studies, and activation of some inactive materials has been reported in another literature [8]. A robust and uniform SEI layer formation on the working electrode and Na metal counter electrode has also been observed in IL, which significantly improves the overall performance [9-11]. Safety of the operation also increases in IL systems owing to the low flammability, negligible volatility, and high thermal stability [12].

In this work, the electrochemical behavior of the SiP_2/C negative electrode in the Na[FSA]–[C_3C_1pyrr][FSA] IL is investigated at 25 and 90 °C. The SiP_2/C prepared by HEBM is characterized by XRD, SEM, and XPS. The charge-discharge performance is compared in IL and organic electrolyte at 25 °C and evaluated using EIS. The charge-discharge mechanism was investigated by *ex-situ* XRD at 90 °C.

7.2 Experimental

The silicon phosphide (SiP_2) sample was prepared by HEBM of Si (Kojundo Chemical Laboratory, purity 99.9%) and red phosphorus powder (Wako Pure Chemical Industries, purity 98%) in a stoichiometric ratio (1:2 in mol) under Ar atmosphere with a ball to powder weight ratio of 35:1. The ball-milling process was carried out at 800 RPM for 5, 10, and 20 h to optimize the reaction time for the formation of SiP_2. The resulting powder was collected from the vessel and ball-milled again with either 20 or 30% weight ratio of AB (Wako Pure Chemical Industries) separately under the same conditions for 3 h to obtain the SiP_2/C composite. The effect of ball-milling time on crystallinity was also investigated.

The XRD patterns of the samples were obtained on a Rigaku SmartLab diffractometer (CuKα (0.15418 nm), 40 kV–30 mA) under Ar atmosphere. The samples were sealed in an airtight cell with Be windows under an Ar atmosphere and set on the diffractometer. XPS measurements were carried out using a JEOL JPS-9010 spectrometer (MgKα, 10 kV–10 mA). The spectra were calibrated by the contaminated carbon in C1s (284.5 eV) as a reference. The particle size and morphology were determined by SEM (Hitachi SU-8020), and elemental mapping analysis was performed by EDX (Horiba EMAX Evolution X-max), respectively.

The negative electrode was prepared by mixing the active material (SiP_2/C), AB, and PAI binder (75:15:10 by weight) in NMP (Wako Pure Chemical Industries, purity 99%) using a planetary centrifugal mixer (AR-100, Thinky). The resulting slurry was cast on Al foil (20 µm) and dried under vacuum at 90 °C for 10 h in an oven and on a vacuum line at 110°C for 48 h. The loading mass of active material was in the range of 0.75-1 mg cm^2. The Na[FSA]–[C_3C_1pyrr][FSA] (20:80 mol ratio) was used as the IL electrolyte. An organic electrolyte of 1 mol dm^{-3} Na[FSA] in ethylene carbonate/dimethyl carbonate (1:1 v/v) (ORG$_{FSA}$) was also used for comparison. A glass fiber filter (Whatman, GFA, 260 mm in thickness and 16 mm in diameter) was used as a separator. A sodium metal disc (Aldrich, purity 99.9%) was used as the counter electrode. Coin cells (2032-type) were assembled in the Ar-filled glove box to measure the electrochemical performance.

Electrochemical performance was measured using a HJ1001SD8 charge-discharge test device (Hokuto Denko). All the coin cells were held at the open-circuit voltage for at least 3 h in an ESPEC thermostatic chamber before the measurements.

EIS was performed on a VSP potentiostat (Bio-Logic) at 25 and 90 °C over the frequency range from 100 mHz to 100 kHz, with an AC amplitude of 20 mV. The symmetric cells were prepared using 2032 coin cells by replacing Na metal with SiP_2/C in normal half-cell configurations. EIS profiles were obtained at 0.5 V in the charging step of the (n+1)th cycle (n = 1, 3, 10, 50).

7.3 Results and discussion

Three reaction times (5, 10, and 20 h) for ball-milling Si with P were tested to prepare SiP_2, and a ball-milling time of 20 h was found to be necessary to complete the reaction (Figure 7-1). The SiP_2 peaks appeared after 10 h of ball-milling, and the Si peaks completely disappeared after 20 h. The following experiments were conducted for the SiP_2 sample with 20 h of ball-milling. The resulting SiP_2 was further ball-milled with AB in SiP_2:C ratios of 80:20 and 70:30 (Notations hereafter are SiP_2/C (80:20) and SiP_2/C (70:30), respectively) to enhance the electronic conductivity. The XRD patterns of the as-prepared SiP_2, SiP_2/C (80:20) and SiP_2/C (70:30) are shown in Figures 7-2 (a), (b), and (c), respectively. All the diffraction peaks of SiP_2 were indexed to the pyrite-type SiP_2 phase [13]. However, after ball-milling with AB, all the SiP_2 peaks disappeared in the spectra of both the SiP_2/C (80:20) and SiP_2/C (70:30) powders, indicating amorphization of the material. This phenomenon is commonly observed [14-16] during ball-milling under intense conditions due to the continuous heavy impact and abrasion of the particles.

Figure 7-3 shows the XPS profiles of (a) SiP_2/C (80:20) and (b) SiP_2/C (70:30) in the P2p region. The peaks around 129 eV in both the cases confirm the formation of SiP_2. However, the peaks showed a slight shift to the lower-energy side than those of the literature data [17], which could be due to ball-milling at a very high speed. The peak at 132.5 eV, corresponding to the P-O-C bond, was significantly more intense than the SiP_2 peak, indicating that the majority of the phosphorus on the particle surface is present in this form. A recent report on a ball-milled SiP_2/CNT composite also confirmed the formation of a P-O-C bond [18]. This P-O-C bond is responsible for good cycleability as it restricts volume change and provides high electrical conductivity, which preserves interparticle connectivity even after long-term cycling [19-21].

Figure 7-4 shows the SEM images and EDX maps of the (a,b) SiP_2, (c,d) SiP_2/C (80:20) and (e,f) SiP_2/C (70:30) composites, revealing the morphological characteristics as irregular aggregates of 50–500 nm in size and uniform distribution of elements.

The galvanostatic charge/discharge profiles of the as-prepared SiP_2, SiP_2/C (80:20), and SiP_2/C (70:30) in IL at 90 °C are shown in Figures 7-5 (a), (b), and (c), respectively (current density: 100 mA g^{-1} and voltage range: 0.005−2.0 V). SiP_2 without conductive carbon delivered a large initial charge capacity of 1153 mAh g^{-1} (Figure 7-5 (a)), but the discharge capacity was merely 226 mA h g^{-1}, giving a Coulombic efficiency of 20%. This result could be attributed to the difficulty in sodium extraction because of the low electrical conductivity of SiP_2. On the other hand, SiP_2/C (80:20) and SiP_2/C (70:30) demonstrated high discharge capacities of 883 and 791 mAh g^{-1} with Coulombic efficiencies of 72% and 76% in the first cycle (Figures 7-5 (b) and (c)), respectively. The irreversible capacity was partially due to the reductive decomposition of the electrolyte on the electrode surface to form the SEI layer. The drastic increase of Coulombic efficiency in the first cycle compared to that of the as-prepared SiP_2 suggests the important role of the conductive carbon. The charge-discharge curves of the subsequent cycles essentially overlapped with each other, indicating good reversibility of the sodiation and desodiation processes in the SiP_2/C composite at 90 °C. The redox activity of SiP_2

and SiP_2/C (70:30) against voltage was quantified by dQ/dV plots as shown in Figure 7-6. During the first cathodic scan of the SiP_2 electrode (Figure 7-6(a)), the two peaks in the range between 1.0 and 1.5 V can be attributed to electrolyte decomposition because of the irreversibility of the peaks, and the following large peak starting at 0.13 V corresponds to sodiation of SiP_2. During the anodic process, a three step desodiation process was observed around 0.1, 0.25, and 0.8 V. In the second and third cycle, limited reduction activities were observed during the cathodic process detected only in the low voltage zone. The weakened peak intensity and shifting to higher voltage during the anodic process shows increasing polarization with cycling. On the other hand, better reversibility was observed in the case of SiP_2/C (70:30). In the first cycle, two small peaks corresponding to the electrolyte decomposition around 1.3 and 1.0 V and one sodiation peak at 0.2 V were observed during the cathodic process (Figure 7-6 (b)). Subsequently, the desodaition took place with three steps at 0.1, 0.4 and 0.65 V. The sodiation and desodiation were reversible in the second and third cycles, indicating the important role of AB to maintain the redox activity.

Figure 7-7 represents the rate capability and cycleability of SiP_2/C (80:20) and SiP_2/C (70:30) with IL at 90 °C. The SiP_2/C (70:30) showed superior rate performance to that of SiP_2/C (80:20), with a discharge capacity of 790 mA h g^{-1} at 100 mA g^{-1}, 740 mA h g^{-1} at 500 mA g^{-1}, 710 mA h g^{-1} at 1000 mA g^{-1}, and 420 mA h g^{-1} at 8000 mA g^{-1}, as shown in Figure 7-7 (a). Figure 7-7 (b) shows the cycling performance of SiP_2/C (80:20) and SiP_2/C (70:30) at 500 mA g^{-1}, after electrochemical activation for the first three cycles at 100 mA g^{-1}. The SiP_2/C (70:30) composite exhibited stable cycling with more than 65% capacity retention after 300 cycles, with a Coulombic efficiency of 99.7%. Although high capacity was observed for SiP_2/C (80:20) during the initial cycles, severe capacity degradation was observed in the first 100 cycles with a large fluctuation in the Coulombic efficiency. The superior performance of SiP_2/C (70:30) over that of SiP_2/C (80:20) was attributed to the restriction of pulverization owing to the presence of a P-O-C bond and the high electronic conductivity with the 30% conductive carbon in the composite. Therefore, further investigations were carried out only on SiP_2/C (70:30) as described below.

The electrochemical performance of SiP_2/C (70:30) at 25 °C was compared between the Na[FSA]-based organic electrolyte, ORG_{FSA} (see Experimental section for details on this electrolyte) and IL (~1 mol dm^{-3}). Figures 7-8 (a) and (b) show the charge–discharge curves of SiP_2/C (70:30) in ORG_{FSA} and IL, respectively, for the initial 5 cycles. Although the charge capacity with ORG_{FSA} in the first cycle was similar to that of IL, the discharge capacities in the second cycle were significantly different from each other (400 mA h g^{-1} in ORG_{FSA} and 600 mA h g^{-1} in IL), indicating the different functionality of the two electrolytes. This observation agrees with those in previous reports; IL was reported to provide a uniform and robust SEI layer with electrode materials such as elemental phosphorus and metal phosphides [22, 23]. On the contrary, according to previous work [6], better performance of SiP_2/C (60:40) was obtained with an organic electrolyte. The different behavior is considered to arise from the larger carbon content and the use of a fluoroethylene carbonate additive. Other electrochemical tests with IL also showed considerably superior performance of SiP_2/C (70:30) at 25 °C. In the rate test, capacities of 540, 340, 240, and 30 mA h g^{-1} were obtained at 100, 500, 1000, and 8000 mA g^{-1}, respectively (Figure 7-8(c)). SiP_2/C (70:30) also exhibited high cycleability at the rate of 500 mA g^{-1} over 200 cycles (Figure 7-8 (d)), as characterized by the 73% capacity retention. The aforementioned results suggest that the SiP_2/C (70:30) is suitable for use as a high-performance negative electrode with long term cycleability and high-rate applications at both 25 and 90 °C.

To elucidate the difference in cycleability observed in IL and organic electrolytes, EIS measurements were performed on a Na||SiP_2/C half-cell with cycling and a symmetric cell SiP_2/C||SiP_2/C after one cycle using IL and ORG_{FSA}. The EIS results were compared for the

SiP_2/C (70:30) electrode charged to 0.5 V. Figures 7-9 (a) and (b) show the Nyquist plots for the Na||SiP_2/C half-cell during cycling at 25 °C with IL and ORG_{FSA}, respectively. With progressive cycling, the interfacial resistance for IL considerably decreased, whereas that for ORG_{FSA} increased. Figure 7-9 (c) shows the Nyquist plots for Na||SiP_2/C with IL during cycling at 90 °C. The interfacial resistance reduced significantly at 90 °C as compared to that at 25 °C, because of the low interfacial resistance offered by sodium metal at 90 °C [10]. The high rate capability obtained at 90 °C could be explained by this result. Figure 7-9 (d) shows the Nyquist plots of the SiP_2/C||SiP_2/C symmetric cell after 1 cycle at 25 °C with the IL and ORG_{FSA} electrolytes. The use of a symmetric cell is preferable to exclude the effects of the sodium metal counter electrode. Two semicircles were observed in both the cases, with a sloping curve denoting the diffusion behavior. The EIS curves were well-fitted by the corresponding parameters according to the equivalent circuit in the inset of Figure 7-9 (d) (see Table 7-1 and Table 7-2 for the optimized parameters for symmetric cell and half-cell, respectively). The R_2 value was similar in both the cases, but R_3 was considerably higher for the organic electrolyte. The characteristic frequencies accompanying R_2 and R_3 decreased in the high- and low-frequency regions, respectively. The resistances at high and low frequencies are generally related to the surface film layer resistance and charge transfer resistance, respectively [10]. Thus, it can be suggested that the increase in charge transfer resistance after cycling may be the reason behind the poor cycleability in the organic electrolyte.

The mechanism underlying the electrochemical reactions for SiP_2/C (70:30) in IL at 90 °C was investigated by *ex situ* XRD analysis (Figure 7-10). The SiP_2/C (70:30) electrode is amorphous before the reactions, as shown in Figure 7-2 (b), but some unknown peaks were observed at 23.9° and 46.7° in the pristine electrode, which may arise from the impurity introduced during the electrode washing or XRD measurements. After charging and discharging, no new peak appeared in the XRD patterns, indicating that all the products are amorphous. This reaction mechanism is different from the previously reported one, which suggested the formation of Na_3P and $NaSi_6$ during the charging process and re-formation of amorphous SiP_2 and phosphorus during the discharge process [6]. Differences in the crystallinity of the electrode material, reaction temperature, and electrolyte possibly cause such differences. The large capacity attained at 90 °C led to a deeper charging state and affected the reaction mechanism (*e.g.* 790 mA h g^{-1} at 100 mA g^{-1}).

7.4 Conclusions

SiP_2, SiP_2/C (80:20), and SiP_2/C (70:30) were prepared by high-energy ball-milling and investigated for use as negative electrodes in NIBs. SiP_2/C (70:30) demonstrated better performance than did SiP_2/C (80:20), with high capacity of 420 mA h g^{-1} at a high rate of 8000 mA g^{-1} and 65% capacity retention after 300 cycles at 90 °C in IL. The charge-discharge curves of SiP_2/C (70:30) at 25 °C showed stable cycleability and higher discharge capacity in the case of IL than in the case of ORG_{FSA}. The presence of P-O-C bond, enhanced ionic conductivity of IL and the low interfacial resistance with cycling are suggested to be the reasons for the good performance observed in IL. Symmetric cell EIS measurements on SiP_2/C||IL||SiP_2/C at 25 °C revealed significantly lower charge transfer resistance than that of SiP_2/C||ORG_{FSA}||SiP_2/C after one cycle. The products after charging and discharging were found to be amorphous for SiP_2/C (70:30), in contrast to a previous study where crystalline Na_3P and $NaSi_6$ were observed after first charging. This difference might occur due to differences in the crystallinity of the starting active material and electrolyte as well as the higher depth of charge. The detailed study of charge/ discharge mechanism is a matter of future investigation. In this study, the obtained results clearly states that the utilization of ionic liquid is beneficial for NIBs enabling high performance of SiP_2/C (70:30) and promoting safer operations.

Table 7-1 EIS fitting data for the $SiP_2/C||SiP_2/C$ symmetric cell with IL (Na[FSA]-[C_3C_1pyrr][FSA] (20:80 in mol)) and ORG_{FSA} (1 mol dm^{-3} Na[FSA]-EC/DEC) at 25 °C (Figure 7-9 (d)).

	Resistance / Ω (Characteristic freq. / Hz)			**CPE / F $s^{(a-1)}$**				**W / Ω $s^{-1/2}$**
	R_1	R_2	R_3	Q_2	a_2	Q_3	a_3	
IL	8.3	10.6 (17467)	19.8 (165)	0.86 $x10^{-6}$	1	0.12 $x10^{-3}$	0.87	33.66
ORG_{FSA}	11.9	11.97 (44694)	123.2 (11.2)	27.23 $x10^{-6}$	0.64	0.51 $x10^{-3}$	0.65	234.5

Table 7-2 EIS fitting data for the $Na||SiP_2/C$ half cell with IL and ORG_{FSA} at 25 °C and 90 °C (Figure 7-9 (a-c)).

		Resistance / Ω			**CPE / F $s^{(a-1)}$**			
Sample	**Cycle**	R_1	R_2	R_3	Q_2	a_2	Q_3	a_3
ORG_{FSA} (25°C)	1	0.91	5.31	94.53	$9.00x10^{-6}$	0.832	$1.64x10^{-5}$	0.819
	3	1.59	4.90	109.00	$1.41x10^{-5}$	0.522	$1.46x10^{-5}$	0.841
	10	7.98	8.19	159.90	$1.23x10^{-5}$	0.860	$9.12x10^{-6}$	0.911
IL (25°C)	1	4.86	6.81	574.60	$7.97x10^{-6}$	0.893	$4.51x10^{-6}$	0.828
	3	4.59	5.69	288.20	$5.98x10^{-6}$	0.805	$3.48x10^{-6}$	0.975
	10	7.39	10.27	167.90	$1.90x10^{-6}$	1	$1.17x10^{-5}$	0.775
IL (90°C)	1	5.71	7.49	7.23	$9.27x10^{-6}$	1	$2.03x10^{-6}$	0.967
	3	5.51	9.83	10.11	$1.14x10^{-5}$	0.985	$2.58x10^{-6}$	0.926
	10	5.19	7.86	18.86	$5.26x10^{-6}$	0.887	$7.86x10^{-5}$	0.713

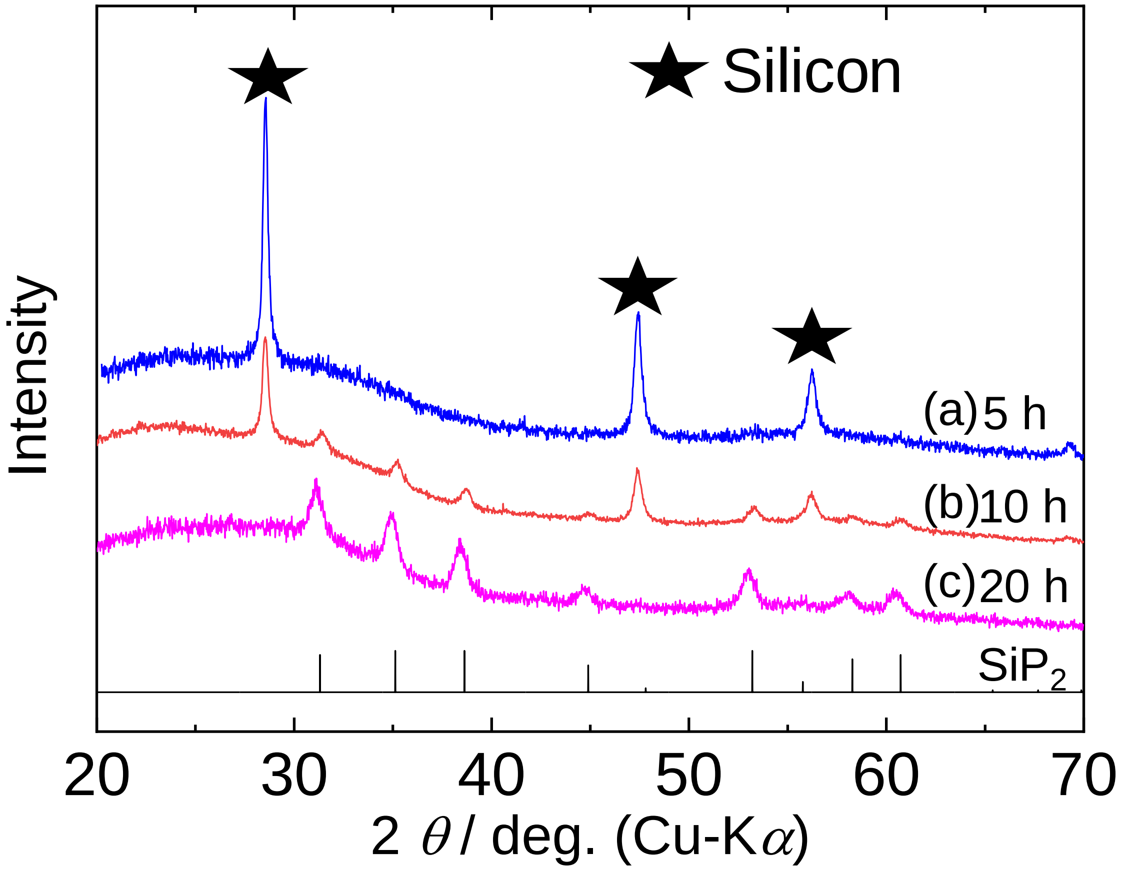

Figure 7-1 Comparison of XRD patterns of SiP_2 prepared by ball-milling of Si and P (ball-milling time: (a) 5h, (b) 10h, and (c) 20h).

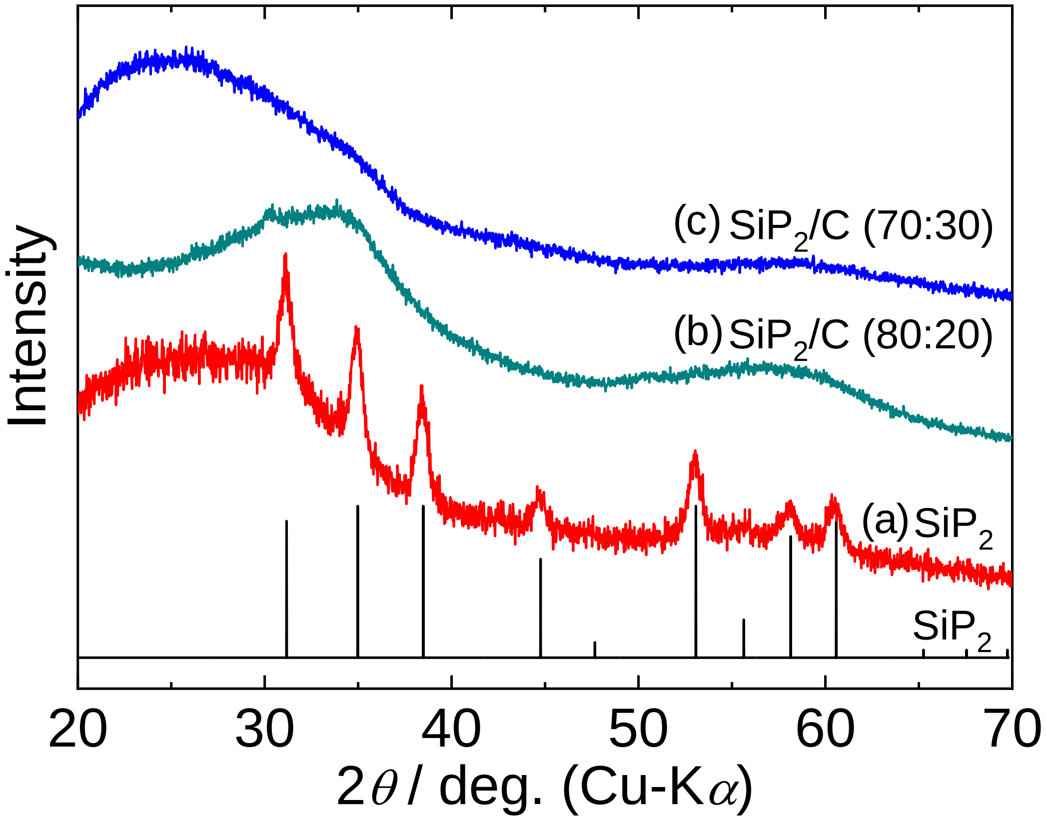

Figure 7-2 XRD patterns of (a) as-prepared SiP_2, (b) SiP_2/C (80:20), and (c) SiP_2/C (70:30). The reference pattern of pyrite-type SiP_2 [13] is shown for comparison.

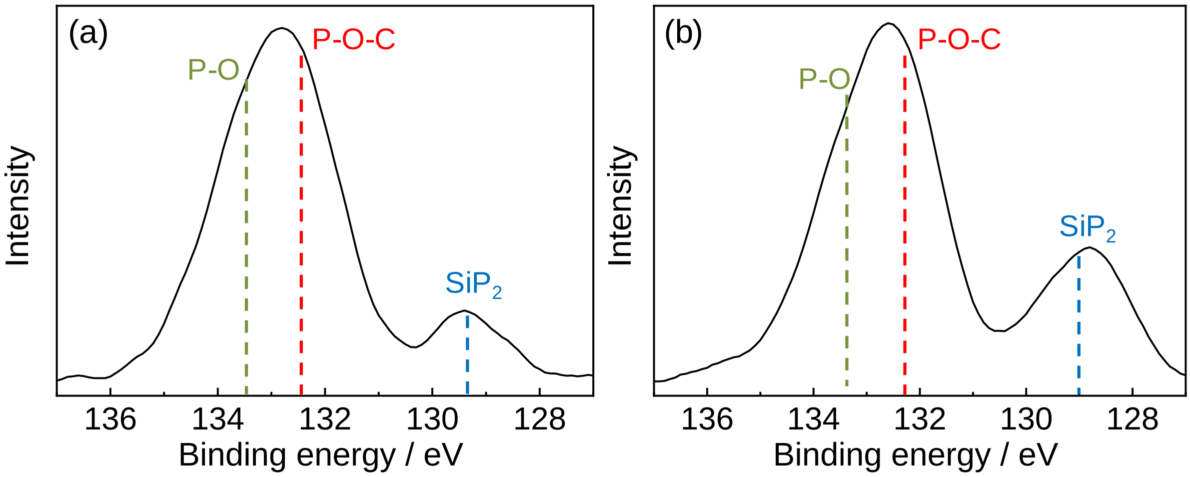

Figure 7-3 XPS (P2p) profiles of (a) SiP_2/C (80:20) and (b) SiP_2/C (70:30).

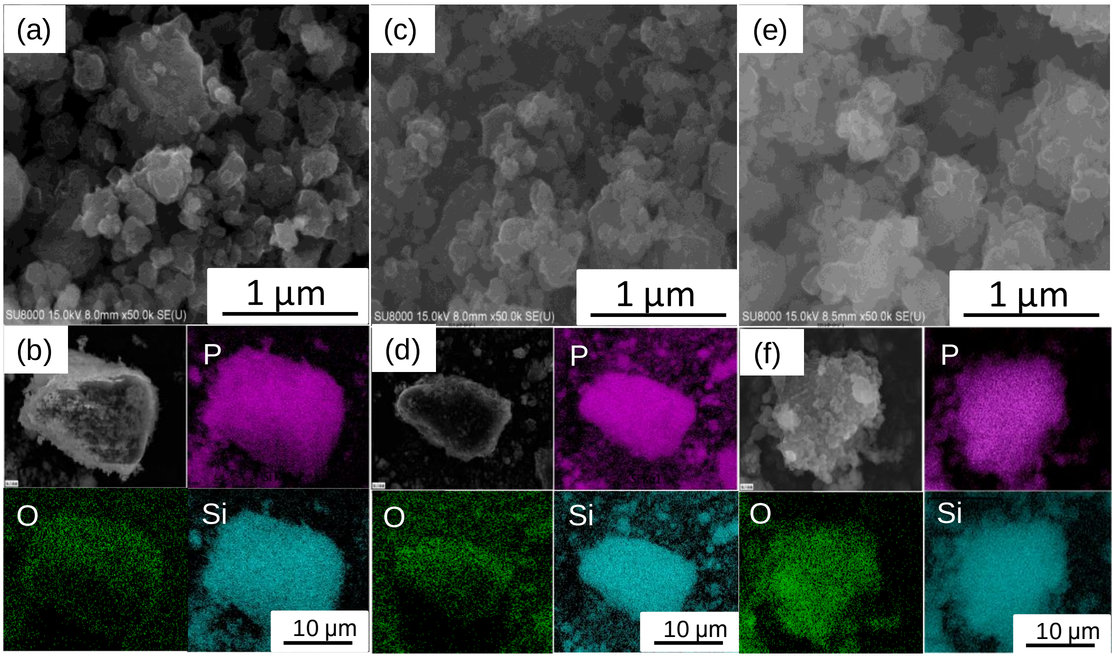

Figure 7-4 SEM images and EDX mapping results of (a,b) as-prepared SiP_2, (c,d) SiP_2/C (80:20), and (e,f) SiP_2/C (70:30).

Brief comments:

The prepared SiP_2 appears as irregular aggregates, while ball-milling with carbon does not cause obvious morphological differences, regardless of the carbon content. The EDX mapping results show the uniform distribution of elements (Si, P, and O) in the particles in each case, as shown in Figure 7-4 (b), (d) and (f).

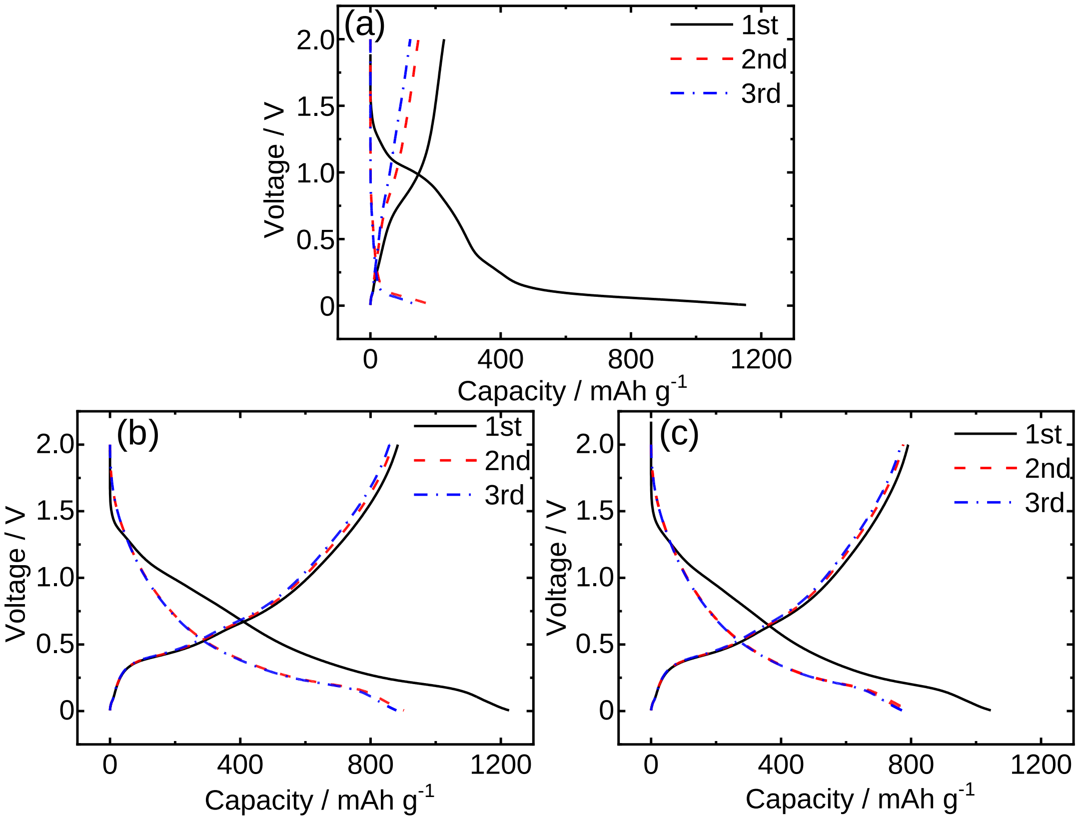

Figure 7-5 Galvanostatic charge-discharge curves of (a) as-prepared SiP_2, (b) SiP_2/C (80:20), and (c) SiP_2/C (70:30) electrodes in IL at 90 °C (rate: 100 mA g^{-1}, voltage range: 0.005–2.000 V).

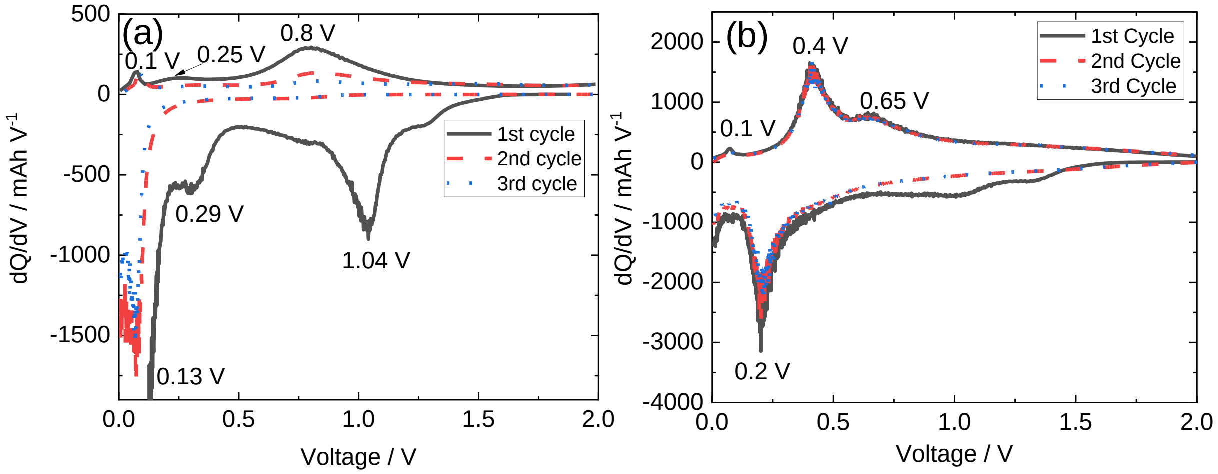

Figure 7-6 The d*Q*/d*V* plots derived from the charge-discharge curves in Figure 7-5 of (a) SiP_2 and (b) SiP_2/C (70:30) at 90 °C using IL.

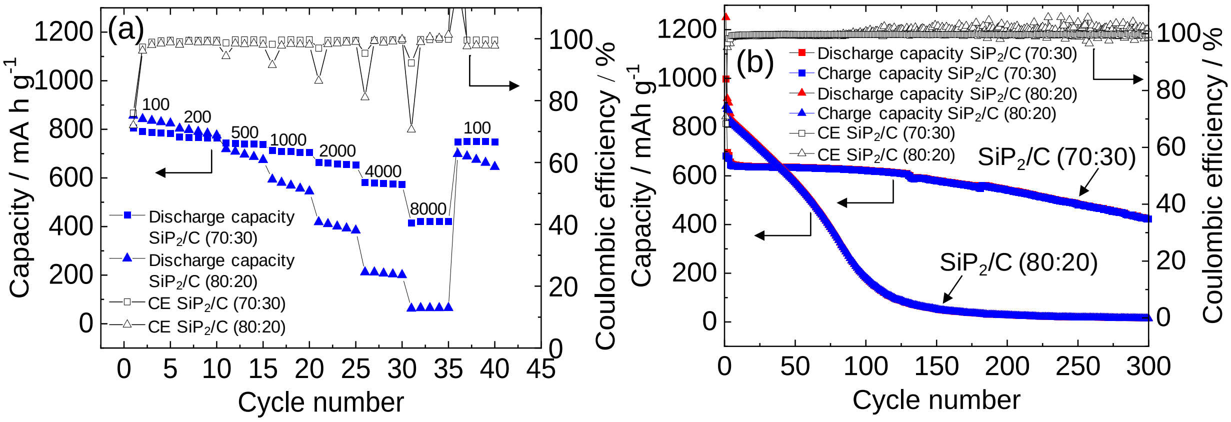

Figure 7-7. (a) Rate capability of SiP$_2$/C (80:20) and SiP$_2$/C (70:30) electrodes at 90 °C (rate: 100–8000 mAg^{-1}) and (b) cycleability at 90 °C (rate: 500 mAg^{-1}, first three cycles at 100 mAg^{-1}).

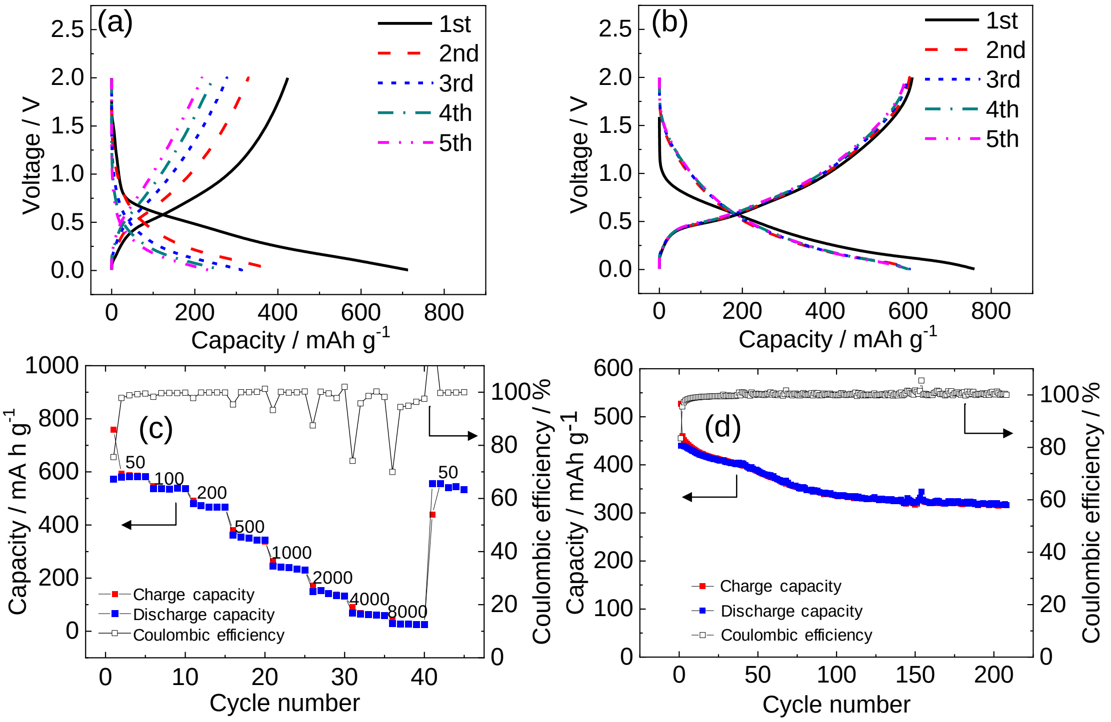

Figure 7-8 Galvanostatic charge-discharge curves of SiP$_2$/C (70:30) at 25 °C with (a) ORG$_{FSA}$ and (b) IL (rate: 100 mA g^{-1}, voltage range: 0.005–2.0 V). (c) rate capability test (rate: 100 – 8000 mA g^{-1}) with IL, and (d) cycleability (rate: 200 mAg^{-1}, initial three cycles at 100 mA g^{-1}) with IL. The Coulombic efficiency in the 41st cycle in (c) is 126.7%.

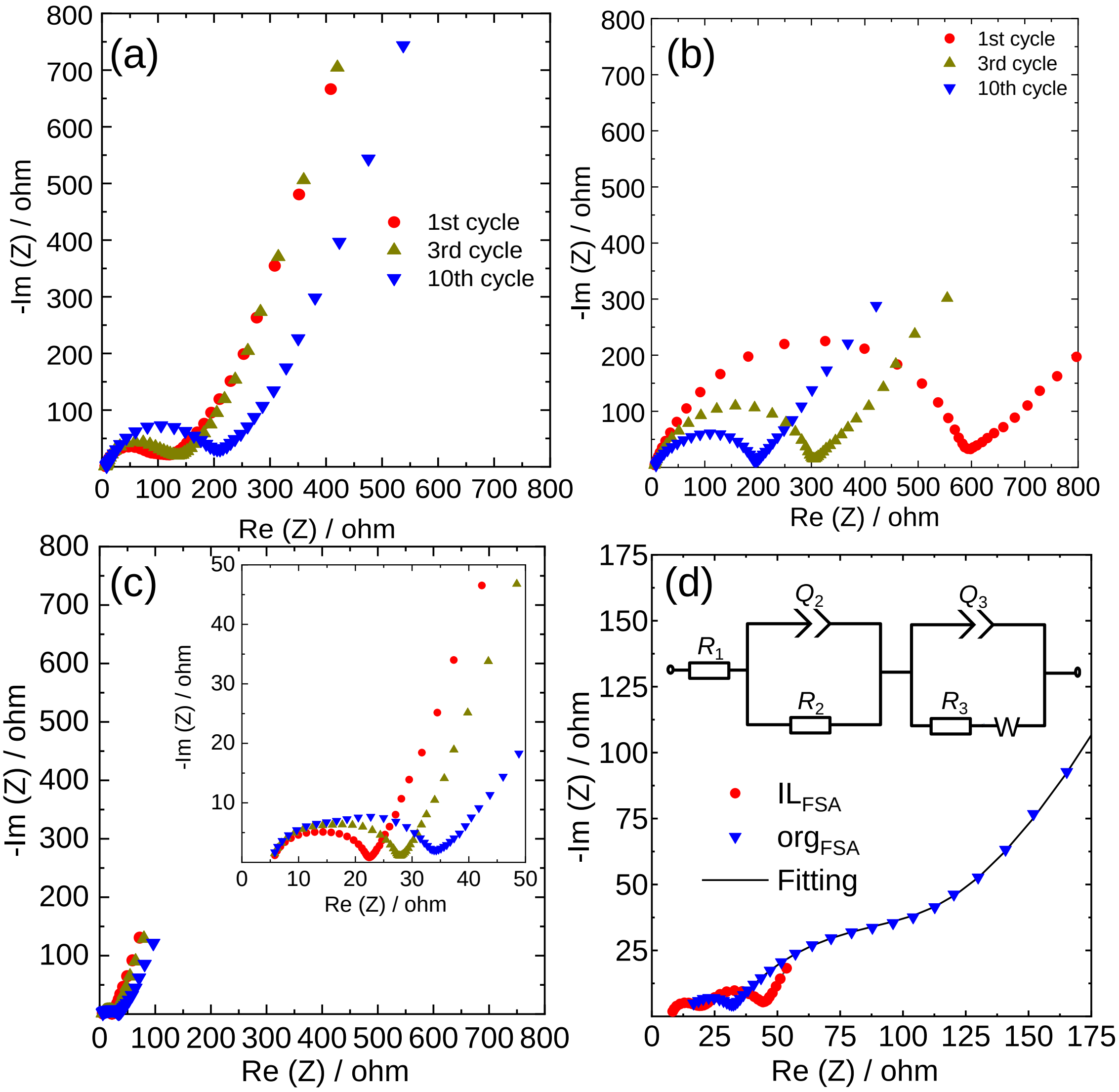

Figure 7-9. Results of EIS tests for the SiP$_2$/C (70:30) electrode. (a-c) Nyquist plots of the Na||SiP$_2$/C cell with cycling at (a) 25 °C with ORG$_{\text{FSA}}$, (b) 25 °C with IL, and (c) 90 °C with IL (inset magnified view). (d) Nyquist plots of SiP$_2$/C||SiP$_2$/C symmetric cell at 25 °C with ORG$_{\text{FSA}}$ and IL. For (a)-(c), galvanostatic charge-discharge was performed in the half-cell at a rate of 100 mA g^{-1} in the first 10 cycles and 500 mA g^{-1} in 11-50 cycles. EIS measurements were performed at 0.5 V during charging, in the *n*+1 cycle (*n* = 1, 3, 10, 50). For the symmetric cell impedance in (d), the electrodes were charged and discharged for 1 cycle and charged again to 0.5 V in half cells and disassembled for preparation of the symmetric cells.

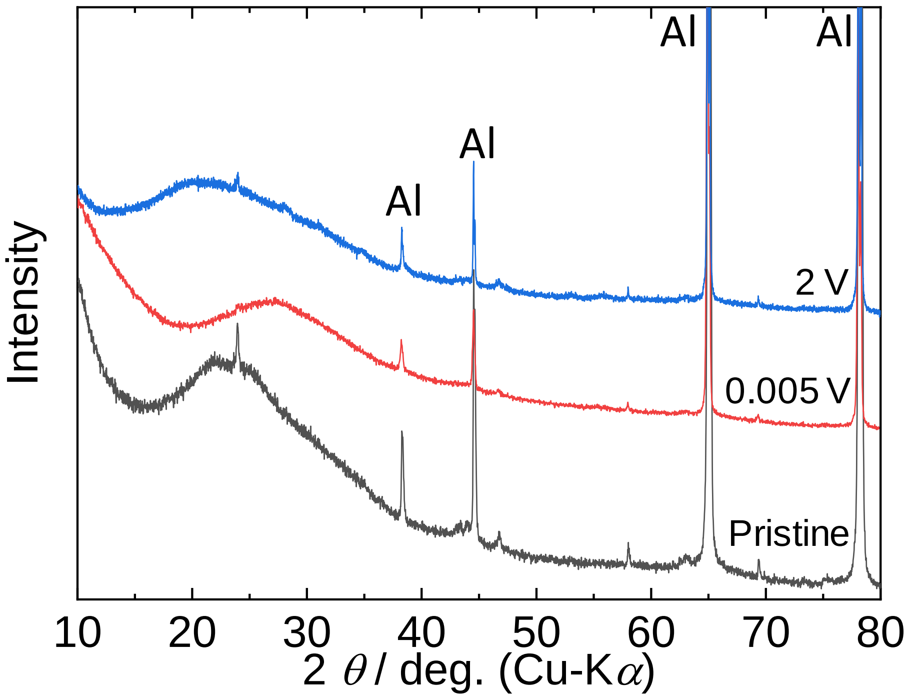

Figure 7-10 *Ex situ* XRD patterns of SiP_2/C (70:30) electrode (pristine, charging: 0.005 V, and discharging: 2.0 V) during the first cycle. Electrolyte: IL. Temperature of charge-discharge: 90 °C. The small peaks at 58.1° and 69.2° are identified as the aluminum $K\beta$ peaks at 65.0° and 78.3°.

References

[1] W. Li, L. Ke, Y. Wei, S. Guo, L. Gan, H. Li, T. Zhai, H. Zhou, J. Mater. Chem. A, 5 (2017) 4413-4420.

[2] Y. Kim, Y. Kim, A. Choi, S. Woo, D. Mok, N.-S. Choi, Y.S. Jung, J.H. Ryu, S.M. Oh, K.T. Lee, Adv. Mater., 26 (2014) 4139-4144.

[3] C.-H. Lim, T.-Y. Huang, P.-S. Shao, J.-H. Chien, Y.-T. Weng, H.-F. Huang, B.J. Hwang, N.-L. Wu, Electrochim. Acta, 211 (2016) 265-272.

[4] D. Duveau, S.S. Israel, J. Fullenwarth, F. Cunin, L. Monconduit, J. Mater. Chem. A, 4 (2016) 3228-3232.

[5] G. Coquil, B. Fraisse, N. Dupré, L. Monconduit, ACS Appl. Energy Mater., 1 (2018) 3778-3789.

[6] J. Saddique, X. Zhang, T. Wu, X. Wang, X. Cheng, H. Su, S. Liu, L. Zhang, G. Li, Y. Zhang, H. Yu, ACS Appl. Energy Mater., 2 (2019) 2223-2229.

[7] C.-Y. Wang, Y.-H. Yi, W.-C. Chang, T.-L. Kao, H.-Y. Tuan, J. Power Sources, 399 (2018) 49-58.

[8] J. Hwang, K. Matsumoto, T. Nohira, R. Hagiwara, Electrochemistry, 85 (2017) 675-679.

[9] C.-H. Wang, C.-H. Yang, J.-K. Chang, Chem. Commun., 52 (2016) 10890-10893.

[10] J. Hwang, K. Matsumoto, R. Hagiwara, J. Phys. Chem. C, 122 (2018) 26857-26864.

[11] J. Hwang, K. Takeuchi, K. Matsumoto, R. Hagiwara, J. Mater. Chem. A, 7 (2019) 27057-27065.

[12] K. Matsumoto, Y. Okamoto, T. Nohira, R. Hagiwara, J. Phys. Chem. C, 119 (2015) 7648-7655.

[13] P.C. Donohue, W.J. Siemons, J.L. Gillson, J. Phys. Chem. Solids, 29 (1968) 807-813.

[14] G.J. Fan, F.Q. Guo, Z.Q. Hu, M.X. Quan, K. Lu, Phys. Rev. B, 55 (1997) 11010-11013.

[15] A.W. Weeber, H. Bakker, Physica B, 153 (1988) 93-135.

[16] C.C. Koch, React. Solids, 8 (1990) 283-297.

[17] R. Reinhold, U. Stoeck, H.-J. Grafe, D. Mikhailova, T. Jaumann, S. Oswald, S. Kaskel, L. Giebeler, ACS Appl. Mater. Interfaces, 10 (2018) 7096-7106.

[18] B.H. Park, S. Haghighat-Shishavan, M. Nazarian-Samani, K.-B. Kim, J. Power Sources, 434 (2019) 226759.

[19] B.E. Gurkan, Z. Qiang, Y.-M. Chen, Y. Zhu, B.D. Vogt, J. Electrochem. Soc., 164 (2017) H5093-H5099.

[20] J. Sun, G. Zheng, H.-W. Lee, N. Liu, H. Wang, H. Yao, W. Yang, Y. Cui, Nano Lett., 14 (2014) 4573-4580.

[21] W.-J. Li, S.-L. Chou, J.-Z. Wang, H.-K. Liu, S.-X. Dou, J. Mater. Chem. A, 4 (2016) 505-511.

[22] H. Usui, Y. Domi, K. Fujiwara, M. Shimizu, T. Yamamoto, T. Nohira, R. Hagiwara, H. Sakaguchi, ACS Energy Lett., 2 (2017) 1139-1143.

[23] M. Dahbi, M. Fukunishi, T. Horiba, N. Yabuuchi, S. Yasuno, S. Komaba, J. Power Sources, 363 (2017) 404-412.

Chapter 8

General conclusions

NIBs have been attracting a huge attention owing to their high electrochemical performance and prospective cost benefits. To realize the practical application of NIBs, high performance and safe operation have to be simultaneously attained. ILs possessing low flammability and volatility enable safe operations, and their high ionic conductivity is attractive for high power applications. However, their cost drawback has to be compensated by other components of the battery. Red phosphorus, which is abundant on the earth and possesses one of the highest theoretical Na-storage capacities, holds promise for cost effective and high energy density applications. The limitations of red phosphorus such as low electrical conductivity and large volume change during charge and discharge have been tackled from various perspectives, and one of the highly investigated approaches is the preparation of binary phosphides. From this point of view, the author has investigated the electrochemical behavior of some binary phosphide materials and their composites (CuP_2/C, V_4P_7/5P, VP_2 and SiP_2/C) using ILs in the present study. The summary of each chapter is given as follows:

In Chapter 3, the electrochemical behavior of CuP_2/C (80:20 in w/w) prepared by two-step HEBM was investigated using the Na[FSA]-[C_3C_1pyrr][FSA] IL (20:80 in molar ratio) at 25 and 90 °C. This composite provided a high reversible capacity of 595 mA h g^{-1} at 100 mA g^{-1} and a high rate capability with a capacity retention of 65 % (366 mAh g^{-1}) at a high current density of 8000 mA g^{-1}. *Ex-situ* XRD results confirmed the formation of Na_3P after charging and amorphization of the product after discharging. However, *in-situ* XRD performed at a slower rate of 50 mA g^{-1} detected the reversible formation of Cu_3P after charging without Na_3P peaks for 2 cycles, indicating the correlation between charging rate and charging product.

In Chapter 4, the carbon content in the CuP$_x$-Cy composite was optimized based on the electrochemical performance using the Na[FSA]-[C_3C_1pyrr][FSA] IL electrolyte at 25 and 90 °C. The CuP$_x$-C30 provided the optimum performance by delivering a high rate capability (358 mA h g^{-1} at 8000 mA g^{-1}) and excellent cycleability (100% after 350 cycles) at 90 °C. The presence of P-O-C bond and robust SEI layer formation in IL were found as the main factor which was supported by EIS and GITT measurement with cycling. In this chapter, the importance of carbon content in the copper phosphide / carbon composite and IL electrolyte was highlighted.

In Chapter 5, the charge-discharge behavior of vanadium phosphide-phosphorus composite (V_4P_7/5P) was investigated at 25 and 90 °C. It was prepared by one-step HEBM at a relatively milder condition (400 rpm) than the phosphides prepared in other chapters. High discharge capacities of 560 mA h g^{-1} with a Coulombic efficiency of 88%, and 738 mA h g^{-1} with 86% were observed at 25 and 90 °C, respectively. A capacity of 360 mA h g^{-1} was obtained even at a high rate of 8000 mA g^{-1} at 90 °C, and 47.2% capacity retention was achieved after 100 cycles. In addition, pure V_4P_7 also provided decent discharge capacities of 270 and 470 mA h g^{-1} at 25 and 90 °C, respectively, as well as long cycle lives. The *ex-situ* XRD analysis revealed the reversible sodiation and desodiation of phosphorus in Na_3P and the insertion mechanism of the V_4P_7 phase. This chapter demonstrated the enhanced performance of vanadium phosphide and vanadium phosphide-phosphorus composite utilizing IL electrolyte.

In Chapter 6, the charge-discharge behavior of vanadium diphosphide (VP_2) was investigated. This compound was prepared by one-step HEBM at an intense condition (850 rpm) and characterized by XRD, SEM, TEM and XPS. Even though VP_2 contains more phosphorus than V_4P_7, the capacity obtained at 25 °C was limited (~50 mA h g^{-1} at 100 mA g^{-1}). However, a significant increase in Na-storage capacity was observed at 90 °C (~250 mA h g^{-1} at 100 mA g^{-1}). At this temperature, this material showed an excellent capacity retention of 102.4% after

500 cycles and a discharge capacity of 131 mA h g^{-1} at 8000 mA g^{-1}. Symmetric cell EIS and SEM after cycling suggested a suppression of charge transfer resistance at 90 °C and formation of robust SEI layer in IL electrolyte. *Ex-situ* XRD, XPS and XAS studies showed no changes after charging and discharging, suggesting an insertion-based mechanism with little change in lattice size.

In Chapter 7, silicon phosphide-carbon composites (SiP_2/C) prepared by two-step HEBM were investigated using the Na[FSA]-[C_3C_1pyrr][FSA] IL electrolyte at 25 and 90 °C. The SiP_2/C (70:30) composite demonstrated better performance than that of SiP_2/C (80:20), with a high capacity of 420 mA h g^{-1} at a rate of 8000 mA g^{-1} and a 65% capacity retention after 300 cycles at 90 °C in IL. A comparative study showed better capacity and cycleability in IL than in 1 mol dm^{-3} Na[FSA] in EC:DEC, which was supported by symmetric EIS test (SiP_2/C|SiP_2/C) conducted in both the electrolytes. The excellent performance was attributed to the synergistic effect of the strong P-O-C bond and low interfacial resistance in the IL electrolyte.

In this study, phosphide-based materials have shown a considerable promise as negative electrode material candidates by providing a high capacity (gravimetric and volumetric), long lifetime and fast charging and discharging results. In addition, the cost benefits arising from the abundant electrode materials is an additional advantage. In future, it is expected that the multifold advantages of ILs as electrolytes will propel its large scale production, which will ultimately lead to its cost merit. Finally, it is also expected that these materials will hold a significant place in the upcoming energy storage system era towards building a sustainable and green world.

List of Publications

Chapter 3

Shubham Kaushik, Jinkwang Hwang, Kazuhiko Matsumoto, Yuta Sato, Rika Hagiwara

ChemElectroChem, **5** (2018) 1340-1344.

“CuP_2/C Composite Negative Electrodes for Sodium Secondary Batteries Operating at Room-to-Intermediate Temperatures Utilizing Ionic Liquid Electrolyte”

Chapter 4

Shubham Kaushik, Kazuhiko Matsumoto, Yuta Sato, Rika Hagiwara

ChemElectroChem, **7** (2020) 2477-2484.

“Optimization of the Carbon Content in Copper Phosphide-carbon Composites for High Performance Sodium Secondary Batteries Using Ionic Liquids”

Chapter 5

Shubham Kaushik, Kazuhiko Matsumoto, Yuta Sato, Rika Hagiwara

Electrochemistry Communications, **102** (2019) 46-51.

“Vanadium Phosphide–phosphorus Composite as a High-capacity Negative Electrode for Sodium Secondary Batteries Using an Ionic Liquid Electrolyte”

Chapter 6

Shubham Kaushik, Kazuhiko Matsumoto, Yuki Orikasa, Misaki Katayama, Yasuhiro Inada, Yuta Sato, Kazuma Gotoh, Hideka Ando, Rika Hagiwara

Journal of Material Chemistry A, to be submitted.

"Vanadium Diphosphide as a Negative Electrode Material for Sodium Secondary Batteries"

Chapter 7

Zhang Xinyue, Shubham Kaushik, Kazuhiko Matsumoto, Rika Hagiwara

Journal of The Electrochemical Society, **167** (2020) 070514.

"High-Performance Sodium Secondary Batteries Using Synergistic Effect of Amorphous SiP_2/C Anode and Ionic Liquid Electrolyte"

Related work not described in this thesis

Kazuhiko Matsumoto, Jinkwang Hwang, Shubham Kaushik, Chih-Yao Chen, Rika Hagiwara

Energy & Environmental Science, **12** (2019) 3247-3287.

"Advances in Sodium Secondary Batteries Utilizing Ionic Liquid Electrolytes"

Acknowledgements

It is an immense pleasure to express my deep sense of gratitude to Professor Rika Hagiwara, who provided me an opportunity to complete my graduate education under his esteemed supervision. His profound knowledge and expert advises have driven my research journey smoothly due to which I was able to achieve a number of interesting results. I am sincerely grateful to Associate Professor Kazuhiko Matsumoto for his enlightening instructions, constant encouragement, and fruitful discussions. Moreover, I am highly motivated by his great writing skills and corrections without which this thesis and the papers would not attain its present heights. I am grateful to Associate Professor Kouji Yasuda for his educational instructions and helpful advice. I am truly thankful to Professor Toshiyuki Nohira and Professor Takashi Sagawa for carefully reviewing the thesis and providing valuable comments and suggestions.

I express my thanks to the present and former members of Energy Chemistry Lab for their constant all-round supports. I express my indebtedness to Dr. Jinkwang Hwang, who has been a mentor and friend both. His valuable comments and insights have shaped my work in a coherent way. I feel obliged to other group members Mr. Hiroki Yamamoto, Mr. Di Wang, Ms. Yayun Zheng, and Ms. Huan Yang. Special thanks are also given to Ms. Naoko Sakamoto for her various help and heedful care. I would like to give a special mention to my partner and co-author, Ms. Xinyue Zhang for her unflinching love and emotional support.

It is my privilege to thank my mother Dr. Sunita Kaushik, my father Dr. Deepak Kaushik, my brother Puneet Kaushik and my sister-in-law Dolly Kaushik. Their unbounded affection and moral support are the real strength behind my accomplishments.

Finally, I feel extremely beholden to God, who blessed me with an opportunity to explore something that I hope will benefit the society.

Not all acknowledgments are described here. I am thankful to all those who are related to this study.

Shubham Kaushik

July 2020